Neutron Interferometry

Fabrication and Testing of Diffraction Gratings for Phase Contrast Imaging with Neutrons

Diploma Thesis

of

Christian Grünzweig

April 2006

Carried out at the Paul Scherrer Institut in Switzerland

Submitted at the Eberhard Karls University Tübingen
Faculty for Mathematics and Physics

Supervisors at the Eberhard Karls University Tübingen:

1. Prof. Dr. Jörg Ihringer (Institut of Applied Physics)

2. Prof. Dr. Frank Schreiber (Institut of Applied Physics)

Supervisors at the Paul Scherrer Institut:

Dr. Christian David (Laboratory for Micro- and Nanotechnology)

Dr. Franz Pfeiffer (Swiss Light Source)

Abstract

In this diploma thesis a new interferometric neutron imaging technique based on diffraction gratings is presented. This technique was worldwide for the first time tested and is more efficient than existing methods. This new technique is the neutron analogue of a recently developed technique for X-rays at the Paul Scherrer Institut (PSI).

Today, the neutron radiography applications are based on the attenuation of the radiation inside the objects. However, imaging the phase shift of neutron waves passing through an object provides new and complimentary information to the standard attenuation image.

With this interferometric technique one can measure simultaneously the phase image and the attenuation image of objects. The two images provide independent information, since the phase image exploits the real part of the refractive index whereas the attenuation image exploits the imaginary part of the refractive index. This new grating based interferometer technique is capable of detecting the wave front distortion of the incident wave caused by the object.

The aim of the diploma thesis was to determine whether it is possible to obtain phase contrast images with neutrons as already shown with the grating interferometer for X-ray. One part of the work of this diploma thesis therefore was the development of a fabrication process for suitable diffraction gratings for neutrons for this interferometer. The other part of the diploma thesis was the testing of these gratings. The grating interferometer consists of three diffraction gratings, two absorption gratings and one phase grating. The fabrication process was developed for fabricating the gratings with optical lithography. The grating size is 64 mm $\times$ 64 mm. The fabrication was challenging since the gratings have to fulfill different demands to the grating materials and the grating periods. The two absorption gratings are made of Gadolinium with a period of 1100 μm and 4 μm. The phase grating is made of Silicon and has a period of 8 μm. The development of the fabrication process was realized at the clean room facility of the Laboratory for Micro- and Nanotechnology (LMN) at PSI. The testing of the gratings and therewith the implementation of the setup at a neutron source was realized at the ICON (Imaging with Cold Neutrons) beam line, at the spallation neutron source (SINQ) at PSI.

With our new technique of a grating based neutron interferometer we should be able to overcome the efficiency problems that challenge other techniques, since our new technique requires less temporal and spatial coherence from the source. The experimental results showed that our method is significantly (about two orders of magnitude) more efficient than the other existing methods. For example, in our measurement in which we measured rods of Ti, Pb, Mo and Mg, the total exposure time for an area of

64 mm $\times$ 64 mm is on the order of 100 seconds. In addition we are able to measure quantitatively the phase shift of neutron waves introduced by the objects. As well, our measured results are in good agreement with the simulated results.

ZUSAMMENFASSUNG

In der vorliegenden Diplomarbeit wird eine neue bildgebende Methode der Neutroneninterferometrie, basierend auf Beugungsgittern, vorgestellt. Diese Technik wurde weltweit zum ersten Mal getestet und ist weit effizienter als die existierenden Methoden. Die neue Technik ist das mit Neutronen durchgeführte Analogon zu einer vor kurzer Zeit entwickelten Methode für Röntgenstrahlen am Paul Scherrer Institut (PSI).

Die Anwendungen der Neutronenradiographie beruhen meistens auf der Abschwächung der Strahlung im Inneren von Objekten. Über diese Information hinaus liefert die Darstellung der Phasenschiebung von Neutronenwellen beim Durchdringen eines Objektes zusätzlich neue und komplementäre Information.

Mit dieser neuen Technik kann gleichzeitig das Phasenbild und das Abschwächungsbild von Objekten gemessen werden. Die beiden Bilder liefern unabhängige Informationen, da das Phasenbild den Realteil des Brechungsindexes, das Abschwächungsbild hingegen den imaginären Teil des Brechungsindexes ausnützt. Diese neue auf Beugungsgitter basierende Interferometriemethode kann Verformungen der einfallenden Wellenfront, hervorgerufen durch das Objekt, sichtbar machen.

Das Ziel der Diplomarbeit war es herauszufinden, ob man mit einem analogen Aufbau zu dem des Röntgen-Gitterinterferometers auch mit Neutronen Phasenkontrastbilder erhalten kann. Die Diplomarbeit besteht deshalb aus zwei Teilen, der Entwicklung eines Herstellungsprozesses für die Beugungsgitter für das Neutroneninterferometer und den Messungen zur Charakterisierung der Gitter und der mit ihnen erzielbaren Phasenkontrastbilder. Das Gitterinterferometer besteht aus drei Beugungsgittern, zwei Absorptionsgittern und einem Phasengitter. Es wurde ein Prozess entwickelt, um die Gitter mittels optischer Lithographie herzustellen. Die Gittergrösse ist 64 mm $\times$ 64 mm. Die Gitterherstellung war eine Herausforderung, da die Gitter unterschiedliche Anforderungen in Bezug auf Material und Gitterperioden erfüllen müssen. Die beiden Absorptionsgitter wurden aus Gadolinium mit einer Periode von 1100 μm und 4 μm hergestellt. Das Phasengitter mit einer Periode von 8 μm ist aus Silizium hergestellt. Die Herstellung erfolgte in den Reinräumen des Labors für Mikro -und Nanotechnologie (LMN) am PSI realisiert. Das Testen der Gitter und das damit verbundene Implementieren des Aufbaus wurde an der ICON Strahlline an der Spallationsneutronenquelle (SINQ) am PSI verwirklicht.

Mit der neuen auf Gitter basierenden Interferometrietechnik sollte man in der Lage sein, die bei anderen Techniken auftretenden Effizienzprobleme, zu bewältigen, da unsere Methode nur geringe räumliche und geringe zeitliche Kohärenz von der Quelle benötig.

Die experimentellen Ergebnisse zeigten dass unsere Methode bedeutend (mehr als

zwei Grössenordnungen) effizienter ist als die bestehenden Methoden. In unserer Messung an Ti, Pb, Mo und Mg Stangen, lag die gesamte Belichtungszeit für eine Bildfläche von 64 mm $\times$ 64 mm in der Grössenordung von 100 Sekunden. Zusätzlich können wir die Phasenschiebung von Neutronenwellen, hervorgerufen durch das Objekt, quantitativ messen. Ebenso stimmen unsere Messergebnisse gut mit den Simulationsergebnissen überein.

Contents

1 Introduction **1**

2 Theory **3**
2.1 Neutron sources and their properties . . . 3
2.1.1 Neutron facilities . . . 3
2.1.2 Classifying the neutron energy . . . 4
2.2 Interaction between neutrons and matter . . . 5
2.2.1 Attenuation of a neutron beam . . . 5
2.2.2 Shell model of nucleus and absorption cross section . . . 7
2.3 Physical basics of neutron optics . . . 9
2.3.1 Neutron optics and its analogy to light optics . . . 9
2.3.2 Refractive index for neutrons . . . 10
2.4 Phase shift of neutron waves passing through matter . . . 12
2.5 Neutron scattering length and scattering cross section . . . 13

3 Principles of grating interferometry **17**
3.1 Setup of the grating interferometer . . . 17
3.2 Formation of differential phase contrast images . . . 17
3.2.1 Function of the phase grating G_1 - fractional Talbot effect . . . 19
3.2.2 Function of the analyzer grating, G_2 . . . 20
3.2.3 Function of the source grating, G_0 . . . 21
3.3 Phase retrieval by interferometric phase-stepping . . . 22
3.4 Coherence requirements . . . 23
3.5 Simulations of phase contrast radiography images . . . 25

4 Design of the grating interferometer **28**
4.1 Grating periods and inter grating distances . . . 28
4.2 Wavelength selection . . . 31
4.3 Structure heights of the gratings . . . 33

5 Grating fabrication **37**
5.1 Source grating G_0 . . . 37
5.1.1 Sputtering process . . . 38
5.1.2 Photo lithography process . . . 39
5.1.3 Etching process . . . 41

5.2 Phase grating G_1 . . . 44
5.2.1 Photo lithography process . . . 44
5.2.2 Etching process . . . 45
5.3 Analyzer grating G_2 . . . 48
5.3.1 Evaporation process . . . 48

6 Experimental setup and results **53**
6.1 Experimental setup at the ICON beam line . . . 53
6.1.1 Source grating mount . . . 55
6.1.2 Interferometer box . . . 56
6.2 Experimental results . . . 59
6.2.1 Optimization of the visibility . . . 59
6.2.2 Phase contrast radiography images . . . 63

7 Conclusion and Outlook **65**

A Run sheets for G_0, G_1, G_2 **67**

Bibliography **73**

Acknowledgment **77**

Chapter 1

Introduction

In quantum mechanics light is considered to be both wave-like and particle-like. The Young's double slit experiment in the 19th century indicated the wave property of light. Albert Einstein in 1905, explained that light consists of particles (photons), and the energy of such a particle is proportional to the frequency of the light. De Broglie in 1923 extended this dualism of light to all moving massive particles. In quantum mechanics neutrons are described by de Broglie wave packages. The Germer and Davison experiment in 1927 first showed the interference effects of electrons as massive particles. Due to this fact it should be possible to observe interference effects with neutrons similar to those observed with light.

The first interferometry experiment with neutrons as the massive particles was done in 1974 by Rauch et al. [Rau1974]. Neutron interferometry has been employed for demonstrating many fundamental features of quantum mechanics like the quantum superposition law. For the first neutron interferometry experiment they were using a perfect crystal Si interferometer as invented for hard X-rays in 1964 by Bonse and Hart. Over the past years, many neutron interferometry experiments have been performed with these devices to detect and image phase shifts of neutron waves passing through objects [Rau2000]. In the past years two new techniques have been developed to detect the neutron wave phase variations. On the one hand this is a technique using an analyzer crystal [Tre2003], and on the other hand the technique based on the free-space propagation method [All2000] [McM2003]. However, some practical difficulties arise for the efficiency of these techniques. The techniques using the crystal interferometer or analyzer crystals require temporal coherence and therefore monochromatic radiation. Hence, these techniques are very inefficient since only a small fraction of the neutron spectrum is used. The free-space propagation technique is limited in efficiency since this technique requires high spatial coherence which can only be achieved with very small apertures defining the incident neutron beam.

A new technique, which we will present in this thesis, utilizes a grating based neutron interferometer. It is similar to the grating based interferometer for X-rays which was developed at the PSI over the last years [Dav2002, Wei2005]. With the X-ray grating based interferometer it was actually possible to obtain phase contrast images with incoherent radiation from a conventional X-ray tube [Pfe2006a].

The diploma thesis is organized in the following manner. Chapter 2 delivers the the-

oretical background of neutron optics and a theoretical explanation of the experimental results. Chapter 3 explains the principles of grating based neutron interferometry and shows simulated phase radiography images. Detailed information about the particular design of the interferometer, gratings and setup parameters, is provided in Chapter 4. In chapter 5, the grating fabrication process is shown, which was developed and performed at the Laboratory for Micro- and Nanotechnology (LMN) at the Paul Scherrer Institute (PSI). The assembly of the setup at the ICON (Imaging with Cold Neutrons) beam line at the spallation neutron source (SINQ) at PSI, as well as the results are described in chapter 6. The conclusion and future outlook are given in chapter 7.

Chapter 2

Theory

The theory part in this chapter is geared mainly towards the understanding of our experimental results. The first section 2.1 describes how high flux neutron beams are produced, and how neutron energies are classified. Interaction between neutrons and matter are described in section 2.2, section 2.4 and section 2.5. In section 2.3 the extremely close mathematical analogies between wave-light properties of matter and light optics are introduced. One similarity is the refractive index. The second section describes the two reasons for attenuation of a neutron beam, when passing through matter: absorption and scattering. Absorption of neutrons is discussed in context with the nuclear shell model. Section 2.4 deals with the phase shift of neutron waves when they are passing through matter. The derivation of the scattering length and the total scattering cross section is given in subsection 2.5 .

2.1 Neutron sources and their properties

The neutron was discovered in 1932 by the English physicist James Chadwick. The neutron is one of the constituent particles of every atomic nucleus except ordinary hydrogen. A neutron has no electrical charge but a magnetic moment. Its mass is nearly 2000 times that of an electron. A free neutron, one that is not incorporated into a nucleus is unstable decaying with a half-life time of about 12 minutes into a proton, an electron, and an antineutrino. The next two subsections cover how high flux neutron beams are created, and the classification of beam energies.

2.1.1 Neutron facilities

Beams of neutrons are produced from nuclear reactions. There are two types of facilities generating high flux neutron beams. The first type are research reactors. The fundamental process of a research reactor is the nuclear fission of highly enriched Uranium. $^{235}_{98}$U picks up a slow neutron and decays into three neutrons and two lighter nuclei.

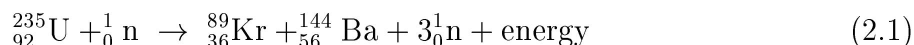

$$^{235}_{92}\mathrm{U} +^{1}_{0}\mathrm{n} \;\rightarrow\; ^{89}_{36}\mathrm{Kr} +^{144}_{56}\mathrm{Ba} + 3^{1}_{0}\mathrm{n} + \mathrm{energy} \qquad (2.1)$$

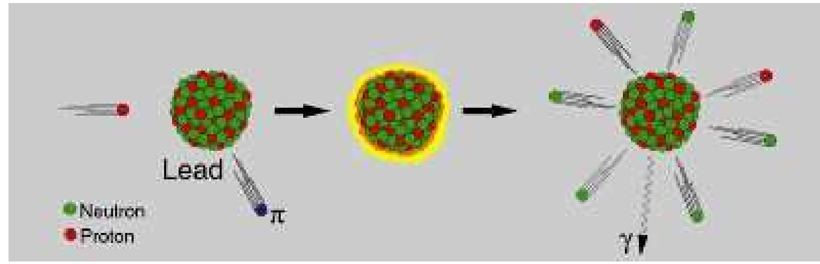

Figure 2.1: *Spallation process [SINQ]*

The crucial effect of the fission of $^{235}_{92}$U is a chain reaction, because one neutron initiates the emission of 3 neutrons, moderating them to accordingly slow speed, increases the probability for next generations reactions. The number of the neutrons increases exponentially with the number of decay generations. The maximum unperturbed thermal flux at the research reactor at the Institute Laue-Langevin (ILL) in France is $1.5 \times 10^{15} \frac{n}{cm^2 \cdot s}$. The research reactor FRM-II in Munich provides a maximum undisturbed thermal neutron flux density of $8 \cdot 10^{14} \frac{n}{cm^2 \cdot s}$.

The second type of facilities for generating high flux neutron beams is spallation sources. At the spallation source SINQ at PSI high-energy protons bombard a heavy atomic nucleus. The present target is an array of lead rods, enclosed in stainless steel tubes. The lead cores are strongly stimulated by the protons (nuclear heated). This internal energy is mainly released by evaporating neutrons. For every proton striking the nucleus, 20 to 30 neutrons are expelled (Fig 2.1). In contrast to nuclear fission chain reaction does not occur at spallation sources. The spallation neutron source SINQ is a continuous source - the first of its kind in the world - with a flux of about $1 \times 10^{14} \frac{n}{cm^2 \times s}$. Besides thermal neutrons, a liquid deuterium moderator slows neutrons down and shifts their spectrum to lower energies.

2.1.2 Classifying the neutron energy

The development of quantum mechanics started with the equivalence hypothesis of particle motion and wave behavior, shown in the de Broglie relation

$$mv = h/\lambda = \hbar k \, . \tag{2.2}$$

Where the momentum p of a particle of mass m and group velocity v is related to a matter wave with the wavelength λ. The wavelength can also be expressed in terms of the neutron energy E:

$$E = \frac{mv^2}{2} = \frac{h^2}{2m\lambda^2} \Rightarrow \lambda = \frac{h}{\sqrt{2mE}} \tag{2.3}$$

Neutrons cannot be deaccelerated like charged particles, but one can start with relatively high-energy neutrons and moderate them through collisions with atoms. This process can result in neutrons with very low energies. The classification of neutron energies is given in Table 2.1.

neutron	energy	wavelength
cold	0.5meV-2meV	12.8Å-6.4Å
thermal	2meV-100meV	6.4Å-0.9Å
epithermal	100meV-1eV	0.9Å-0.28Å
intermedite range	1eV-0.8MeV	0.28Å-0.01Å
fast	>0.8MeV	<0.01Å

Table 2.1: *Neutron classification and corresponding energy and wavelength [Neutra]*

2.2 Interaction between neutrons and matter

Neutrons interact through all four forces of nature: the electromagnetic, strong, weak, and gravitational interaction. Nuclear forces, the weak interaction but mainly the strong interaction, play the leading role when neutrons pass through matter. As a beam of neutrons passes through matter, the intensity will decrease as neutrons are removed from the beam by nuclear reactions. For fast neutrons many reactions are possible such as (n,p), (n,α) and (n,2n), but for cold neutrons the primary reaction is neutron capture (n,γ). In subsection 2.2.1 only the main two processes that lead to attenuation are considered, namely scattering and absorption. In subsection 2.2.2 the relation between the nuclear shell model and the capture cross section is discussed.

2.2.1 Attenuation of a neutron beam

As an uncharged particle, the neutron does not interact with the electrostatic potential of protons and electrons. The interaction with matter is dominated by the strong neutron-nuclear interaction. Unlike X-rays, where the attenuation coefficient rises linearly with the number of electrons per atom, the attenuation coefficient for neutrons does not linearly increase with the number of neutrons per atom. A plot of the attenuation coefficient versus the atomic number is shown in Fig. 2.2. In simplified terms, neutrons are attenuated in matter either by the scattering or absorption from the nucleus of a target atom. The cross sections for scattering (σ_{s}) and absorption (σ_{a}) sum to the total cross section (σ_{t})

$$\sigma_{\mathrm{t}} = \sigma_{\mathrm{s}} + \sigma_{\mathrm{a}} \tag{2.4}$$

The scattering cross section (σ_{s}) is composed of a coherent part ($\sigma_{\mathrm{s,coh}}$) and an incoherent part ($\sigma_{\mathrm{s,incoh}}$). The scattering cross section is described in more detail in subsection 2.5.2 . In contrast to the scattering cross section, the absorption cross section depends on the neutron energy and therefore its velocity. The formula of the total cross section for neutrons with a velocity v_n is

$$\sigma_{\mathrm{t}} = \sigma_{\mathrm{s}} + \frac{2200\frac{m}{s}}{v_{\mathrm{n}}}\sigma_{\mathrm{a,2200}} \tag{2.5}$$

The absorption cross section is described more detailed in subsection 2.2.2 . Table 2.2 shows the incoherent scattering cross sections and the absorption cross sections of

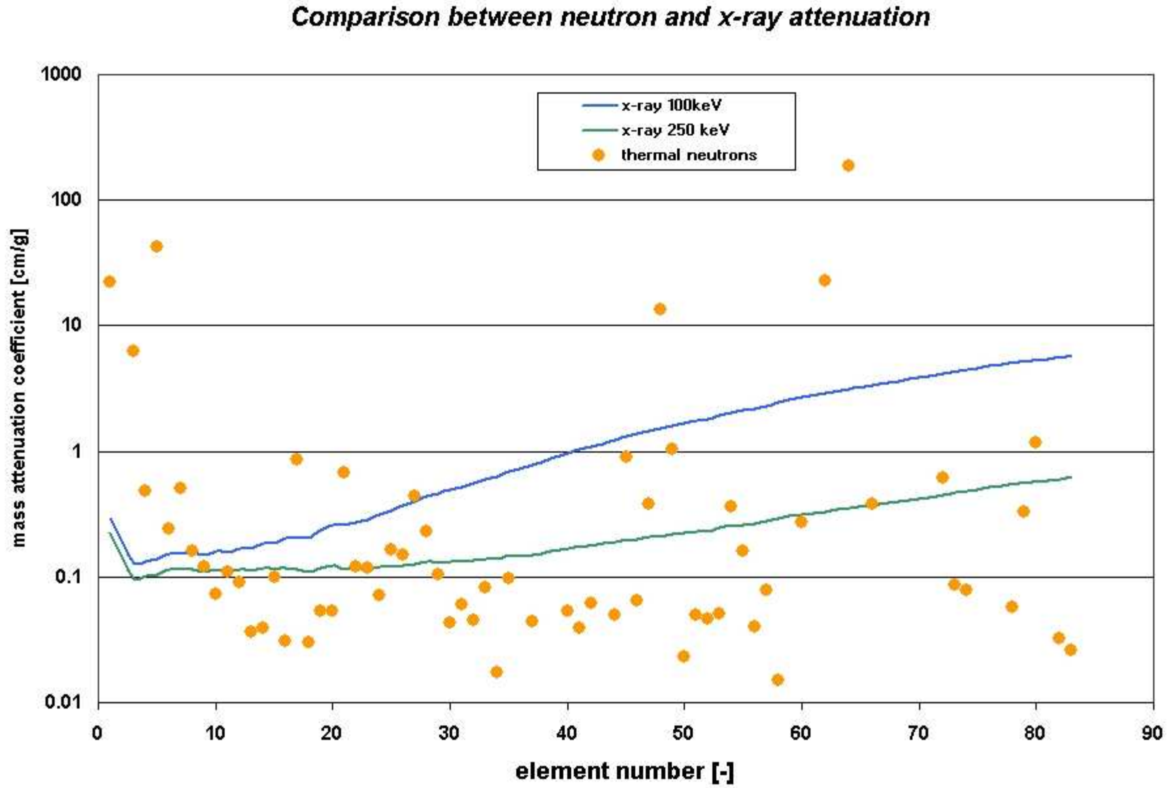

Figure 2.2: *Attenuation coefficient for thermal neutrons in comparison to X-rays [Neutra].*

several elements. The coherent part of the scattering cross section can be ignored in attenuation based neutron radiography applications. However, the coherent part of the scattering cross section is the exploited one for our phase sensitive measuring method.

The intensity of the incoming neutron beam is reduced through the loss of neutrons. Making the assumption that none of the scattered neutrons will hit the detector the attenuation of the beam intensity I is given by

$$\frac{I}{I_0} = e^{-\mu x}. \tag{2.6}$$

Where the attenuation coefficient μ is given by

$$\mu = \sigma_t \frac{\rho N_A}{M_{Mol}}. \tag{2.7}$$

Where ρ is the density of the attenuating element, N_A is the Avogadro number and M_{Mol} is the molar mass of the element.
For an arbitrary number of elements along a straight line S the formula becomes

$$\frac{I}{I_0} = exp\left[(-\int_S \mu(x,y)ds)\right] \tag{2.8}$$

Element	$\sigma_{\text{s,incoh}}[barn]$	$\sigma_{\text{a}}[barn]$
H	80.26	0.33
B	1.7	767
^{10}B	3	3835
^{11}B	5.77	0.0055
Mg	0.08	0.063
Al	0.0082	0.231
Si	0.004	0.171
Ti	2.87	6.09
Pb	0.003	0.171
Gd	151	49700
^{155}Gd	25	61100
^{156}Gd	0	1.5
^{157}Gd	394	259000

Table 2.2: *Incoherent and absorption cross sections of some elements [NCNR92].*

Where the attenuation coefficient is

$$\mu(x,y) = \sum_i \mu_i(x,y) = \sum_i \sigma_{t_i} \frac{\rho_i(x,y) N_A}{M_{Mol_i}} \tag{2.9}$$

The simple exponential attenuation law does not hold for all situations. Thick samples or strongly scattering (e.g. hydrogen) or absorbing materials (e.g. containing strong absorbers like boron, gadolinium) show a deviation, due to multiple scattering effects or the need to take the changing neutron energy spectrum into account. Since the absorption cross section depends on v_n^{-1} (Eqn. 2.5), the slower neutrons have a faster attenuation.

2.2.2 Shell model of nucleus and absorption cross section

The reason for the, at the first sight, random structure of the attenuation coefficients for neutrons (Fig 2.2) and the differences in the absorption cross sections for different elements and isotopes (Tab. 2.2) is explained by the nuclear shell model [Kra1988]. Atomic theory is based on the atomic shell model which provides remarkable insights in the atomic structure. Nuclear physicists use a similar theory to attack the problem of nuclear structure. In the atomic shell model shells are filled with electrons. In the nuclear shell model the same is done for the nucleons within the nucleus respecting the Pauli exclusion principle. In the atomic case, the potential is supplied by the Coulomb field of the nucleus. Nucleons move in a potential that they create as an ensemble. The first step in developing the nuclear shell model is the choice of the potential. A realistic form of the nuclear potential is an intermediate form between a three-dimensional simple harmonic oscillator potential which extends to infinity and a potential well which has a sharp cut-off at a finite radius. The intermediate potential

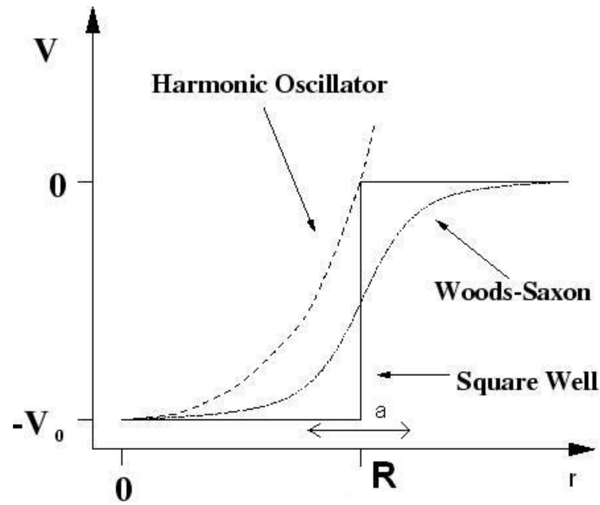

Figure 2.3: *The Wood-Saxon potential is an intermediate form between a three-dimensional simple harmonic oscillator potential and a potential well. The parameter R is the mean radius and the parameter a is the skin thickness of the potential. The skin thickness is the distance over which the potential changes from 0.1 V_0 to 0.9 V_0*

form, the Wood-Saxon potential in Fig 2.3 is commonly used

$$V(r) = \frac{-V_0}{1 + exp\left(\frac{r-R}{a}\right)}. \tag{2.10}$$

A nucleon moving in a Wood-Saxon potential, leads to an energy quantization. In addition we have to consider the spin-orbital interaction of a nucleon which plays an important role in the nuclear potential. Such a coupling also exists in the atomic shell model between the spin and the orbital angular momentum. Its nature is purely electromagnetic and leads to a relatively small splitting of the energy levels. In contrast to the atomic shell model, spin-orbital coupling inside of the nucleus, is comparable to the distance term (Eqn. 2.10). The nuclear potential (Eqn. 2.10) must be modified to include the spin-orbital interaction to

$$V_{nuc} = V(r) + V_{ls}(r)(\vec{l} \cdot \vec{s}). \tag{2.11}$$

The nucleon energy levels are the energy Eigenstates of the spin-orbit modified potential. Filling these energy levels with either protons or neutrons, there are certain points where the adjacent state have significantly different binding energy.

Closed shell configurations lead to magic numbers, like filled outer electron shells for a noble gas. This observation, that there are certain *magic numbers* 2, 8, 20, 28, 50, 82, 126 which correspond to more tightly bond nuclei is explained by the nuclear shell model (Fig. 2.4).

With the knowledge and the origin of the magic numbers it is clear why $^{208}_{82}$Pb has a relatively small absorption cross section (Tab. 2.2). The $^{208}_{82}$Pb isotope has 126 neutrons and 82 protons. This is a double magic nucleus, because both the number of protons and neutrons are magic numbers. Since magic numbers represent filled shells,

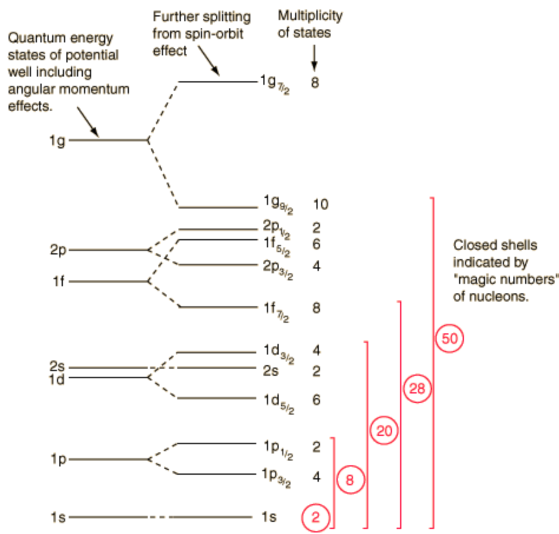

Figure 2.4: *Nuclear shell model. The shell effect is quite apparent, and the magic numbers 2, 8, 20, 28, 50 are apparent in nature [Hyp2005].*

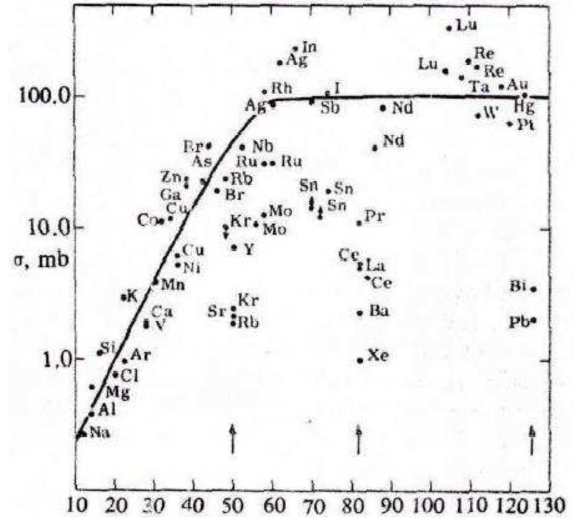

Figure 2.5: *Neutron absorption cross section as a function of the number of neutrons. Note the decrease of the absorption cross section by roughly two orders of magnitude near the magic numbers N=50,82 and 126 [Kra1988]*

the probability for a neutron capture is negligibly small. In general nuclei with a magic number of neutrons have a much lower absorption cross section than their isotopes and neighbor elements (Fig. 2.5).

2.3 Physical basics of neutron optics

In the next section we will point out, that the word "optics" can be applied to the propagation of neutrons through various fields [Rau2000]. The extremely close mathematical analogies between the propagation of light described by the Maxwell's equations and the propagation of low-energy neutrons as described by the Schrödinger equation, shown in subsection 2.3.1 , suggests that most phenomena in light optics have analogies in neutron optics. The experiments of neutron optics are particularly analogous to those performed with x-rays, because of the similar wavelengths. In subsection 2.3.2 a connection between neutrons and light is made via the derivation of the refractive index .

2.3.1 Neutron optics and its analogy to light optics

Matter wave fields $\psi(\mathbf{r},t)$ are described by the Schrödinger equation

$$H\psi(\mathbf{r},t) = \left(-\frac{\hbar^2}{2m}\nabla^2 + V(\mathbf{r},t)\right)\psi(\mathbf{r},t) = i\hbar\frac{\partial\psi(\mathbf{r},t)}{\partial t} \tag{2.12}$$

and electromagnetic wave fields are given by the vacuum wave equation of classical optics

$$\nabla^2\psi(\mathbf{r},t) - \frac{1}{c^2}\frac{\partial^2\psi(\mathbf{r},t)}{\partial t^2} = 0 \tag{2.13}$$

Both equations are separable in space and time and can therefore be solved in free space using the plane wave approach

$$\psi_k(\mathbf{r},t) = a_k e^{i(\mathbf{k}\cdot\mathbf{r}-\omega_k\cdot t)} = \psi(\mathbf{r})e^{i\omega t}. \tag{2.14}$$

This simplifies in both cases to the Helmholtz equation,

$$\nabla^2\psi(\mathbf{r}) + k^2\psi(\mathbf{r}) = 0. \tag{2.15}$$

with the following dispersions relations

$$k^2 = \frac{2mE}{\hbar^2} \qquad \text{matter waves,} \tag{2.16}$$

and

$$k^2 = \frac{E^2}{\hbar^2 c^2} \qquad \text{e.m. waves} \tag{2.17}$$

where $E = \hbar\omega$. The velocity of wave propagation for electromagnetic waves is always equal to the velocity of light, whereas for matter waves it is determined by the de Broglie relation (Eqn. 2.2).

The Helmholtz equation describes stationary situations for both kinds of waves (electromagnetic and matter), thus the phenomena are analogous, aside from their different dispersion relations and the differencing interactions. For the time-dependent phenomena differences are expected because the power of the time derivative in the wave equations is different, i.e. of first in order in Eqn. 2.12 and second order in Eqn. 2.13. Since reflection, refraction, diffraction and interference are consequences of the stationary equations, the complete array of wave optical phenomena known from the wave nature of light occur for neutron waves in matter. The phenomena of refraction for neutrons is described in the next section.

2.3.2 Refractive index for neutrons

The derivation of the refractive index for neutrons is quantum mechanical in nature. Neutrons which move inside a medium experience a spatially dependent potential $V(\mathbf{r})$. The energy eigenstate ($E = \hbar\omega$) and the wave function

$$\psi(\mathbf{r},t) = \psi(\mathbf{r})e^{-i\omega t} \tag{2.18}$$

satisfies the time-independent Schrödinger equation

$$\nabla^2\psi(\mathbf{r}) + \frac{2m}{\hbar^2}E\psi(\mathbf{r}) = 0 \tag{2.19}$$

outside the medium, and

$$\nabla^2\psi(\mathbf{r}) + \frac{2m}{\hbar^2}[E - V(\mathbf{r})]\psi(\mathbf{r}) = 0 \tag{2.20}$$

within the medium. Both equations are Helmholtz scalar wave equations as shown in Eqn. 2.15 and can therefore be written as

$$\nabla^2\psi(\mathbf{r}) + k^2\psi(\mathbf{r}) = 0\,. \tag{2.21}$$

With the wave vector $\mathbf{k}$ outside the medium

$$k^2 = \frac{2mE}{\hbar^2} \tag{2.22}$$

and the wave vector $\mathbf{K}$ inside the medium (region of the potential)

$$K^2(\mathbf{r}) = \frac{2m}{\hbar^2}[E - V(\mathbf{r})]. \tag{2.23}$$

It is natural to define the spatially dependent refractive index as the raio of this spatial dependent wavevektor $\mathbf{K(r)}$ to the free space wavevector $\mathbf{k}$ [Sea1989], such that

$$n(\mathbf{r}) := \frac{|\mathbf{K(r)}|}{|\mathbf{k}|} = \sqrt{1 - \frac{V(\mathbf{r})}{E}}\,. \tag{2.24}$$

Since the range of the neutron-nucleus interaction is much smaller than the wavelength a of thermal neutrons the scattering is isotropic. This allows to use the Fermi pseudo potential $V(\mathbf{r})$ to describe the interaction of a neutron with a sample containing many nuclei [Fer1936]

$$V(\mathbf{r}) = \frac{2\pi\hbar^2}{m}\sum_j b_j\delta(\mathbf{r} - R_j) \tag{2.25}$$

where R_j is the position of the jth nucleus and b is the neutron scattering length. The mean interaction potential, or *optical potential*, for a material is defined as

$$\langle V(\mathbf{r})\rangle = \bar{V} = \frac{2\pi\hbar^2}{m}b_cN\,. \tag{2.26}$$

Where N is the mean number of scattering nuclei per unit volume and $b_c = \langle b\rangle$ is the mean coherent scattering length. The scattering length b is in the range of -5 to + 10 fm[1], and in most cases positive. Any absorption or nuclear reaction effects are described by the imaginary term of the scattering potential in Eqn. 2.26, that is, the scattering length b_c becomes complex: $b_c = b' - ib''$ [Bla1952]. This yields according Eqn. 2.24 to an complex index of refraction [Gol1974]

$$n = \sqrt{1 - \frac{\bar{V}}{E}} = 1 - \frac{\lambda^2 N}{2\pi}\sqrt{b_c^2 - \left(\frac{\sigma_r}{2\lambda}\right)^2} + i\frac{\sigma_r N\lambda}{4\pi} = n_r + in_i\,. \tag{2.27}$$

[1]The reason for positive and negative value is explained in section 2.5

The complex refraction index counts for absorption (σ_{a}) and incoherent scattering ($\sigma_{\mathrm{s,incoh}}$) processes. $(\sigma_{\mathrm{r}}) = (\sigma_{\mathrm{a}}) + (\sigma_{\mathrm{s,incoh}})$ is the total reaction cross section per atom. For this reason (σ_{t}) in Eqn. 2.4 has been replaced by (σ_{r}) so that it fulfills the law of beam attenuation. The imaginary part is typically small, and therefore the index of refraction can be approximated as

$$n = 1 - \frac{\lambda^2 N b_c}{2\pi}. \tag{2.28}$$

In summary, the complex refractive index for neutrons with a wavelength λ propagating through a medium is described as

$$n(\mathbf{r}, \lambda) = 1 - \delta(\mathbf{r}, \lambda) + i\beta(\mathbf{r}, \lambda). \tag{2.29}$$

Where the real part δ corresponds to the phase of the propagating wave and β represents the absorption in the medium. One can say that phase contrast imaging exploits the real part of the refractive index (1-δ) while neutron radiography exploits the imaginary part β. In comparison to the refractive index for X-rays, which is generally slightly less than unity, the refractive index for neutrons can either be greater than or less than unity. Thus the coherent scattering length for neutrons can be positive or negative.

2.4 Phase shift of neutron waves passing through matter

As a neutron passes through matter, it experiences an assembly of interactions with nuclei. This leads to an effective optical potential, see Eqn. 2.26. The phase along a neutron path is given by the Feynmann-Dirac path integral of classical mechanics [Fey1948]. The line integral over the Lagrangian L in space-time is given by

$$\phi(\mathbf{r},\mathbf{t}) = \frac{1}{\hbar}\int L dt. \tag{2.30}$$

The Lagrangian is related to the Hamiltonian H by a Legendre transformation

$$L = \mathbf{p} \cdot \mathbf{v} - H \tag{2.31}$$

where $\mathbf{p} = \mathbf{p}_{kinetic} + \mathbf{p}_{hidden}$ is the canonical momentum of the neutron, and $\mathbf{v} = d\mathbf{s}/dt$ is the classical group velocity. The accumulated phase at position $\mathbf{r}$ as function of time t is

$$\phi(\mathbf{r},\mathbf{t}) = \frac{1}{\hbar}\int_{r_0}^{r} \mathbf{p} \cdot d\mathbf{s} - \frac{1}{\hbar}\int_{t_0}^{t} H dt \tag{2.32}$$

In our case

$$H = \left[-\frac{\hbar^2}{2m}\nabla^2 + V(r)\right], \tag{2.33}$$

where the potential $V = V(\mathbf{r})$ depends only on position (Eqn. 2.26). The potential is independent of time and velocity, and thus the force is said to be conservative. Therefore the accumulated phase simplifies to

$$\phi(\mathbf{r}) = \frac{1}{\hbar}\int_{r_0}^{r} \mathbf{p}_{kin} \cdot d\mathbf{s}\,, \tag{2.34}$$

since the Hamiltonian is time-independent. The hidden part of the momentum, $\mathbf{p}_{hidden}$, only arises in situations where the potential is velocity dependent. The neutrons total energy E therefore is a constant of motion. Neutrons decelerate (accelerate) when they are entering a material, and accelerate (decelerate) when leaving the material, depending on the sign of the scattering length. The phase shift $\Delta\phi$ caused by the nuclear potential, is of special interest in neutron interferometry. This phase shift for the optical like potential depends only on the action of the kinetic momentum:

$$\Delta\phi(\mathbf{r}) = \phi_{vacuum}(\mathbf{r}) - \phi_{matter}(\mathbf{r}) = \frac{1}{\hbar}\oint_{S} \Delta\mathbf{p}_{kin} \cdot d\mathbf{s}\,. \tag{2.35}$$

Combining $\mathbf{p} = \hbar\mathbf{k}$ and $n = \frac{|\mathbf{K}|}{|\mathbf{k}|}$ (Eqn. 2.24), the difference in the kinematic momentum $\Delta\ \mathbf{p}_{kin}$, can be written as

$$\Delta\mathbf{p} = \hbar\mathbf{k}(1-n) \tag{2.36}$$

and the phase shift is given by

$$\Delta\phi = k(1-n)D\,. \tag{2.37}$$

Where D is the effective path length of the neutron beam in the material. With Eqn. 2.28 this simplifies to

$$\Delta\phi = -Nb_c\lambda D\,. \tag{2.38}$$

Where N is the particle density, b_c the coherent neutron scattering length and λ the wavelength of the neutrons. The product of the particle density N and the coherent scattering length b_c is called the neutron Scattering Length Density (nSLD).

There are quite a few isotopes which have a negative coherent scattering length, for example manganese ^{55}Mn(-3.73 fm), hydrogen ^{1}H(-3.74 fm) and titanium ^{48}Ti(-6.08 fm). Thus the phase shift for neutrons passing through matter can be either positive or negative, depending on the sign of b_c. The reason why the coherent scattering length can be positive or negative is described in the following section.

2.5 Neutron scattering length and scattering cross section

In the previous section we saw that the phase shift for neutrons passing through matter is proportional to the scattering length. We also mentioned that there are a few isotopes

with negative scattering length, and the connection between the scattering length and the scattering cross section will be explained in this section.

In the quantum mechanical treatment of scattering, the scattering problem would appear to be a very difficult time-dependent problem. But it is possible to cast the problem into a time-independent, stationary-state problem that is much easier to solve. In this view, we consider a state of one particle corresponding to a plane wave at large distances that interacts with a fixed potential at the origin. The wave function $\psi(\mathbf{r})$ is the solution of the time-independent Schrödinger equation

$$\left(-\frac{\hbar^2}{2m}\Delta + V(\mathbf{r})\right)\psi(\mathbf{r}) = E\psi(\mathbf{r}), \tag{2.39}$$

where $V(\mathbf{r})$ is the potential causing the scattering, and E is the total energy in the center of mass (CM) system and m is the reduced mass. It is sufficient to assume that the scattering potential is a central potential $V(r)$. Given the z-axis of symmetry the wave function can be expressed in terms of Legendre polynomials P_l

$$\psi(\mathbf{r}) = R(r)\theta(\vartheta)\phi(\varphi) = R(r)\sum_{l=0}^{\infty}\sum_{m=0}^{\infty} Y_{l,m}(\vartheta,\varphi) = \sum_{l=0}^{\infty} R(r)P_l(cos\vartheta) \tag{2.40}$$

where $R(r)$ is the radial coefficient and $Y_{l,m}(\vartheta,\varphi)$ are the spherical harmonics. Eqn. 2.40 is called partial wave analysis. Only the radial function $R(r)$ in Eqn. 2.40 is responsible for the central potential $V(r)$. Substituting $u(r) = rR(r)$ into Eqn. 2.39 the radial function satisfy the one-dimensional Schrödinger equation

$$\frac{d^2u}{dr^2} + \frac{2m}{\hbar^2}\left[E - V(r) - \frac{l(l+1)\hbar^2}{2mr^2}\right]u = 0\,. \tag{2.41}$$

The additional term in the scattering potential is the repulsive centrifugal barrier potential $(\hbar^2/2m)(l(l+1)/r^2)$ which acts like it would repel particles with non-zero angular momentum. However, we will now consider the scattering of slow neutrons where the Schrödinger equation (Eqn. 2.41) can be simplified by assuming that $l = 0$. This assumption is justified by the fact that relative angular momentum between the neutron and the nucleus is quantized in units of $\hbar$, $mvr = l\hbar$, and $mvr << \hbar$ for slow neutrons. This assumption is valid when $v << h/mr$ and corresponds to a kinetic energy T given by

$$T = \frac{1}{2}mv^2 << \frac{\hbar^2}{2mR^2} \simeq 20MeV \tag{2.42}$$

where the impact parameter R is on the order of 1 fm. This is valid for neutron energies classified in Tab. 2.1. The simplified, $l = 0$, Schrödinger equation is

$$\frac{d^2u}{dr^2} + \frac{2m}{\hbar^2}\left[E - V(r)\right]u = 0\,, \tag{2.43}$$

For the purpose of the following analysis the potential $V(\mathbf{r})$ can be approximated by a simple square well potential, $V(r) = -V_0$, (see Fig. 2.3), since the short-range strong

interaction has a relativly sharp, well-defined cutoff. The wave function inside the potential, $r < R$, is

$$u(r) = A\, sin(\, k_i r + \epsilon_i) \tag{2.44}$$

where

$$k_i = \sqrt{2m(E - V_0)/\hbar^2} \tag{2.45}$$

is the wave vector inside the potential. The solution outside the potential, for $r > R$, is also of the form Eqn. 2.44, since in this region $V = 0$ and we do not consider bound states. Thus $E > 0$ and k is real .

The wave function outside the potential is given by

$$u(r) = B(\, sin\, k_o r + \epsilon_o) \tag{2.46}$$

where

$$k_0 = \sqrt{2mE/\hbar^2}. \tag{2.47}$$

Since we are only considering elastic scattering, i.e. no creation or destruction of particles, A in Eqn. 2.44 must equal B in Eqn. 2.46. All that can result from elastic scattering is a change in the phase of the outgoing wave. The other two unknowns, ϵ_i and ϵ_o must satisfying continuity at the potential barrier, $r = R$, in order that $u_i = u_o$ and $du_i/dr = du_o/dr$.

These conditions lead to a phase shift, $\epsilon = \epsilon_o$ - ϵ_i. As $V \rightarrow 0$ (in which cases no scattering occurs), $k_i \rightarrow k_o$ and $\epsilon \rightarrow 0$. This is just the free particle solution. The effect of V on the wave function is indicated in Fig. 2.6. The wave function at $r > R$ has the same form as the free particle, but it has experienced a phase shift ϵ. The nods of the wave function are "pulled" towards the origin by the attractive potential($\epsilon > 0$). A repulsive potential would "push" the nodes away from the origin and would give a negative phase shift ($\epsilon < 0$)[Kra1988].

This phase shift is linked total scattering cross section,

$$\sigma = 4\pi \frac{d\sigma}{d\Omega} \tag{2.48}$$

where dσ/dΩ is given by [Kra1988],

$$\frac{d\sigma}{d\Omega} = \frac{sin^2\epsilon}{k^2}\,. \tag{2.49}$$

The low-energy total scattering cross section σ is connected with the scattering length b by

$$\lim_{k\rightarrow 0} \sigma = 4\pi b^2\,, \tag{2.50}$$

where,

$$b = -\lim_{k\rightarrow 0} \frac{sin\epsilon}{k}\,. \tag{2.51}$$

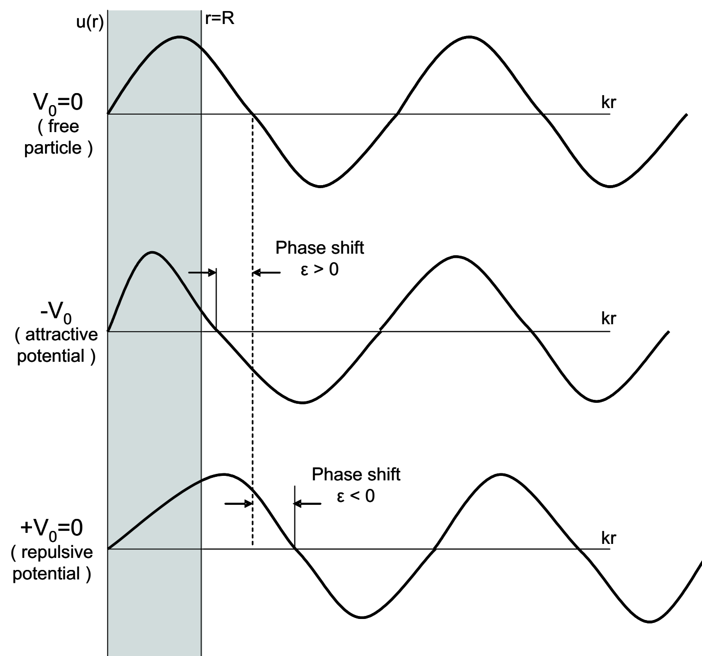

Figure 2.6: *The effect of a scattering potential is to shift the phase of the scattered wave at points beyond the scattering regions, where the wave function is that of a free particle.*

The choice of sign in Eqn 2.51 is arbitary, however it is conventional to choose the negative sign. After summing over spin states one obtains the coherent scattering length b_c. Thus since a nuclear potential may be attractive or repulsive, causing δ (and b) to have either sign, the coherent scattering length b_c may also be positive or negative. This is in contrast to the total scattering cross section which is always positive.

Chapter 3

Principles of grating interferometry

The principle of a grating based interferometer consisting of three diffraction gratings is explained in this chapter. In combination with a phase stepping approach it can be used to obtain differential phase contrast (DPC) images and quantitative phase information. The chapter is organized in the following manner: In section 3.1 the setup of the interferometer is described. Section 3.2 deals with the formation process of DPC images. The phase retrieval in combination with the phase stepping approach is described in section 3.3. In section 3.4 the coherence requirements on the radiation are given. Finally in section 3.5 simulations of phase contrast radiography images are shown.

3.1 Setup of the grating interferometer

The setup consists of an incoherent neutron source, a wavelength filter, the object, a spatially resolving neutron image detector and a grating interferometer, shown in Fig 3.1. The latter is comprised of three diffraction gratings: two absorption and one phase grating. The first grating is the source grating G_0 with the period p_0. This is an absorption grating with transmitting slits, placed close to the neutron beam exit port. The second grating is the phase grating G_1 with the period p_1 which is located on the optical axis at a distance l away from the source grating directly behind the object. The phase grating only modulates the phase of the neutron wave, and ideally does not attenuate the beam. The third grating is the second absorption grating, the analyzer grating G_2 with the period p_2, located at a distance d behind the phase grating on the optical axis. The design parameters for the gratings (structure heights and periods), the wavelength and the distances labeled in red in Fig. 3.1 are calculated in chapter 4. The fabrication of the gratings is described in chapter 5. The realization of the complete experimental setup is given in chapter 6.

3.2 Formation of differential phase contrast images

In the next three subsections the role and impact of each grating concerning the formation of the differential phase contrast images is explained. For a better understanding the image formation mechanism with two gratings, the phase and the analyzer grating

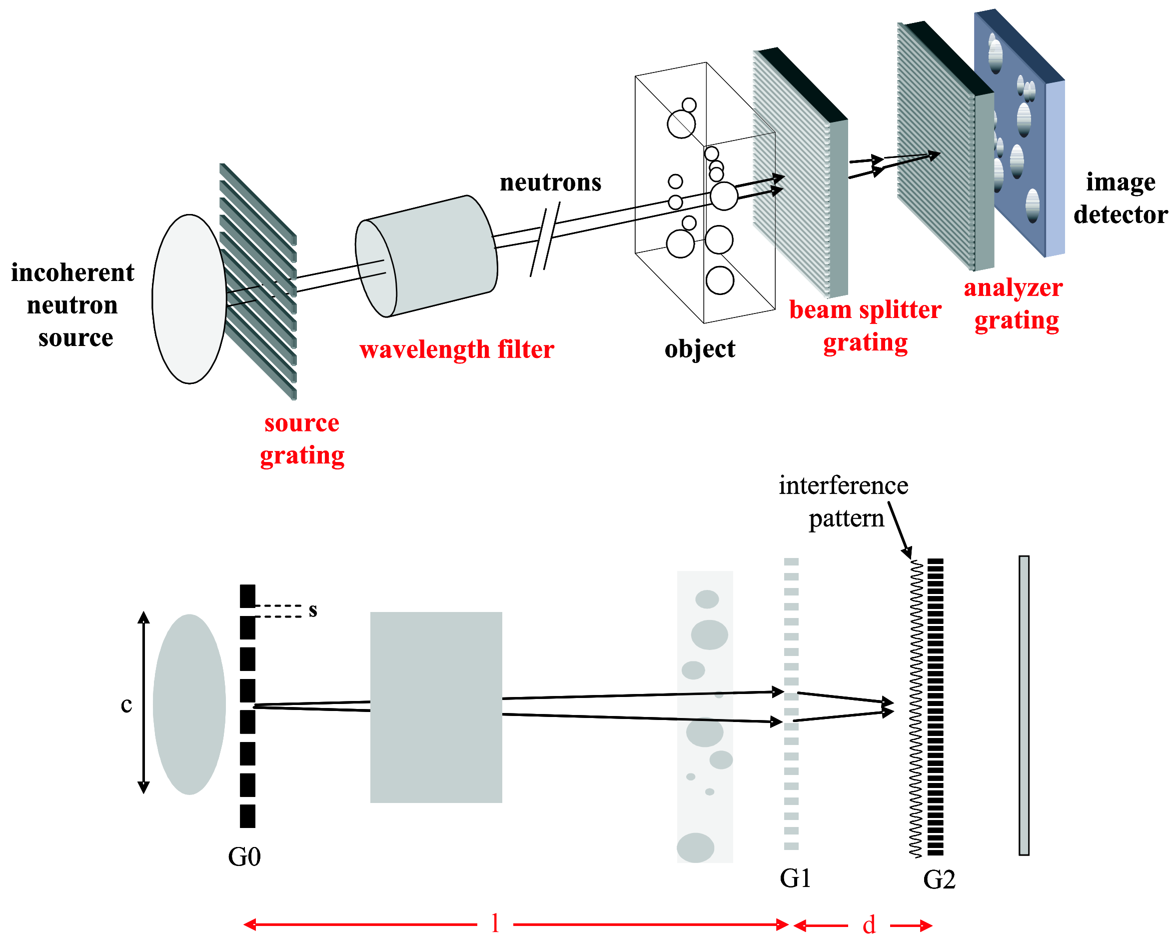

Figure 3.1: *Setup of the grating based neutron interferometer. It consists of the source grating G_0, a wavelength filter, an object, the phase grating G_1, the analyzer grating G_2 and an image detector. Courtesy of Christian David and Franz Pfeiffer*

is first described. The role of the source grating to the image formation mechanism is given afterwards. The function of the phase the analyzer and the source grating are described in subsections 3.2.1, 3.2.2 and 3.2.3 respectively.

The accomplishment of the DPC images is based on detecting perturbations of the incident wave front, induced by refraction on a phase object in the beam. This leads to a local displacement of the interference pattern. The objective of the grating based interferometer is to detect the local position of the fringes and determine from these the phase shift induced by the object [Dav2002] [Wei2004] [Wei2005] [Pfe2006a]. All these cited paper describe the grating based X-rays experiments. The DPC image formation process achieved by the grating interferometer is similar to Schlieren imaging or to a Shack-Hartmann wave front sensor [Bor1980].

3.2.1 Function of the phase grating G_1 - fractional Talbot effect

The phase grating G_1 is constructed in such a way that it divides the incoming beam basically into the two first (± 1) diffraction orders [Goo2004]. The conditions for this are:

- grating lines must have negligible zero absorption.
- bars of the Si grating must shift the phase by odd multiples of π.
- DC[1] of 0.5.

In this case, 81% of the incoming intensity are diffracted into the positive and negative first orders, which are used to generate the signal. This arises from the fact, that the $\pm$ first Fourier components of a rectangular phase modulating box-profile each carry 40.5 % of the diffracted intensity. The remaining 19 % go into higher orders, inevitable for a box-profile phase grating structure. The intensity of the zeroth order of the ideal phase grating with a box-profile is zero. The wavelength of the illuminating neutrons is on the order of several Å, i.e. much smaller than the grating period (a few μm). Therefore the angles between the two diffraction orders are small (mrad) that they overlap almost completely. In the overlapping region downstream of the phase grating, the diffracted beams interfere and form linear periodic interference fringes in the planes perpendicular to the optical axis at a distance d from G_1. For a spherical incident wave, i.e. for radiation coming from a single line source s at a distance l as indicated in Fig. 3.1 the period of the interference pattern is equal to

$$p_2 = \frac{1}{2} p_1 \frac{(l+d)}{l}, \tag{3.1}$$

for neutrons waves coming from a source at a distance l. If $d \ll l$, which is the case for our experiment, the period p_2 of the interference fringes is about half of the period p_1. Notice that the period of the interference fringes does not depend on the wavelength of the radiation used.

The contrast of the interference pattern changes periodically as a function of the inter-grating distance d along the optical axis. This phenomenon is related to the Talbot[2] self-imaging effect. A nice overview is given in the paper from [Arr2000]. For an incoming plane wave and a pure phase grating of period p_1 and DC$= 0.5$ whose lines shift the phase by π, the contrast is strongest when

$$d_n = n \cdot \frac{p_1^2}{8\lambda}, \tag{3.2}$$

for odd n and vanishes for even n. A simulation of the field amplitude distribution behind the phase grating is shown in Fig. 3.2. For a spherical incoming wave with a

[1] Duty cycle is defined by the ratio of the trench width to the period of a grating.

[2] The Talbot effect was first observed by the English scientist Henry Fox Talbot (1800-1877). The phenomenon of Talbot self-imaging is caused by Fresnel diffraction of a grating in the near field. The basic equation used to describe the Talbot effect is the Fresnel diffraction integral.

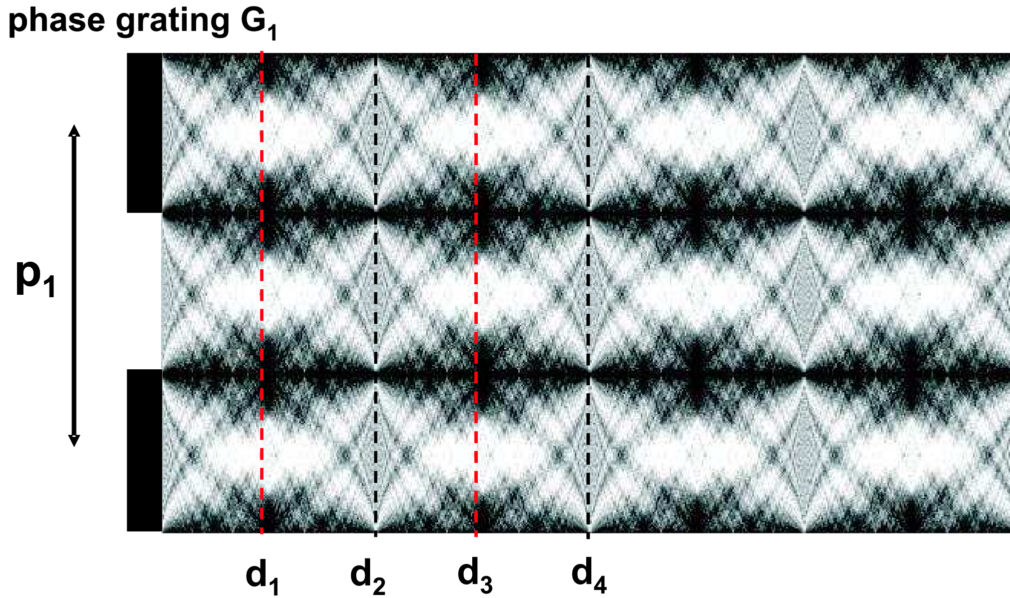

Figure 3.2: *Simulated near field amplitude distribution after an ideal phase grating for an incident plane wave. The red dashed lines are the Talbot planes (odd n) with maximum contrast. The contrast vanishes for Talbot planes with even n. Courtesy of Franz Pfeiffer.*

radius l, the expression in Eqn. 3.2 has to be modified to [Wei2005],

$$d_{n,sph.} = \frac{l \cdot d_n}{l - d_n} = \frac{l \cdot n \cdot \frac{p_1^2}{8\lambda}}{l - n \cdot \frac{p_1^2}{8\lambda}} . \tag{3.3}$$

For $l \gg d_n$, the difference between d_n and $d_{n,sph.}$ is very small.

3.2.2 Function of the analyzer grating, G_2

The periodicity of the phase grating and thus the spacing of the interference fringes does not exceed a few microns. Hence a detector placed in the Talbot plane will generally not have sufficient resolution to resolve the fringes. Therefore, the analyzer grating G_2 with the same periodicity and orientation as the fringes is placed in the first Talbot plane just before the detector (Fig. 3.1). For a plane wave, $p_2 = p_1/2$. For optimum performance, the transmission of the absorber lines should be as low as possible, and the duty cycle should be 0.5.

When the analyzer grating is placed into the interference fringe pattern of the empty setup (without an object), then the transmitted intensity depends on the relative position between the fringes and the grating lines. When the maxima of the interference

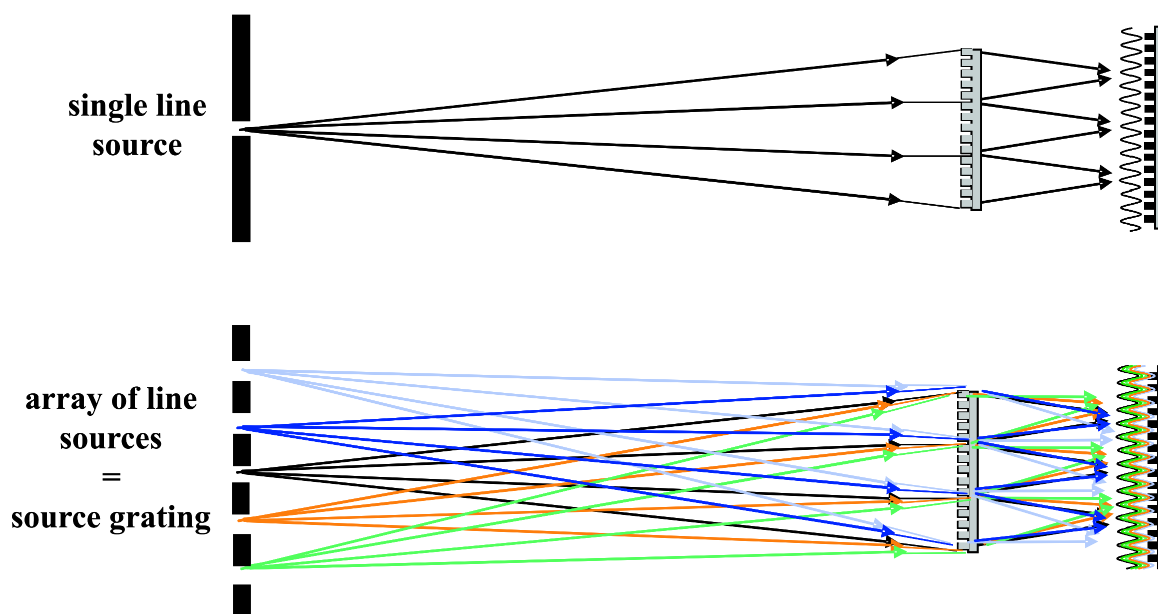

Figure 3.3: *The source grating creates an array of N individually coherent but mutually incoherent sources. The interference pattern created in each line source superimpose congruently. Therefore the flux density is increased by a factor N compared to a single line source. Courtesy of Christian David and Franz Pfeiffer.*

fringes coincide with the absorbing grating lines, the transmitted intensity reaches a minimum, whereas a maximum is reached, when the maxima of the interference fringes coincide with the transmitting gaps between the absorbing lines. If the position of the analyzer grating is chosen such, that the transmitted intensity is close to the middle, then a local distortion of the interference fringes will cause a change in the local transmission proportional to fringe distortion. This analyzer grating therefore acts as a transmission mask for the detector and transforms local fringe position into signal intensity variation. The detected signal profile thus contains quantitative information about the phase gradient of the object. To separate this phase information from other contributions to the signal, such as diffraction on the sample (in-line phase contrast) as well as attenuation in the sample inhomogeneous illumination or imperfections of the gratings, the phase-stepping approach used in other interferometry methods [Wei2005] was adapted to this setup. It is explained in section 3.3. The following subsection describes a setup that can record phase contrast images with much higher flux density.

3.2.3 Function of the source grating, G_0

The source grating G_0 is an array of N absorbing lines that is placed close to the neutron beam exit port. It creates for the image formation mechanism an array of N individually coherent line sources that are mutually incoherent as shown in Fig.3.3. The coherence requirements on the source grating is explained in section 3.4 Since G_0 can contain a large number of individual lines, each creating a virtual source, efficient use can be made of typical neutron source sizes of more than a few square centimeters. Such a

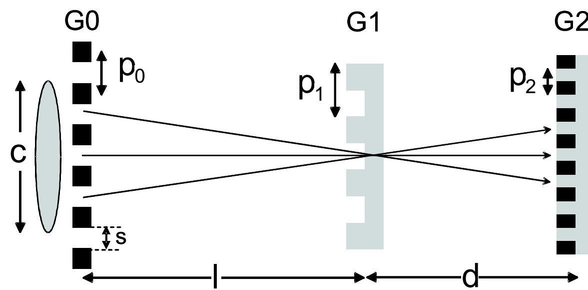

Figure 3.4: *Intercept theorem which holds for the grating interferometer [Pfe2006b].*

grating makes it possible to use the interferometer with a source of size c (Fig. 3.1) that provides low spatial and low temporal coherence [Pfe2006a]. More detailed information about the coherence requirement are discussed in section 3.4.. However, it is important to note that the total source size c determines the sharpness in the final image, which is given by $c \cdot d'/l$, where d' is the distance form the object to the analyzer grating. Thus G_0 decouples spatial resolution from spatial coherence.

The spacing of neighboring source lines (period p_0) is chosen such that the shift of the interference patterns created by two neighboring virtual line sources along the direction perpendicular to the grating lines exactly matches the periodicity of G_2. This condition is fulfilled for the intercept theorem shown in Fig. 3.4:

$$p_0 = p_2 \frac{l}{d}, \tag{3.4}$$

The duty cycle DC=s/p_0 of the source array determines the degree of transverse coherence in the direction perpendicular to the interferometer grating lines, where s is the width of the transmitting slits as shown in Fig. 3.4. The setup with the source grating increases the total flux by a factor N compared to a single line source and thus shortens the exposure times by a factor N.

3.3 Phase retrieval by interferometric phase-stepping

A phase object in the beam will cause a distortion of the incident wave front, and that in turn will cause a local displacement of the interference fringes as shown in Fig. 3.5. As already mentioned, the fundamental idea of the method presented here is to detect the local positions of the fringes and determine from these the phase shift induced by the object. When one of the gratings, e.g. the analyzer grating[1] as indicated in Fig. 3.5 is scanned along the transverse direction x_g, the intensity signal I(x,y) in each pixel (x,y) in the detector plane oscillates as a function of x_g (Fig. 3.6 e). The phases of the intensity oscillations) in each pixel ϑ(x,y) (Fig. 3.6 e) are related to the wave front

[1] In the experiment the phase-stepping was performed with the source grating G_0 over one period. Due to the fact that the phase stepping over one period of G_0 is much coarser in comparison to one period of G_2, it has to be performed with l/d times less precision.

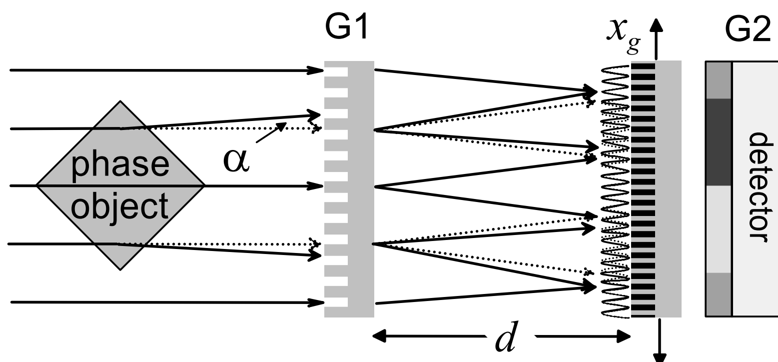

Figure 3.5: *A phase object in the incident beam will cause a slight refraction, which results in changes of the locally transmitted intensity through the analyzer grating [Pfe2006b].*

phase profile Φ(x,y), the neutron wavelength λ and the period of p_2 by [Wei2004]

$$\vartheta(x,y) = \frac{\lambda d}{p_2}\frac{\partial \Phi}{\partial x}. \tag{3.5}$$

The recorded image is therefore a differential phase contrast image. The interferometer phase ϑ(x,y) contains no other contributions, particularly no absorption contrast. The phase profile of the object can thus be retrieved from ϑ(x,y) by a simple one-dimensional integration

$$\Phi(x,y) = \int dx\, \vartheta(x,y)\frac{p_2}{\lambda d}, \tag{3.6}$$

assuming that the constraints are know. These are that the interferometer phases outside the objects are zero. In the general case where the wave front impinging on the object already shows some distortion, the background phase distribution Φ_{back}(x,y) should be measured with the object removed from the beam and then subtracted (flat-field correction).

Another quantity obtained by a phase-stepping scan is the average signal for each pixel over an entire oscillation a(x,y) (Fig. 3.6 e). It is identical to the transmission radiography signal as it would be measured in a radiograph taken without the interferometer. A single phase-stepping scan thus yields the DPC image the phase image and the attenuation image.

In practise, $a(x,y)$ and $\vartheta(x,y)$ are extracted by evaluating the amplitude of the zeroth and the phase of the first component of a discrete Fourier transform of the phase stepping intensity values for each pixel in the image.

3.4 Coherence requirements

The phase of a wave cannot be measured directly, so any conversion of a phase shift into an intensity modulation must depend on the interference of two (or more) waves.

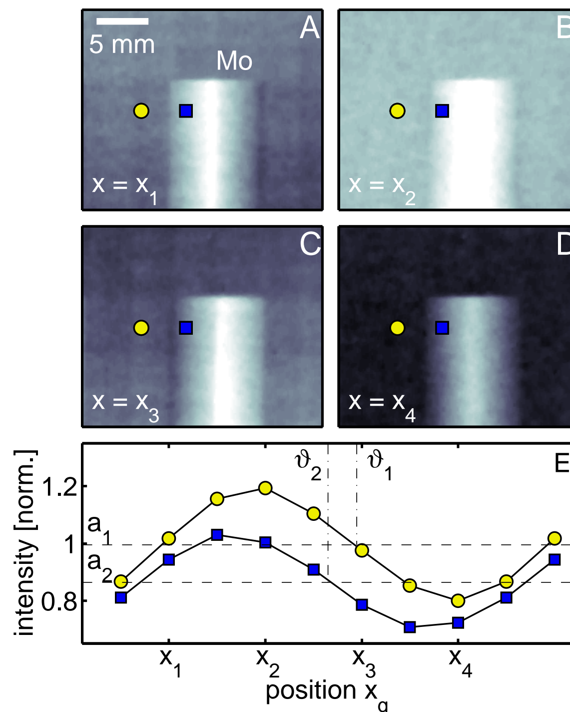

Figure 3.6: *Principle of phase-stepping. (A-D) Raw image data of a quadratic Molybdenum (Mo) metal rod rientated like in Fig. 3.5, taken at different positions* $x_g = x_1, ..., x_4$ *of the analyzer grating* G_2*. (E) Intensity oscillations in two detector pixels as a function of* x_g *[Pfe2006b].*

In order to be able to interfere constructively or destructively, the waves need to have a well-defined phase relation in time and space, i.e. sufficient temporal (longitudinal) coherence and spatial (transverse) coherence [Lip1995].

Temporal coherence is related to the monochromaticity of the radiation. For radiation of a bandwidth of $\Delta\lambda$ around a central wavelength λ, the longitudinal coherence length is $\frac{\lambda^2}{\Delta\lambda}$. Consider two beams originating from the same source point that are superimposed after taking different paths through an optical setup. These beams only have a well-defined phase relation if the difference in optical path lengths is shorter than the longitudinal coherence length. While for visible laser light $\frac{\lambda^2}{\Delta\lambda}$ can extend over many meters, it is only on the order of nanometers for neutron beams.

Neither the period nor the lateral position of the interference pattern in our grating ingerferometer depend on the wavelength of the radiation used. In this sense the described setup is achromatic allowing for the use of broadband radiation from a neutron source without the need of monochromators that would only transmit a small fraction of the used radiation. However, three aspects of the interferometer setup do depend on the neutron wavelength. First, the phase shift of the neutron wave passing through the grating lines of G_1 depends on the neutron energy due to the dispersion in the grating material (Eqn. 2.38). The condition to induce a phase shift equal to odd multiples of π is not strict, and a radiation within a certain energy band in the order of $\pm 10\%$ around the design energy can be accepted. A deviation from phase shift π only affects

the contrast, but it does not change the interference pattern qualitatively. Second, the position of the Talbot planes (Eqn. 3.2) depends on the neutron wavelength and therefore the neutron energy [Wei2004]. The simulated field distribution in Fig. 3.2 was calculated for one wavelength. Taking a wavelength distribution into account the field distribution will smear out. Third, the absorption cross section is velocity dependent (Eqn. 2.5) and therefore wavelength dependent. The smaller the wavelength the thicker the absorption materials of the source grating and the analyzer grating have to be.

Spatial coherence is related to the size and distance of the source. Let us consider an intrinsically incoherent and chaotic source of a size w emitting at a wavelength λ. At a distance l from the source, the wave front phase difference between two points lying in a plane normal to the optical axis and separated by a distance r is only then well defined when the condition $r < \lambda \cdot l/w$ is fulfilled. $t = \lambda \cdot l/w$ is called the transverse coherence length.

Our described setup requires spatial coherence only in the direction perpendicular to the optical axis and to the grating lines. In this direction the minimum required coherence length t is given by

$$t = 4d\frac{\lambda}{p_1}\,. \tag{3.7}$$

If G_2 is placed in the first fractional Talbot plane, then t=$p_1/2$. For a phase grating period of 8 μm the transverse coherence length t is 4 μm. Thus the size of an individual source s (Fig. 3.1) emitting at wavelength $\lambda = 0.4$ nm and placed at a distance $l = 5$ m from the beam splitter grating should be smaller than 0.5 mm. The use of a smaller source will increase the spatial coherence, resulting in an improvement of the fringe visibility[1]. As there are no limitations in terms of coherence in the direction along the grating lines, a line source can be used.

3.5 Simulations of phase contrast radiography images

The objects chosen for the simulation and later used in the experiment are metal rods with a quadratic profile. The edge length of the rods is 5 mm. For the simulation, the rods are placed with one edge facing the incoming beam as shown in Fig. 3.5. For the simulation we choose four rods of different materials. The rods are chosen to have small attenuation coefficients μ and therefore negligible absorption. Thus they are almost invisible in the transmission image. But they are chosen to have large real parts δ of the refractive index (see Eqn. 2.29). The δ value is directly linked to the coherent scattering length b_c and therefore to the phase shift (see Eqn. 2.38). That means the rods which are invisible in the transmission image are visible in the phase image. A plot of δ versus μ is shown in Fig. 3.7. Three materials, Lead (Pb), Molybdenum (Mo) and Magnesium (Mg) were the chosen materials with small μ but large positive δ. This leads to a negative phase shift according Eqn. 2.29 and Eqn. 2.37. The fourth material is Titanium (Ti) which has a negative δ, and this leads to a positive phase shift.

[1] More information about the visibility is given in chapter 6.

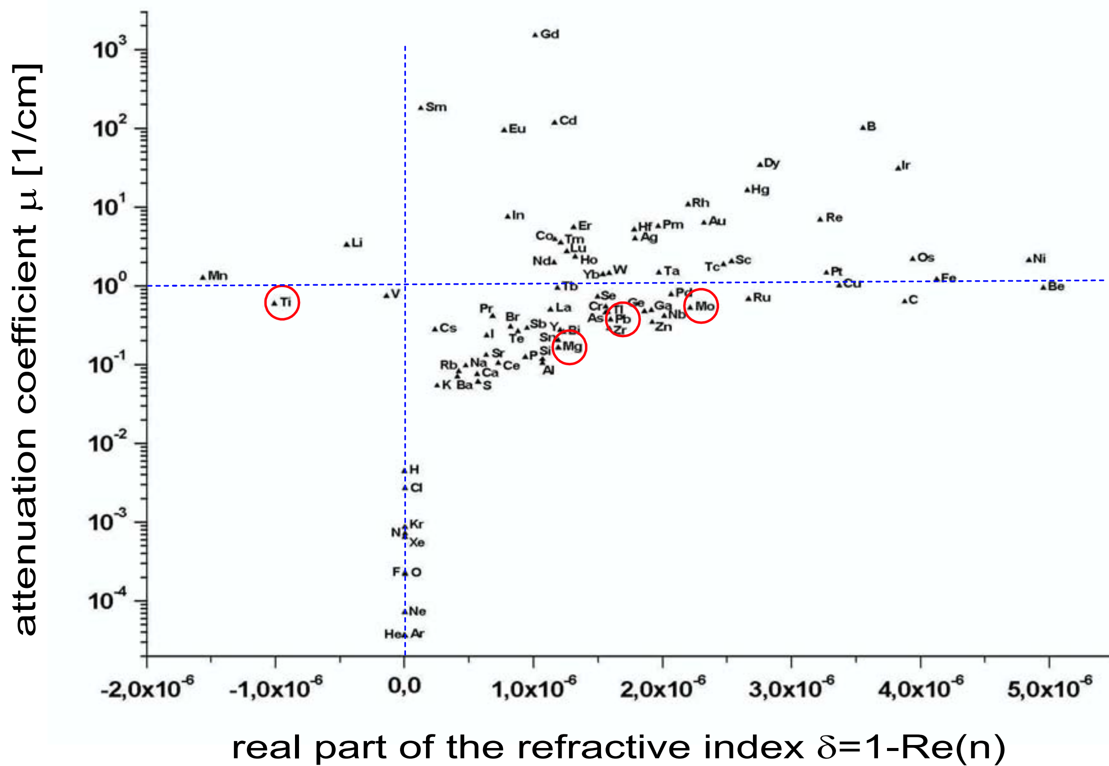

Figure 3.7: *Plot of attenuation coefficient versus real part of the refractive index for different elements [NCNR92]. The elements marked with red circles are the ones used in the simulation and later in the experiment. Courtesy of Klaus Lorenz (FRM-II in Munich)*

The simulation of the neutron radiographies contains three images. They are calculated for a wavelength of 4.1 Å. The first one is the transmission image which serves as comparison image that one would obtain without the three diffraction gratings in the beam. The second image is the differential phase contrast (DPC) image. This is the image which is extracted from the phase stepping scan (see section 3.3). The third image is the phase image. In the experiment it is obtained by integrating the DPC image. Fig. 3.8 shows the result of the simulation of these three images.

The image on the left shows the simulated transmission image. Due to the different attenuation coefficients of the materials differences in the transmitted intensity are observed. In addition the profiles across the corresponding images are shown. They yield precise qualitative information about the objects. The section profile gives the values of the transmission[1] of the four rods: 51% (Ti), 99% (Pb), 77% (Mo), 99 % (Mg). Notice, that the Pb and Mg rod are not visible in the transmission image. This is due to their large attenuation length. Furthermore, it is not easy to distinguish materials with almost identical attenuation coefficients in the transmission image, like Pb and Mg. The image in the middle shows the simulated DPC image. It is obtained by calculating the phase shift through each rod (Eqn. 2.38) and then differentiating the

[1] The formula for the calculation of the transmission is described in section 4.1.4

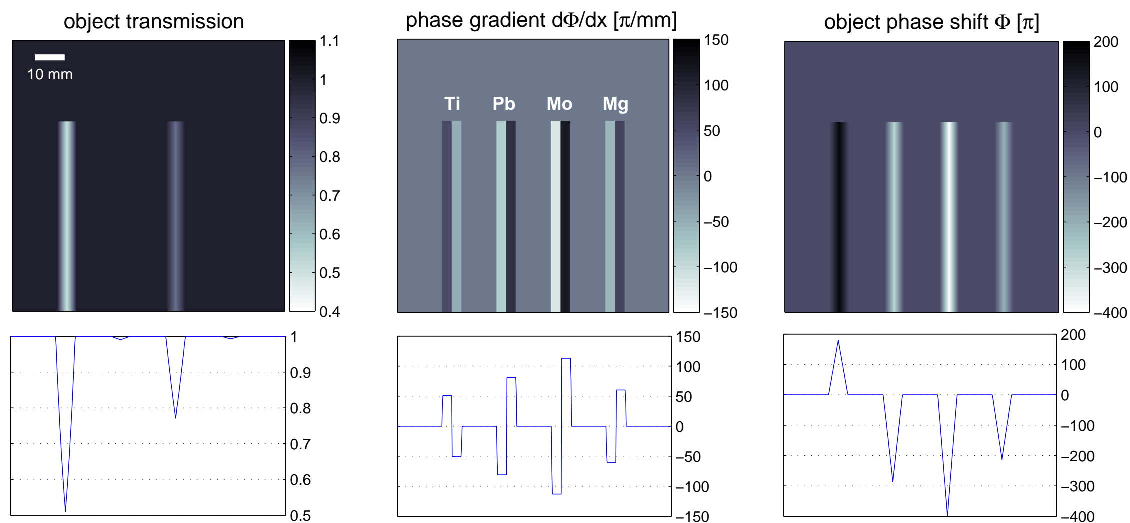

Figure 3.8: *Linear contour plots and section profiles of the simulated data for the four metal rods (Ti, Pb, Mo, Mg) with a quadratic profile and an edge length of 5 mm. The rods are placed with one edge facing the incident beam as shown in Fig. 3.5. (left) Conventional neutron transmission image. (middle) Differential phase contrast image* $d\Phi/dx$*. (right) Integrated phase shift* $\Phi(x, y)$ *retrieved from* $d\Phi/dx$ *by integration. The images are represented on a linear grey scale. They are calculated of* $\lambda = 4.1$ Å

phase shift along the direction perpendicular to the rod. Since the vector component of the phase gradient in the direction perpendicular to the grating lines is constant, but of opposite signs for both sides of the rods, they appear dark and bright. Due to the fact that Ti has a negative coherent scattering length and therefore a refractive index greater than unity, the sides of the Ti rod have opposite signs of the phase shift than the other rods . The section profile through the DPC image gives the values for the phase gradient $d\Phi/dx$:$\pm$ 51 (Ti), $\mp$ 81 (Pb), $\mp$ 116 (Mo), and $\mp$ 61 (Mg) [π/mm]. In the DPC image it is possible to visualize these rods which are not observable in the transmission image. In addition, the section profile of the DPC image one gets quantitative information about the phase gradient and thus can distinguish the rods with roughly same μ like Pb and Mg. The image on the right side shows the phase shift for each of the four rods. It is interesting to note that Ti has a positive phase shift. Therefore the Ti rod appears dark instead of bright as the other three rods. The maximum values in the section profile are: 180 (Ti), -286 (Pb), -400 (Mo), -213 (Mg) [π].

Recapitulating one can say that the DPC image and the phase shift image provide additional new information to the conventional transmission image. With our grating interferometer we are therefore simultaneously able to image the complementary information of both the attenuation and the phase shift as plotted in Fig. 3.7.

Chapter 4

Design of the grating interferometer

In this chapter the design parameters for the three diffraction gratings and the setup are calculated. For the gratings these are the values for the periods (p_0,p_1,p_2) and the structure heights (h_0,h_1,h_2). For the setup these are the inter grating distances d and l. The values for the periods and distances are calculated in section 4.1 with respect to the setup described in the previous chapter. The interferometer is designed for the layout of the ICON beam line at PSI where the experiment was performed. The wavelength for the experiment was adjusted using a velocity selector, which is described in section 4.2. The structure heights are calculated to match the selected wavelength in section 4.3. For the calculations of the periods, the inter grating distances and the structure heights, three parameters are given. These are the period p_2 of the analyzer grating, the inter grating distance l and the wavelength λ.

4.1 Grating periods and inter grating distances

To observe the diffraction pattern generated by a spherical wave behind the beam splitter grating G_1, the analyzer grating G_2 should be placed at a Talbot distance $d_{sph,n}$ (Eqn. 3.3). The connection between the Talbot distance d_n for a plane wave and the Talbot distance $d_{sph,n}$ is given by

$$\frac{1}{d_n} = \frac{1}{l} + \frac{1}{d_{sph,n}} \,. \tag{4.1}$$

This equation is the analogue to the well know lens equation. Therefore the Talbot distance for a spherical wave originating form a source at distance l is given by

$$d_{sph,n} = \frac{l d_n}{l - d_n} = \frac{l \cdot n \cdot \frac{p_1^2}{8\lambda}}{l - n \cdot \frac{p_1^2}{8\lambda}}. \tag{4.2}$$

The triangle intercept theorem holds for the transverse scaling of the diffraction pattern. The image is magnified by a factor of M (Fig. 3.4):

$$M = \frac{l + d_{sph,n}}{l} \overset{(4.2)}{=} \frac{l}{l - d_n} = \frac{d_{sph,n}}{d_n} \,. \tag{4.3}$$

From Eqn. 3.4 we can express the distance l as

$$l = \frac{p_0}{p_2} \cdot d_{sph,n} \,. \tag{4.4}$$

Inserting Eqn. 4.2 for d_{sph}, l is given by

$$l = \frac{p_0}{p_2} \frac{l d_n}{l - d_n} \quad \Rightarrow \quad l = d_n \cdot \left(\frac{p_0}{p_2} + 1 \right) . \tag{4.5}$$

The magnification of the image can also be expressed in terms of the period p_2 of the analyzer grating and the period p_1 of the beam splitter grating as

$$M = \frac{2p_2}{p_1} \stackrel{(4.3)}{=} \frac{d_{sph,n}}{d_n} \,. \tag{4.6}$$

Equating Eqn. 4.5 and Eqn. 4.4 leads to

$$\frac{d_{sph,n}}{d} = \frac{p_0 + p_2}{p_0} \tag{4.7}$$

and together with Eqn. 4.6, the period of the phase grating is

$$p_1 = \frac{2p_0 p_2}{p_0 + p_2} \,. \tag{4.8}$$

The first Talbot distance (n=1) behind the phase grating is then given by

$$d_1 = \frac{p_1^2}{8\lambda} = \left(\frac{p_0 p_2}{p_0 + p_2} \right)^2 \cdot \frac{1}{2\lambda} \tag{4.9}$$

and this can be used in Eqn. 4.5 to obtain the distance l as a function of the two periods p_0 and p_2:

$$l = \frac{1}{2\lambda} \cdot \left(\frac{p_0 p_2}{p_0 + p_2} \right)^2 \cdot \left(1 + \frac{p_0}{p_2} \right) \; = \; \frac{1}{2\lambda} \cdot \frac{p_0^2 p_2}{p_0 + p_2} . \tag{4.10}$$

The period of p_0 is obtained by solving Eqn. 4.10:

$$p_0 = \frac{\lambda l}{p_2} + \sqrt{\left(\frac{\lambda l}{p_2} \right)^2 + 2\lambda l} \,. \tag{4.11}$$

With the given parameters p_2, l and λ, it is possible to calculate p_0 from Eqn. 4.11. With the knowledge of p_0 and Eqn. 4.8 the period p_1 is calculated. From the knowledge of p_1, the first Talbot distance d is calculated using Eqn. 4.9.

The period p_2 of the analyzer grating G_2 is fixed to $p_2 = 4\mu$ m due to the fabrication process. The distance l between the source grating G_2 and the phase grating G_1 is given by the layout of the beam line (Fig. 4.1) as the distance from the beam shutter to the first experimental place. The resulting length for l is 5.239 m. The neutron wavelength λ was chosen to be 4.1 Å. This is explained in the next section. With the

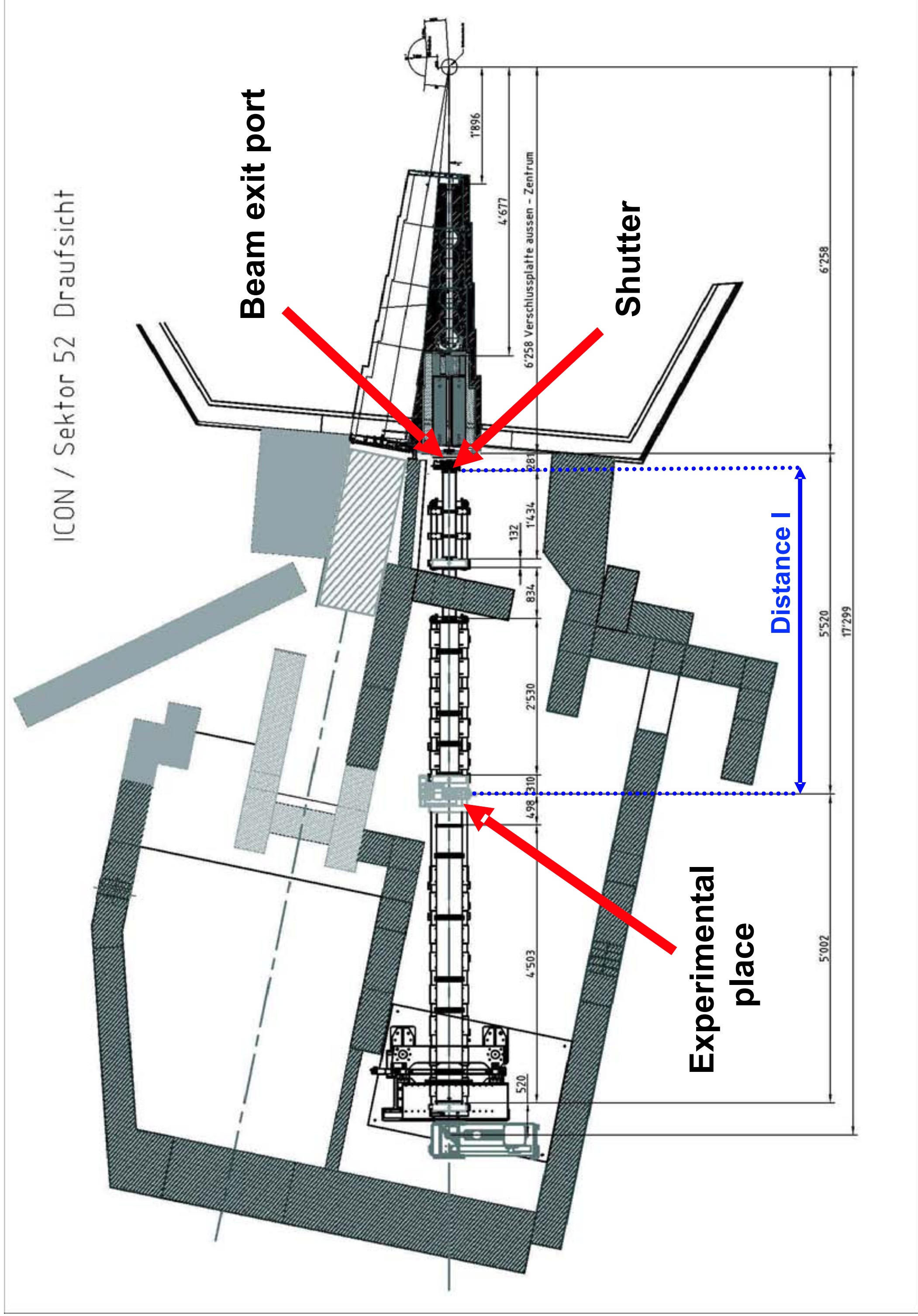

Figure 4.1: *Layout of the ICON beam line at PSI [ICON].*

given parameters, the values of the calculated periods and the first fractional Talbot distance are:

$$\begin{aligned} p_0 &= 1076\ \mu m\,, \\ p_1 &= 7.97\ \mu m\,, \\ d_{sph.} &= 19.4\ mm\,. \end{aligned}$$

4.2 Wavelength selection

With respect to structure heights (section 4.3) and therefore the fabrication processes, the wavelength is chosen with a velocity selector to λ =4.1 Å. The velocity selector consists of a horizontally rotating cylindrical drum with narrow slits in which the neutrons can pass through (see Fig. 4.2)[Ris1980].

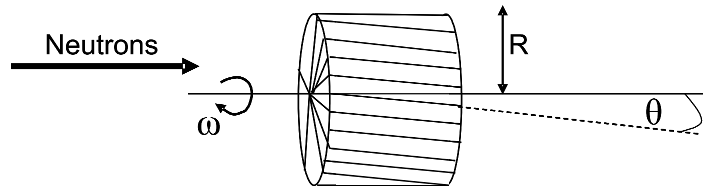

Figure 4.2: *Draft of a velocity selector.*

The slits form an angle of $\theta = 1.27°$ with respect to the optical axis. When the drum is rotating with a constant frequency ω it allows only neutrons of wavelengths in a band $\Delta\lambda$ around the optimum value λ to pass through. A neutron wavelength band is chosen by rotating the cylinder with a certain velocity

$$v = 2\pi R\omega \tag{4.12}$$

where R is the radius of the drum (R=8.3cm). The transmitted wavelength is then given by

$$\lambda = \frac{h\theta}{\omega R m}\,, \tag{4.13}$$

where h is Planck's constant and m is the mass of the neutron. The measured spectrum[1] of the ICON beam line without a velocity selector is shown in Fig. 4.3. Measurements of the wavelength distribution at the ICON beam line for various rotaton frequencies ω of the drum, are shown in Fig. 4.4. A more precise calibration of ω to achieve the mean wavelength is shown in Fig. 4.5. To obtain λ = 4.1 Å, the rotating frequency of the velocity selector was set to ω = 34 Hz. The wavelength distribution FWHM (Full Width Half Maximum) is $\frac{\Delta\lambda}{\lambda} \simeq 20\%$. It is therefore acceptable concerning the temporal coherence requirements discussed in section 3.4 . The wavelength was chosen

[1]Courtesy of Gabriel Frei and Guido Kühne.

as a compromise between the producibility of the three gratings and the neutron flux. The former condition sets a lower and the latter an upper limit for the wavelength. The influence of the wavelength on the grating structure heights is discussed in the next section.

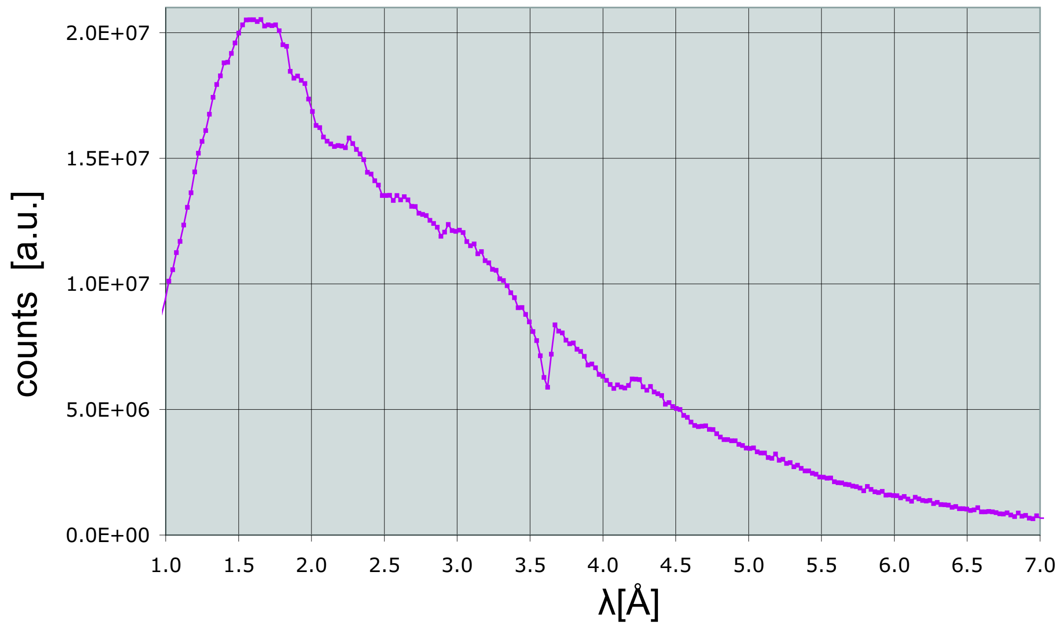

Figure 4.3: *Measured wavelength spectrum of the ICON beam line.*

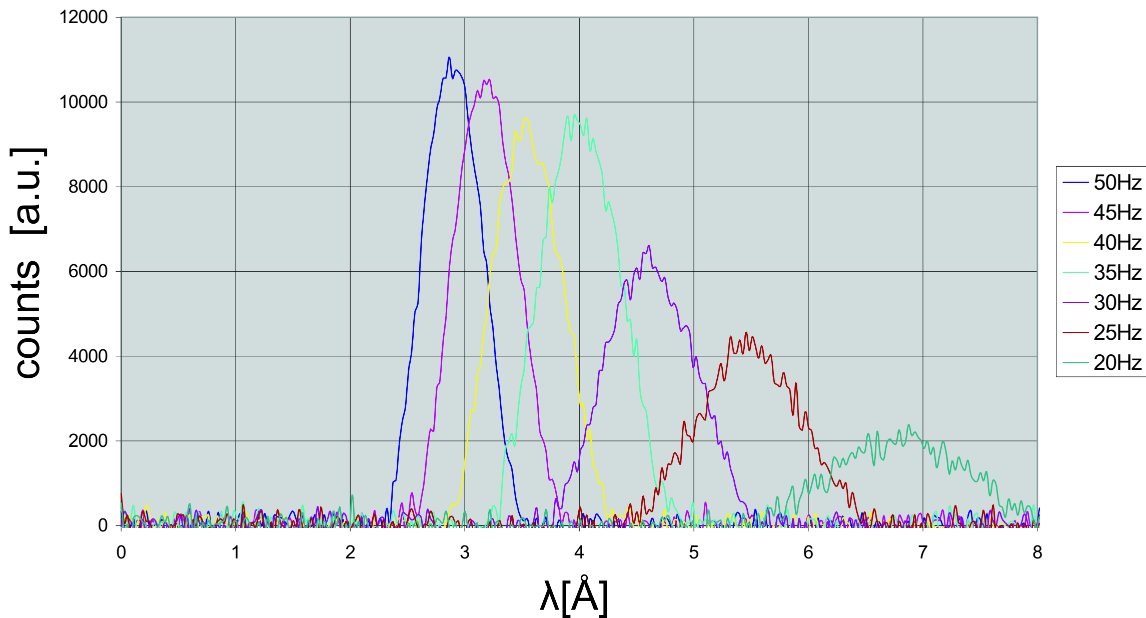

Figure 4.4: *Measured wavelength spectrum for different rotating frequency ω of the velocity selector drum.*

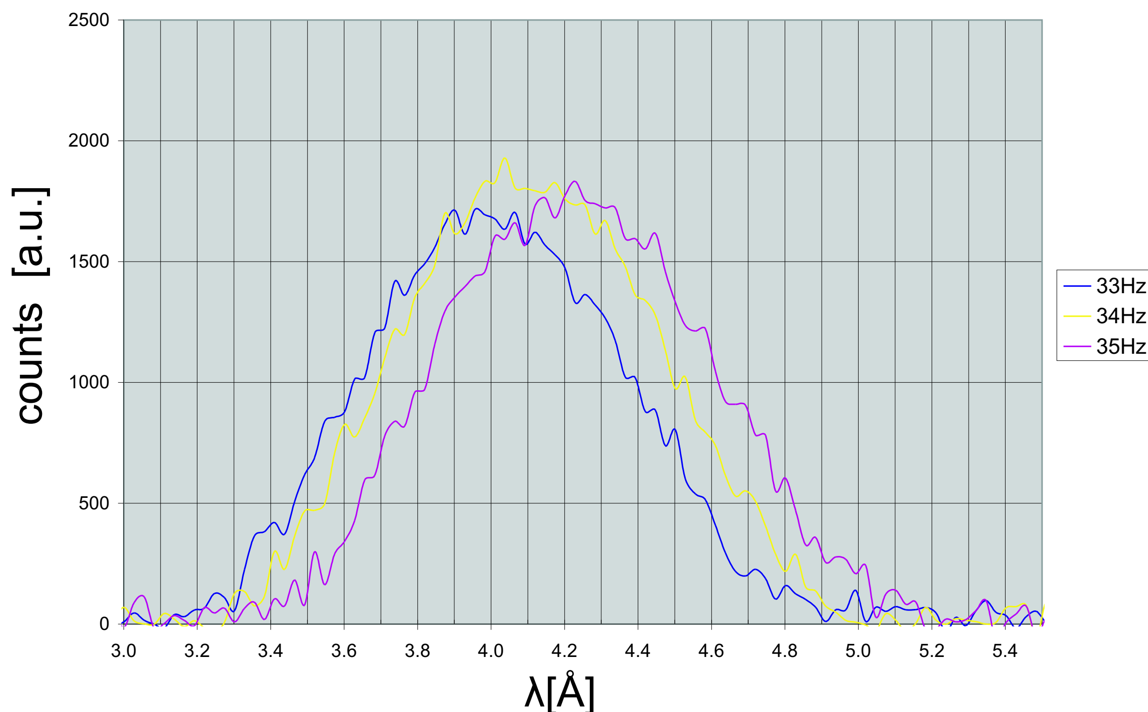

Figure 4.5: *Calibration measurements of the rotating frequency ω to achieve $\lambda = 4.1\AA$.*

4.3 Structure heights of the gratings

In the setup described in section 3.1, G_0 and G_2 represent the absorption gratings and G_1 represents the phase grating. As described in section 3.2.3, the source grating G_0 is an array of absorbing lines and transmitting slits. For optimum performance the absorber lines should have as little transmission as possible. A very good absorbing material for thermal neutrons is Gadolinium[1] (see Tab. 2.2 in subsection 2.2.1). Gadolinium has an attenuation length[2] of 2.92 μm for λ =4.1 Å. Silicon for instance has at the same wavelength an a_l-length of 50.9 cm. a_l is calculated as

$$a_l = \frac{1}{\sigma_t} \tag{4.14}$$

where σ_t is total cross section (coherent, incoherent scattering and absorption) per unit volume (in units of cm^{-1}). The transmission as a function of material thickness d is calculated as

$$T(\lambda) = (exp[d/a_l])^{-1}. \tag{4.15}$$

The transmission of neutrons with different wavelengths through Gadolinium layer with thicknesses of multiples (n=1,2,3,4) of a_l-length are plotted in Fig. 4.6.

[1] Gd has the highest thermal neutron capture cross-section of any known elements. The Gd used for the grating fabrication is the natural one, a mixture of all existing isotopes.

[2] The attenuation length is the thickness of a material that will attenuate a neutron beam to 1/e of its incident intensity. We will abridge it from now on with a_l for attenuation length

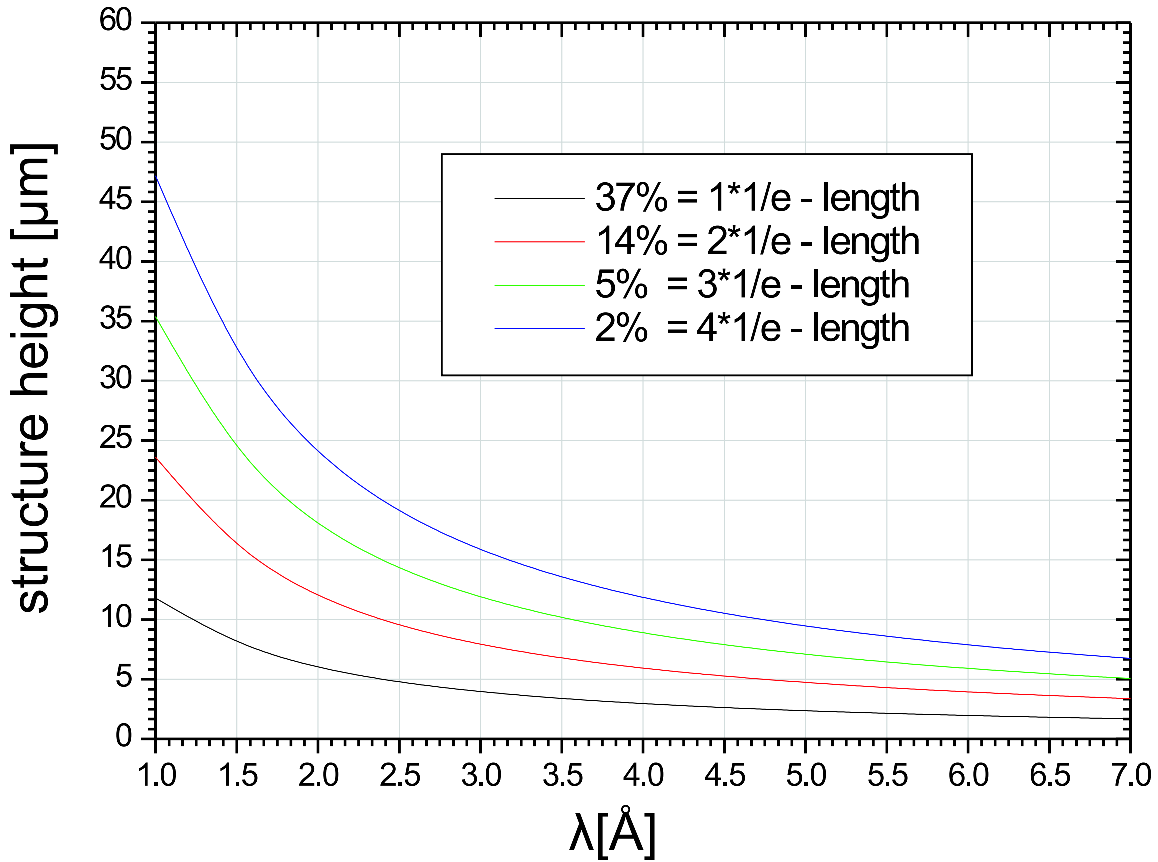

Figure 4.6: *Transmission of thermal neutrons through* ^{nat}*Gd. The different lines correspond to the different thicknesses of Gd. The transmission of 37% corresponds to the n=1 multiple of* a_l *[NCNR2004].*

For the experiment the structure height h_0 of the absorption lines of the source grating is set to h_0 =10 μm. This corresponds to a transmission of 3.3% at $\lambda = 4.1$ Å. In the experiment two source grating wafers are put on top of each other, so that the resulting Gadolinium thickness is 20 μm. This thickness corresponds to a transmission of about 0.001 % and is therefore sufficient.

The height h_2 of the absorption lines of the analyzer grating G_2 was made as high as possible to achieve the best efficiency. The height for the analyzer grating is limited by the fabrication processes as described later in 6.3. Ideally the transmission of the line should be 0. For a Gadolinium thickness of about 6 μm and $\lambda = 4.1$ Å, the transmission is about 14% (see Fig. 4.6). The remaining transmission will affect the visibility and therefore the contrast of the images (see chapter 6).

The structure height h_1 of the grating lines of the beam splitter grating G_1 is calculated such that the lines shift the phase of the incident neutron waves that pass through the grating lines by π. The material is therefore chosen to have as little absorption as possible. As previously mentioned, Silicon has an a_l-length of 50.7 cm. For a Silicon wafer of thickness of 500 μm the transmission is 99.9% in accordance to Eqn. 4.15. In section 2.4 the phase shift of a neutron wave passing through the material

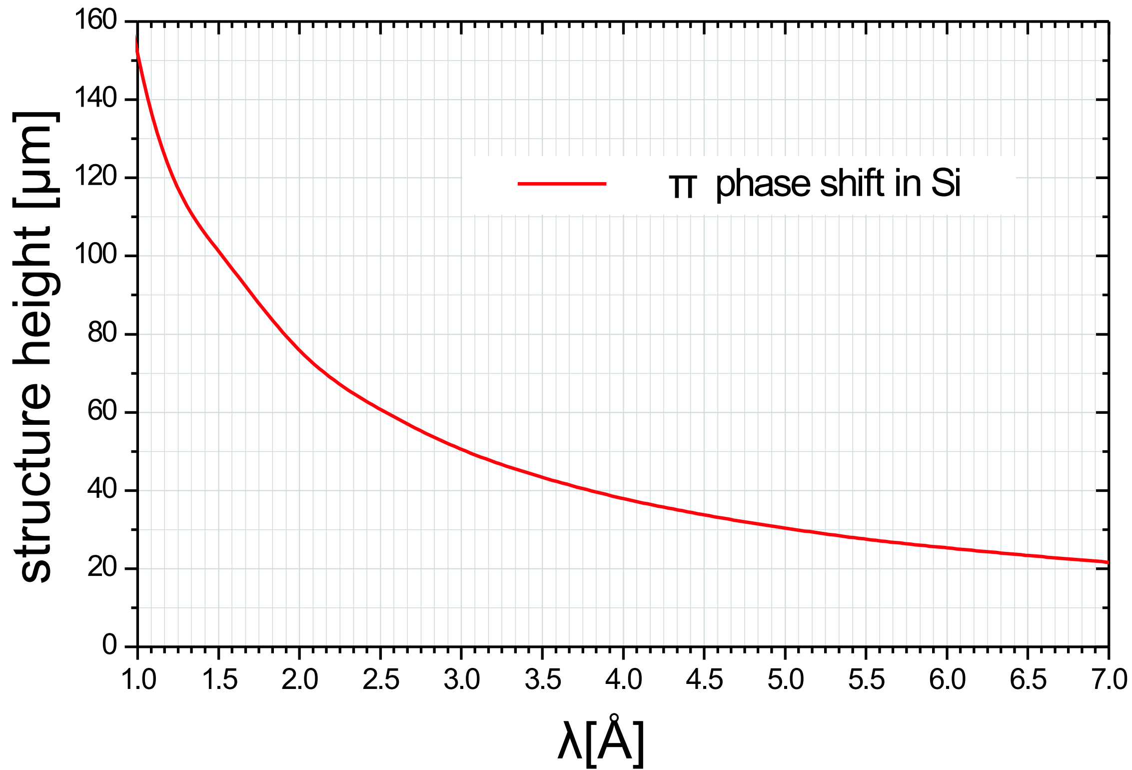

Figure 4.7: *Structure height for π phase shift in Silicon for different wavelengths.*

can be calculated with Eqn. 2.38 to

$$\phi = -N b_c \lambda D \,, \tag{4.16}$$

where D is the thickness of the material. The product of the particle density N and the coherent scattering length b_c is called the neutron scattering length density (nSLD) as already introduced in chapter 2. The nSLD for Silicon for $\lambda = 4.1$ Åis $2.07 \cdot 10^{-6}$Å^{-2}. As mentioned above the phase shift ϕ should be π. This leads to

$$\phi := \pi = \text{nSLD} \cdot \lambda \cdot D = \text{nSLD} \cdot \lambda \cdot h_1 \,. \tag{4.17}$$

The structure height in Silicon for a phase shift of π is therefore

$$h_1 = \frac{\pi}{\text{nSLD} \cdot \lambda} = 37.015 \ \mu m \tag{4.18}$$

Thus h_1 is 37.015 μm. A plot for a phase shift of π in Silicon for different wavelengths is shown in Fig. 4.7. The diagram shows that the smaller the wavelength, the larger the structure height has to be. This was one of the reason to set the wavelength to 4.1 Å. In Tab. 4.1 a summary of the given and calculated parameters is shown.

Parameters		**Value**
Wavelength	λ	4.1 Å (given)
Inter grating distance	l	5.23 m (given)
	$d_{sph.}$	19.4 mm (calculated)
Periods	p_0	1076 μm (calculated)
	p_1	7.97 μm (calculated)
	p_2	4 μm (given)
Structure heigths	h_0	2·10 μm (calculated)
	h_1	37 μm (calculated)
	h_2	6 μm (set due to fabrication)

Table 4.1: *Calculated parameters of the interferometer setup.*

Chapter 5

Grating fabrication

This chapter gives the main part of the thesis, the development of the fabrication processes for the three diffraction gratings. Most parts of the fabrication processes of the gratings were done in the clean room facility[1] *of the Laboratory for Micro- and Nanotechnology (LMN) [LMN] at the PSI. It was a challenge to fabricate the gratings with a size of 64 mm × 64 mm. The goal was to develop a fabrication process for the three gratings with optical photolithography. Another difficulty was that the gratings have to meet different demands in periodicity and materials. The source grating, e.g., has a period of 1076 μm and should be made out of Gd with a structure height of 10 μm, whereas the phase grating has a period of about 8 μm and should be made out of Si with a structure height of 37 μm. Also challenging was the fabrication of the analyzer grating which has a period of 4 μm and should be made out of Gd with a structure height of at least 3 μm. How these three gratings with different demands to material, period and structure heights are fabricated is described in the following sections. In section 5.1 the fabrication of the source grating is explained, containing three different major steps. The fabrication of the phase grating is explained in section 5.2. It contains two different major steps. The fabrication of the analyzer grating is explained in section 5.3 containing three different major steps. The fabrication steps and parameters are listed as run sheets for each grating in the appendix.*

5.1 Source grating G_0

The source grating should consist of an array of absorbing Gd lines with a period of 1076 μm and a structure height of 10 μm. The grating should be fabricated on a non absorbing substrate for neutrons. The fabrication process can be classified into three fabrication steps. The first step is a sputtering process explained in subsection 5.1.1. During this process a multi-layer system Cr/Gd/Cr is sputtered on a 100 mm Quartz wafer. The first Cr layer serves to improve the adhesion of the Gd layer. This is the layer which later contains the absorbing lines. The top Cr layer acts as an etching mask for the Gd layer. The second step is the optical photo lithography process. During this

[1] The nanotechnology clean room facility at the LMN is a 170 m^2 clean area (hybrid class 10/1000), professionally designed and equipped state of the art clean room lab.

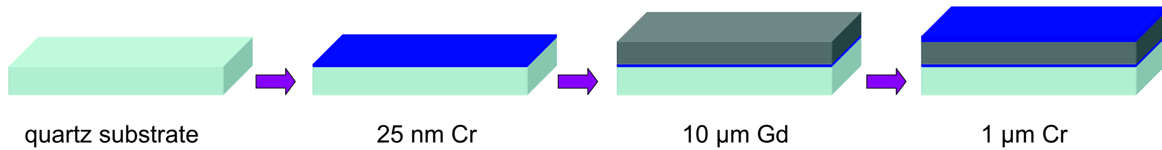

Figure 5.1: *Sputtered layer progression on the Quartz substrate as basis for the source grating. A 25 nm Cr undercoating layer, the Gd layer with a thickness of 10 μm and a 1 μm Cr masking layer.*

process the pattern consisting of grid lines is transferred into a photoresist layer which was spinned on the Cr mask layer, as described in subsection 5.1.2. The third and last step contains two different etching processes. The first one is dry plasma etching. It serves to transfer the photoresist pattern into the Cr mask. The second one is chemical wet etching. It serves to transfer the grating structure into the Gd layer through the patterned Cr mask to obtain the final Gd grating. These etching steps are explained in subsection 5.1.3.

5.1.1 Sputtering process

In the sputtering process Argon ions from a plasma are accelerated towards a target consisting of the material to be deposited (Cr/Gd). The material is sputtered from the target and deposited on the substrate (Fig. 5.2 d). The process is realized in a closed recipient, which is pumped down to a base pressure of $4 \cdot 10^{-6}$ mbar before the deposition starts [Cha1980].

During the sputtering process the three layers are sputtered in succession on top of each other onto the substrate. This is a four inch quartz wafer[1] (SiO_2) with a thickness of 500 μm. Quartz has an a_l - length of 93.3 cm, therefore the absorption of neutrons in the substrate is negligible. The first sputtered layer on the substrate is a 25 nm thick Chromium layer. It serves as an undercoating between the substrate and the second layer. This is the 10 μm thick ^{nat}Gd layer in which later the array of grating lines will be etched. For etching the array of grating lines into the Gd layer an etching mask is needed. This is the last sputtered layer and again a Cr layer with a thickness of 1 μm. The sputtered layer progression is drafted in Fig. 5.1. The layers were produced at the "Von Ardenne - Series LA 440S" machine. The sputter machine and a look inside the recipient on the mounted substrate and the sputter targets is shown in Fig. 5.2 a-c. The machine is a small area circular magnetron sputter source. The diameter of the sputter targets of Cr and Gd is 5 cm. The bias power P and the pressure of the Argon gas p are the adjustable sputter parameters. The bias power was set to 70 W. The applied voltage was 500 V. The Argon pressure was set to 0.2 mbar. With this values the sputter rate for Cr is 75 nm/min, and 150 nm/min for Gd. The next step is the patterning of the Cr mask, as explained in the next subsection.

[1] It has to be Boron free quartz glass since Boron has a high absorption cross section.

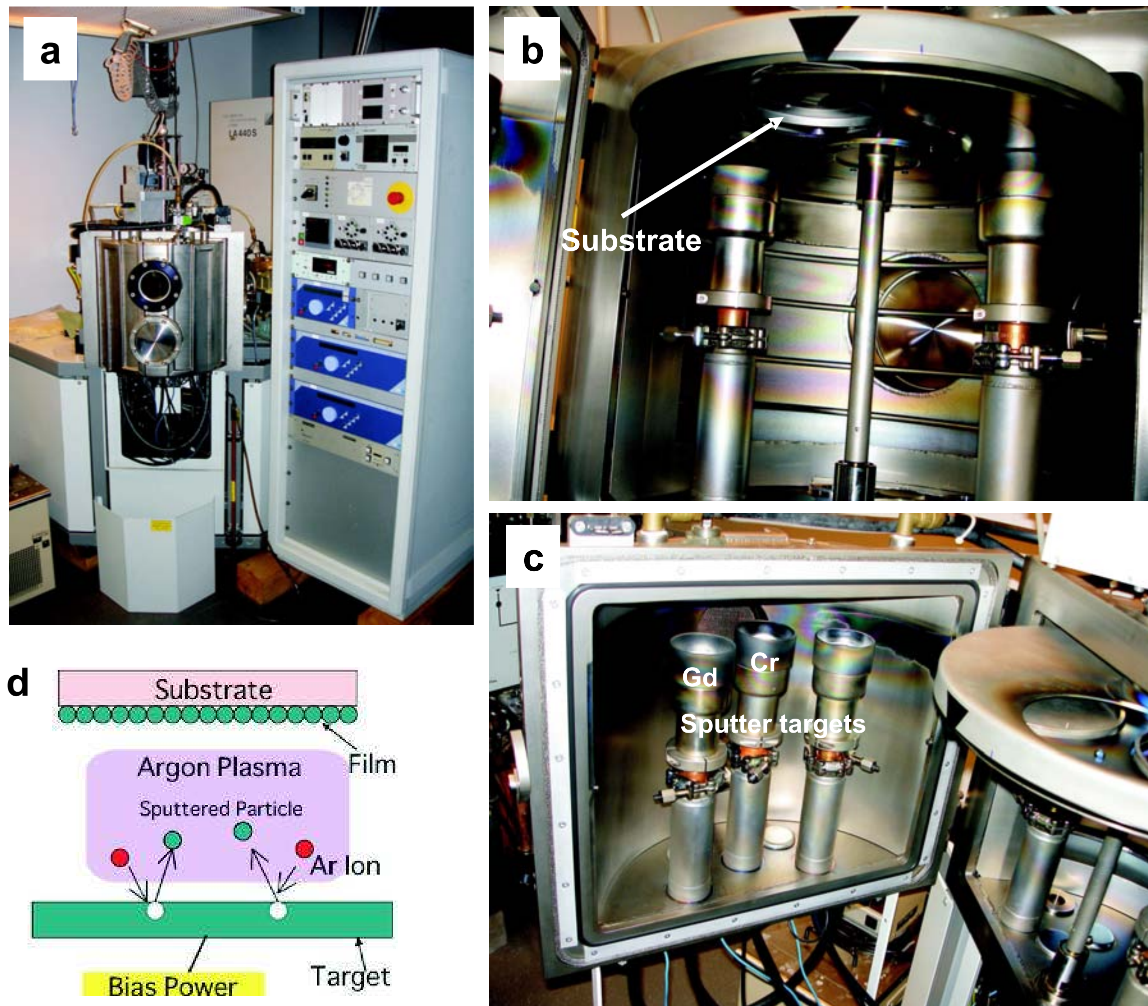

Figure 5.2: *(a) Sputtering machine with recipient and control units. (b) View inside the recipient with a view on the mounted quartz substrate. (c) Cr and Gd sputter targets. (d) Draft of the sputtering process.*

5.1.2 Photo lithography process

The next step is to bring the grating pattern on the sputtered multilayer system. This is done by optical photo lithography [Cha1980]. The steps involved in the photo lithographic process are wafer cleaning, photo resist application, soft baking, exposure with a photo mask, development of the patterned photoresist and hard-baking. Before the photoresist is applied to the Cr masking layer, the surface is cleaned with acetone and isopropanol.

Then the photoresist is applied to the surface using a spin-coating machine. The photoresist used is the positive photoresist S1813 [Shipley]. It was spinned for 30 seconds at 4000 rpm using an acceleration rate of 1000 rpm/sec. The obtained photoresist thickness is 1.3 μm (Fig. 5.4). After the spin coating a soft-bake of the wafer on a hot-plate at 90°C for 90 seconds was made. The exposure step was performed at the Carl Süss MA-6 mask aligner as shown in Fig. 5.3. The photo mask used is a glass mask

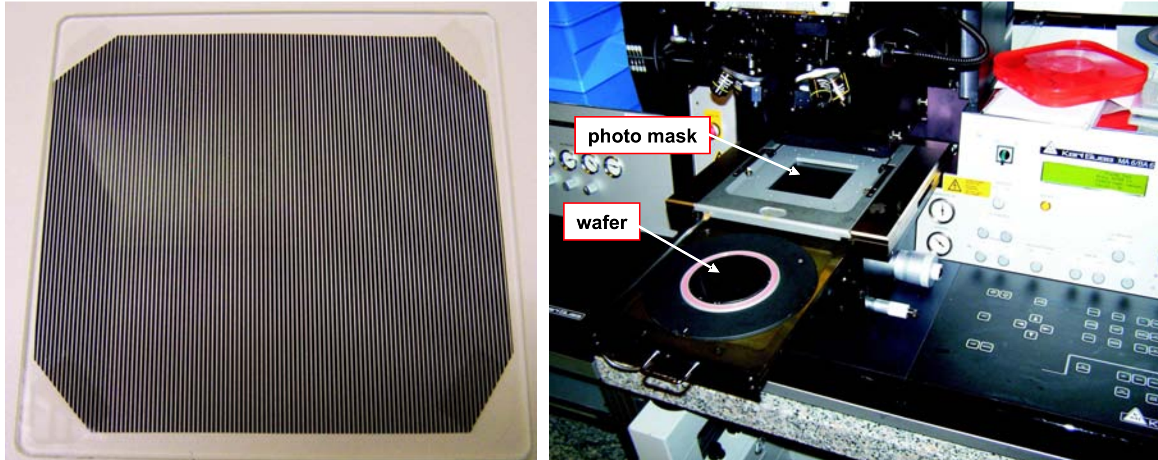

Figure 5.3: *The left picture shows the photo mask with the grid foil glued on the photo mask blank. The right picture shows the mask aligner with the installed photo mask. The wafer is fixed on the vacuum chuck of the drawer.*

blank, where a foil with printed grating lines is glued on as shown in Fig. 5.3. A draft of the masking is shown in Fig. 5.4 . The grating period on the foil is 1120 μm. The exact value as calculated in section 4.1 should be 1076 μm. In chapter 6.1.1 it will be shown, that in the experiment we are able to tilt the source grating about the axis which is parallel to the grating lines. Therefore the grating period is adjustable and for a certain tilt angle α the calculated period of 1076 μm can be achieved. For a DC of 0.4 in the final Gd grating the width of the Gd lines should be 672 μm for $\alpha = 0$. Taking into account the 10 μm under etching during the wet chemical etching process of the Gd layer, the line width on the photo mask is set to 692 μm. The exposure was done with hard contact[1]. The exposure time was 12 seconds. During the exposure process, the photoresist which is not covered by the photo mask undergoes a chemical reaction (Fig. 5.4). The last step in the photolithographic process is the development of the exposed photoresist layer. The photoresist structures which were exposed can be removed with a designated developer solvent. The whole wafer is therefore inserted into the developer solvent for 25 sec. A copy of the photo mask remains as a grating pattern on the Cr mask layer (Fig. 5.4). The next step is to transfer the grating pattern from the photoresist layer into the Cr mask layer as explained in the next subsection.

[1]The photoresist-coated wafer is brought into physical contact with the photo mask. N_2 is used to press the wafer against the photo mask.

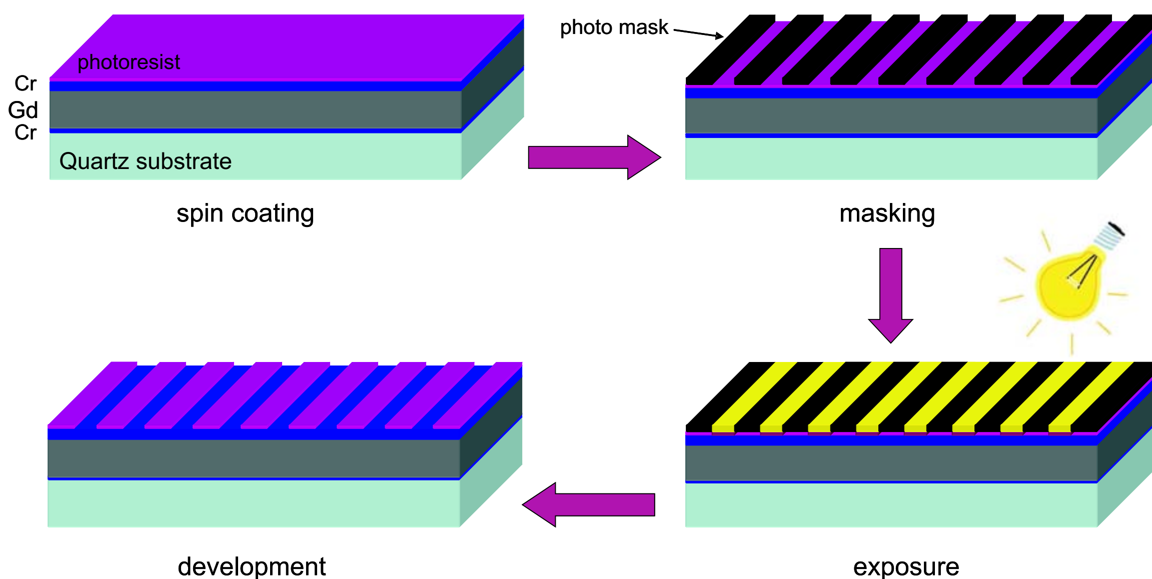

Figure 5.4: *Process steps of the photolithography: Spin coating of the photoresist layer on the sputtered multilayer system. Masking of the photoresist layer with the photo mask consisting of grating lines. Exposure step. Finishing with the development of the exposed photoresist layer. A copy of the photo mask remains in the photoresist layer.*

5.1.3 Etching process

Two etching processes are necessary to achieve the final Gd grating. The first is a plasma etching process. It is used to transfer the photoresist pattern into the Cr layer. The patterned Cr layer later on serves as an etching mask during the pattern transfer into the Gd layer. The second etching process is wet chemical etching. It is used to transfer the grating pattern from the Cr mask layer into the Gd layer, to achieve the final source grating.

Plasma etching: The dry plasma etching process was performed at the BMP machine (vertical mask etcher, BMP Plasmatechnologie GmbH) which is a parallel plate etcher [Cha1980]. The etching with this machine is isotropic[1]. During the process only the Cr which is not covered by the structured photoresist layer is etched away (Fig. 5.5). Chlorine and carbon dioxide are used for the etching process. Before etching the grating pattern into the Gd layer, a hard bake of the remaining photoresist which covers the remaining Cr lines was done. The hard bake was done on a hotplate at 135°C for 3 minutes. This step is necessary in order to harden the photoresist and improve the adhesion of the photoresist to the Cr layer. The hard baked photoresist serves as an additional etching masking in addition to the Cr mask.

Wet chemical etching: The wet chemical etching of the Gd layer can be performed with the structured Cr mask and the additional resist mask. Dilute sulfuric acid is a suitable etching solvent for this system. This was confirmed through several test runs. The ratio of $H_2O : H_2SO_4$ was 100:1. The sulfuric acid was 96% concentrated. For etching the Gd layer, the whole glass wafer was inserted into a Teflon container

[1]Equal etch rate along all directions.

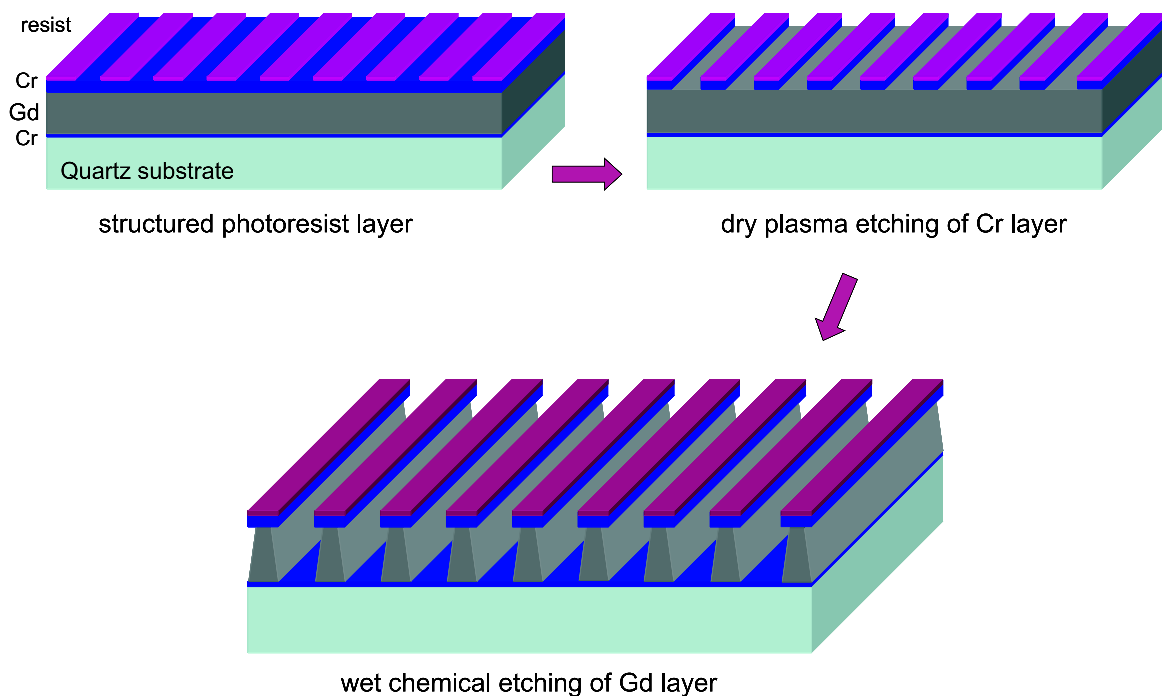

Figure 5.5: *Etching steps: Transferring the grating pattern from the photoresist layer into the Cr mask layer using dry plasma etching. Structuring of the Gd layer through the patterned Cr mask using wet chemical etching. Due to the isotropic wet etching the Gd lines are not vertical.*

which contains the acid. Visual inspections of the wafer showed that the Gd which was not covered by the Cr etching mask dissolves. The sites where the Gd was etched away are clearly visible due to the transparency of the Quartz wafer. The etching time was 5 minutes. Since the wet etching process for the Gd layer is isotropic, the grating walls are not vertical as depicted in Fig. 5.5. The result of the completely processed wafer is shown in Fig. 5.6 . The front view of the wafer is shown in Fig. 5.6 (a). The structured resist layer appears in color. Fig. 5.6 (b) shows the wafer from the backside. The black lines are the Gd grating lines. Fig. 5.6 (c) is a closed-up view from the back side. The grating lines are clearly visible. Fig. 5.6 (d) shows a light microscope photo. It is the top view on the grating. The pink color corresponds to the resist lines. A measurement of the DC with the light microscope performed with an encoder resulted a DC of 0.4, i.e. exactly the desired value. Fig. 5.6 e shows a height profile measurement of the grating. The measured height is 11.75 μm. This is the sum of the 10 μm Gd, 1 μm Cr and the remaining photo resist. The results of the height measurement reflect the demands to the structure heights. The slope of the side walls is also seen in the height measurement.

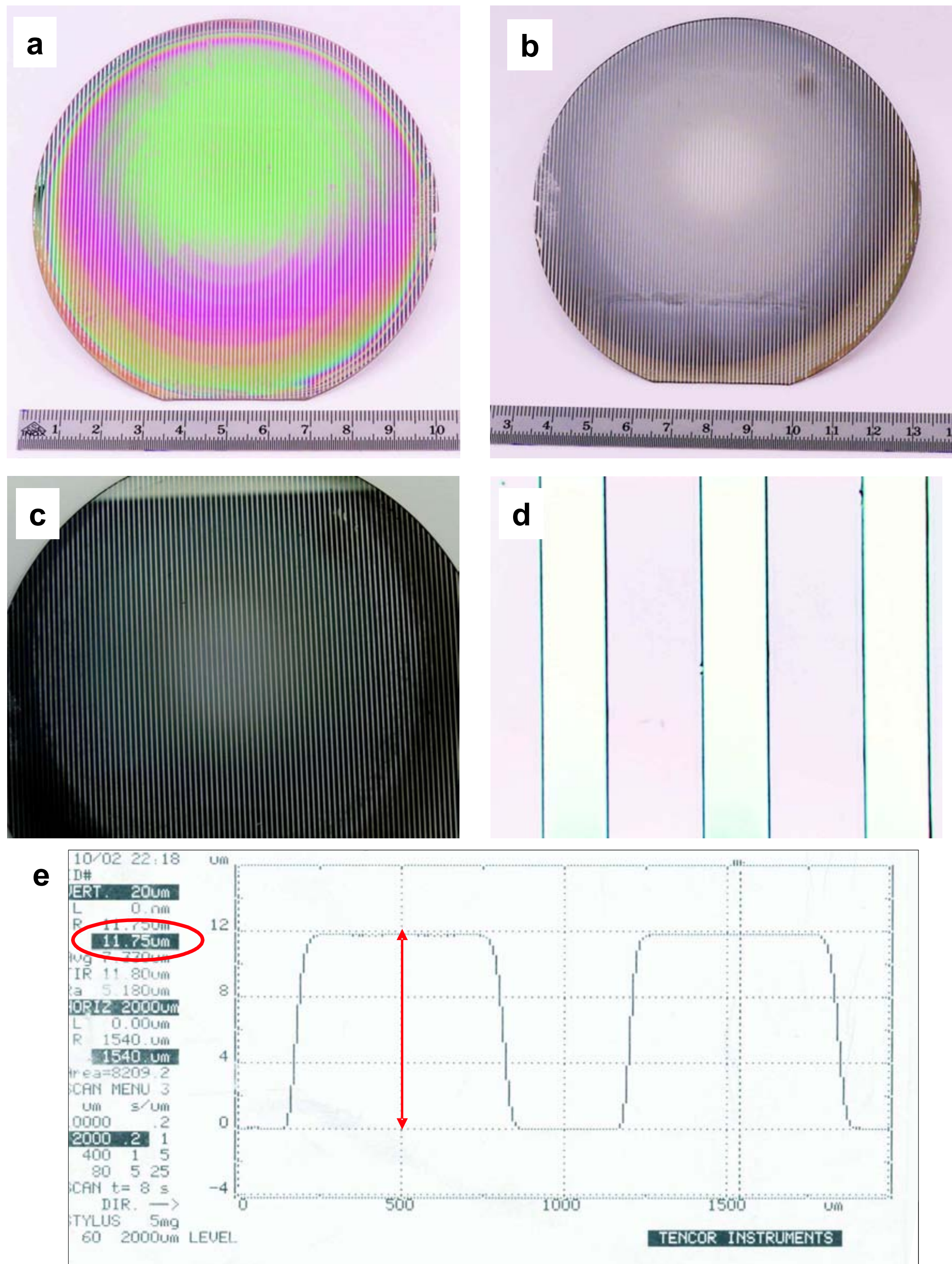

Figure 5.6: *(a) Top view of the processed source grating wafer. The colors stem from the photoresist lines. (b) Back view of the wafer. The black lines are the Gd grating lines. (c) Closer view of the grating lines form the backside. (d) Light microscope photo of the top view of the grating lines. The pink color is caused by the photoresist remaining on the Gd lines. (e) Height profile measurement.*

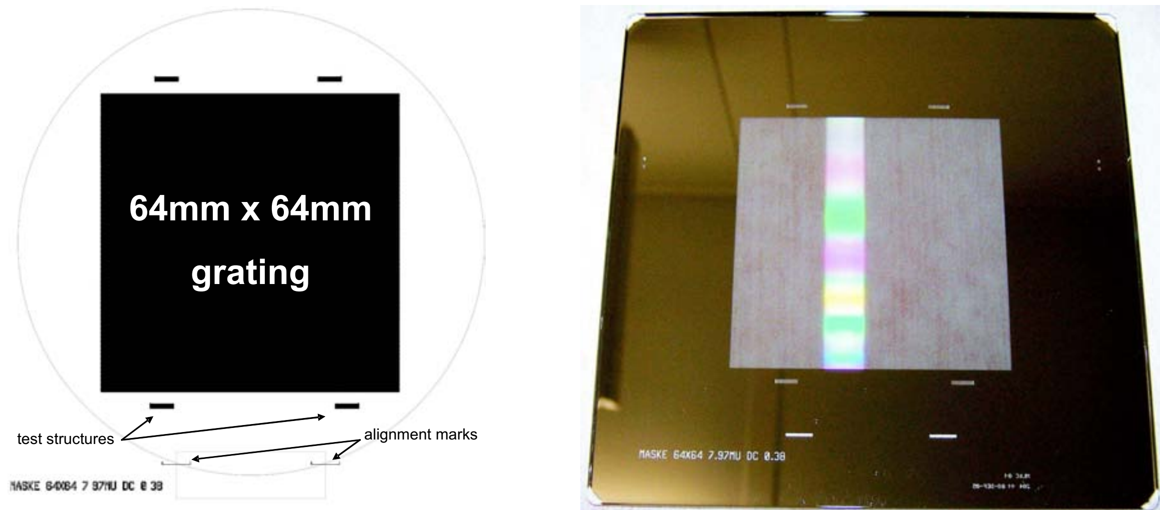

Figure 5.7: *(left) Sketch shows a draft of the photo mask. The circle symbolizes the size of the four inch wafer. The big black square is the grating. (right) Picture of the photo mask with the grating, the test structures and the alignment marks is shown.*

5.2 Phase grating G_1

The phase grating is fabricated on a 100 mm and 280 μm thick Si wafer. Due to the large a_l - length of Si the attenuation of the neutron beam through the wafer is negligible and the assumption of a pure phase grating is justified. The period of the grating has to be 7.97 μm and the structure height has to be 37 μm to achieve π phase shift. The phase grating is fabricated on a [110] oriented[1] Si wafer. The wafer surface was thermally oxidized to give a 110 nm thick SiO_2 layer. The oxide layer later serves as an etching mask for the Si. The fabrication of this grating consists of two parts. The first one is photo lithography to superimpose the grating structure on the oxide layer of the wafer described in section 5.2.1. The second process contains two etching steps, a dry plasma etching process to transfer the photoresist pattern into the oxide masking layer followed by a wet chemical etching process. The latter is used to etch the Si to obtain the final grating structure. Both etching steps are described in section 5.2.2.

5.2.1 Photo lithography process

A photoresist layer was spin coated on the oxide layer. Positive photoresist S1805 [Shipley] was used. It was spin coated with 4000 rpm and an acceleration of 1000 rpm/sec for 30 seconds. The obtained photoresist thickness is 500 nm (Fig. 5.8). A soft bake with the wafer on the hotplate at 90° for 30 seconds was made after the spin coating. The exposure step was performed at the Carl Süss MA-6 mask aligner. The photo mask which was used for the exposure was especially designed for a grating with a size of 64 mm × 64 mm and a period of 7.97 μm and a DC of 0.5. To fabricate

[1] [110] have $\{1\bar{1}1\}$ planes which are orientated perpendicular to the (110) surface (see Fig. 5.9).

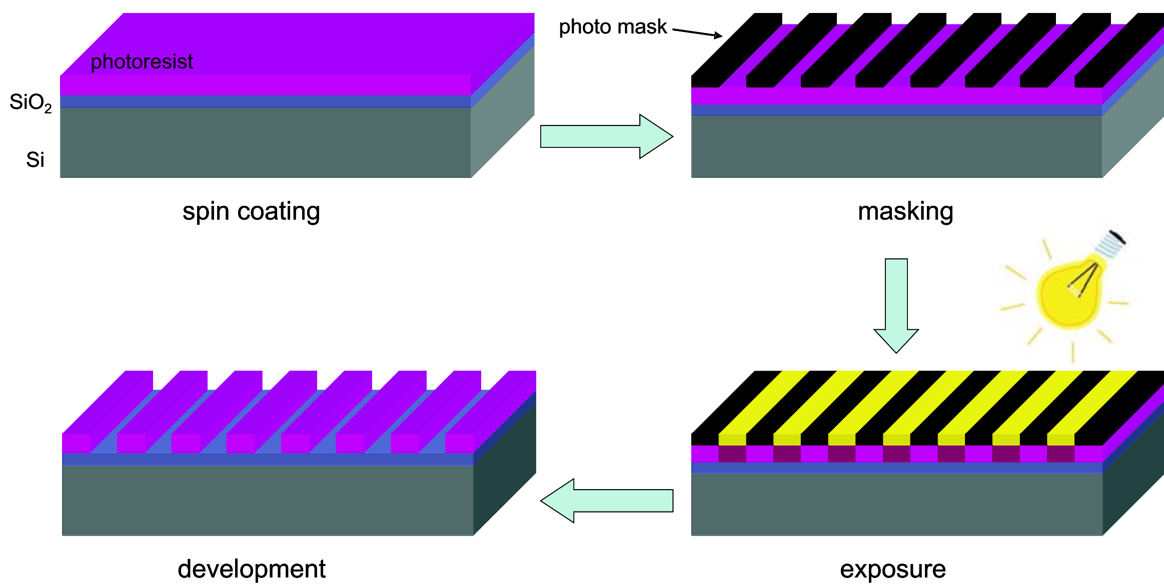

Figure 5.8: *Process steps of the photolithography: Spin coating of the photoresist layer on the sputtered multilayer system. Masking of the photoresist layer with the photo mask, consisting of grid lines. Followed by the exposure step. Finishing with the development of the exposed photoresist layer.*

a Si grating with a duty cycle of 0.5 and a structure height of 37 μm means for the photo mask design that one has to take into account the under etching of the side walls during the wet chemical etching process of the 37 μm deep silicon trenches. The etch selectivity for a Si(110) wafer is 40:1 for the {110} planes compared to the {111} planes [Ehr2002]. This means that one has to design the duty cycle on the photo mask to DC=0.38. For effective etching, the grating lines must be aligned parallel to the primary flat of the wafer. The alignment procedure was done with marks on the photo mask. A picture of the photo mask is shown in Fig. 5.7. In addition to the grating on the photo mask, small grating test structures with the same period and DC were designed. They serve later for cross section images taken with a scanning electron microscope (SEM).

The exposure was performed with vacuum contact[1]. The exposure time was set to 4 seconds. The exposed wafer was developed for 25 seconds in a designated developer solvent. The steps of the photolithography process are illustrated in Fig. 5.8. The next step is to transfer the pattern from the photo resist layer into the oxide mask.

5.2.2 Etching process

Two etching steps are necessary to obtain the final Si grating. The first one is a plasma etching process. It transfers the photoresist structures into the oxide layer. The second one is the wet chemical etching to transfers the pattern from the oxide layer into the Si wafer.

[1] The photoresist-coated wafer is brought into physical contact with the photo mask. Additional a vacuum is drawn between the mask and wafer (highest resolution mode).

Plasma etching: The dry plasma etching process is a reactive ion etching process (RIE) [Cha1980]. This etching step is anisotropic[1]. The etching step was performed at the Oxford Plasmalab 100 reaktive ion etcher. The etch gases for the process are CHF_3 and O_2. After the RIE process, the remaining photoresist was removed with an oxygen plasma etching step (see Fig. 5.9) in the Tepla 300 plasma processor machine.

Wet chemical etching: Before inserting the wafer into the etching bath to etch the grating pattern from the oxide mask into the Si wafer, a dip with the whole wafer into buffered oxide etch[2] (BOE) was done. The BOE etches away possible residual oxide. The used etching solvent for etching the (110) Si is a KOH[3] bath. The KOH etching rate strongly depends on the crystallographic orientation of the Si. It is therefore an anisotropic etching process. The (110) planes etche faster in comparison to the $(1\bar{1}1)$ planes [Ehr2002]. This makes it possible to etch gratings with almost vertical $\{1\bar{1}1\}$ sidewalls as shown in Fig. 5.9. The etching rate is 1.4 μm/min for a KOH concentration of 10% and a bath temperature of 70°C. The {110} planes are etched 40 times faster then the $(1\bar{1}1)$ planes. This leads to an under etching of 925nm for the 37 μm deep trenches. With the etch rate of the KOH bath the etching time was 26.5 minutes. The grating structure is now transferred into the Si wafer. The last step to obtain the final Si grating is to remove the remaining SiO_2 on the Si bars. It is etched away with BOE for a period of 3 minutes (Fig. 5.9). To check the processed wafer for the ideal duty cycle and etch depth, the test structures are separated from the large grating by cleaving. By cleaving the test structures once again perpendicular to the grating lines one can obtain cross section images recorded with a scanning electron microscopy (SEM). With the cross section image one can verify the fabrication process and analyze the results for the etching depth and DC. The results of the fabricated phase grating are shown in Fig. 5.10. The left picture is a photo of a processed wafer, which was used during the experiment. It shows the grating and the four test structures. The right picture shows a cross section SEM image of a test structure. The SEM image is taken with a Zeiss Supra 55 VP microscope. The measured height in the SEM image is 37.14 μm. The duty cycle of the grating as measured in the cross section image is 0.5. The measured period is 7.97 μm. Within the accuracy of the SEM measurement the obtained results are in tune with the demands to the structure height, the period and the duty cycle. However, the cross section SEM image does not stem from the wafer on the left side, but from another wafer which was produced in the same way. The difference is that the wafer on the left picture was processed with a 110 nm oxide layer, whereas the cross section picture stems from a wafer which was processed with a 60 nm thick oxide layer. The risk for getting the cross sectional SEM image by cleaving the test structures from the wafer is considerably high. A top view look already indicates the DC of 0.5. The KOH etching time was the same for both wafers, and therefore no big deviations from the etching depth are expected. Thus the bars of the grating are tapering off at the surface due to the fact that, the oxide layer of 60 nm was too thin for the etching depth. Thus the oxide layer was gone before the etching depth of 37 μm was achieved. With a oxide layer of 110 nm this problem was solved.

[1] Different etching rates for different directions.
[2] Etching solution containing mainly hydrofluoric acid and distilled water in ratio 1:7 and
[3] Etching solution containing distilled water and potassium hydroxide, KOH, in ratio 9:1.

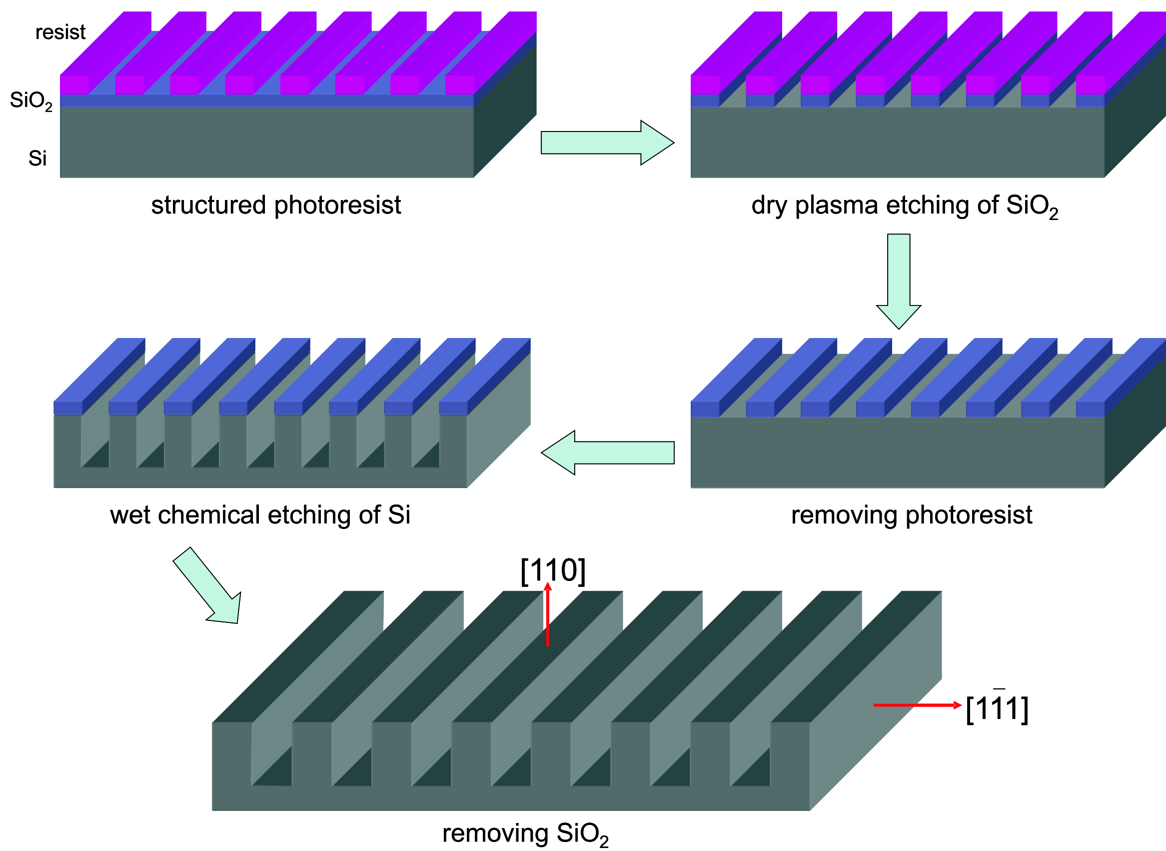

Figure 5.9: *Etching steps: Transfer of the photoresist pattern into the SiO_2 layer using plasma etching. Removal of the photoresist pattern with oxygen plasma etching. Wet chemical etching of the* [110] *orientated Si wafer, and removal of the oxide mask. Due to the anisotropic etching vertical sidewalls* $\{1\bar{1}1\}$ *are obtained.*

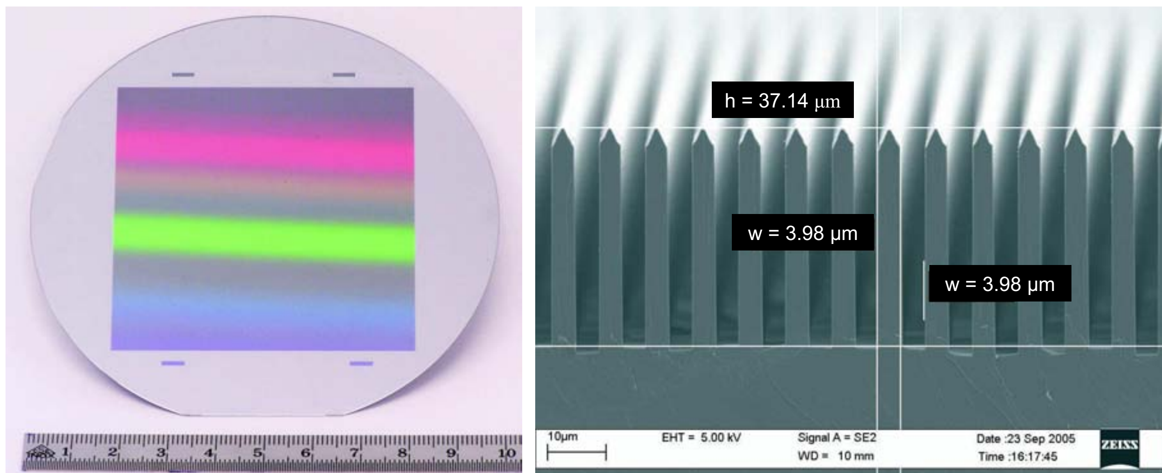

Figure 5.10: *The left picture shows the processed wafer. The colored square is the grating. Around the grating the four test structures are visible. The right picture is a SEM image of a cross section corresponding to one of the test structures.*

5.3 Analyzer grating G_2

The analyzer grating is an absorption grating with a period of 4 μm consisting of Gd absorber lines. The substrate for the analyzer grating is a 280 μm thick 100 mm Si wafer. The starting point for the analyzer grating is a Si grating with a size of 64 mm $\times$ 64 mm and fill the trenches with Gd. Due to the large a_l - length of Si the attenuation trough the 280 μm thick wafer is negligible and the neutrons then only "see" the superimposed Gd inside the Si grating.

The Si grating was fabricated in the same way as the phase grating in section 5.2 with a depth 6 μm. The width of the Si bars is 1.21 μm. This corresponds to a DC in the Si grating of 0.7. The challenge for the analyzer grating was how to fabricate absorbing lines made of Gd. The primary idea was to fill the trenches of the Si grating with Gd. This filling was realized by an evaporation process. In the next subsection we will see that this strategy is linked with a lot of obstacles and a lot of process steps, since one has to remove the evaporated Gd from the grating bars. Otherwise the absorption of the neutrons is the same over the whole grating.

However, from the idea to fill the trenches of the Si grating, a second possibility arises to fabricate absorbing Gd lines. This idea is to build "towers" on the top of the Si bars. This is realized by evaporating Gd sideways on the Si bars. The advantage of this strategy is that only one step has to be performed to obtain the final analyzer grating.

5.3.1 Evaporation process

The first idea, to fill the trenches of the Si grating with Gd, was realized by perpendicular evaporating Gd into the trenches. Therefore the Si wafer with the grating was placed exactly over the evaporation boat. The problem which emerges with this strategy is, that one has to remove after the evaporation process the evaporated Gd on the bars of the grating. It was considered to etch away the Gd on the bars, without removing the Gd inside the trenches. This was tried by covering the evaporated Gd inside the trenches with a photoresist layer. This layer is temporary stable against the etching solvent of Gd (diluted sulfuric acid see 5.1.3). A SEM cross section image of the evaporated Gd on the grating and the covering with photoresist is shown in Fig. 5.11. The next step after the spin coating of the covering photoresist layer is to bare the Gd on the top of the bars. This is realized by etching away the thin photoresist layer with an oxide plasma. When the Gd is finally bared, it is etched away with diluted sulphuric acid, hoping that the photoresist layer which covers the Gd in the trenches is hermetical sealed. Several test runs showed that it is not a reliable way to remove the Gd on the bars, because the Gd inside the trenches in most cases was also etched away. However, from the idea to fill the trenches with Gd a second possibility arises to fabricate the analyzer grating. We know now that the evaporated Gd grows with an apex angle off $2\alpha = 32^\circ$ on the bars of the Si grating (Fig. 5.11). With this knowledge of the growth angle, the other possibility to fabricate the grating is an inclined evaporation process of Gd. By evaporating Gd onto the side walls of the Si bars under an angle, which is the same angle α than the half of the apex angle , it is possible to grow towers

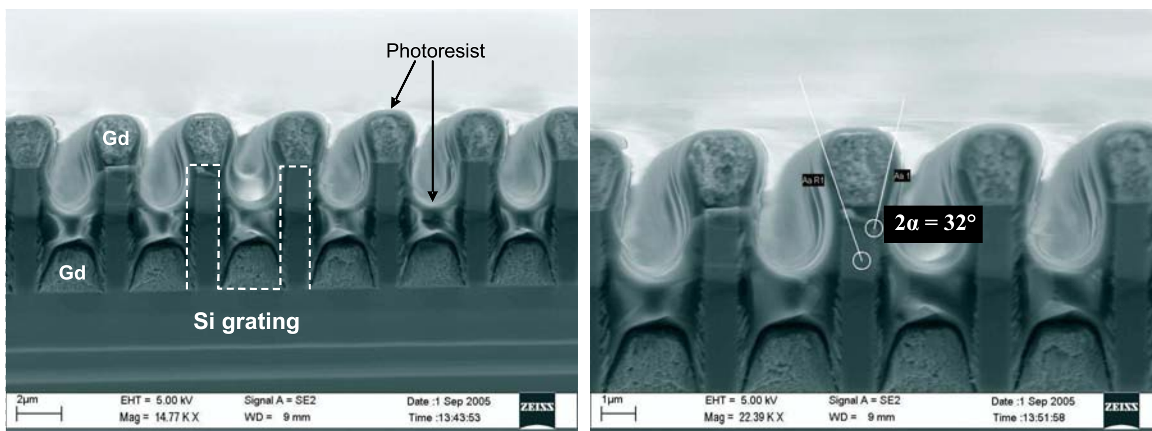

Figure 5.11: *Si grating with evaporated Gd in the trenches and on the bars. A spin coated photoresist layer covers the Gd. The Gd grows as a cone with an apex angel* $2\alpha = 32°$ *on the bars.*

on the bars with an height h and a width w as indicated in Fig. 5.12. In addition to the thusly grown towers, the Gd which adhere at the side walls also contributes to the structure height of the absorbing Gd lines. In practice the sidewall evaporation is done by displacing the wafer by a distance x away from the plumb on the crucible as shown in Fig. 5.13. The distance x is chosen that the angle between the center of the grating and the plumb is the same as α. The only parameter which is adjustable during the evaporation process is the height h. The height of the evaporated Gd is measured *in-situ* with an balance quartz (shown in Fig. 5.13) during the evaporation process. Due to the fact that the Gd grows with the half apex angle α, the Gd height h affects directly the thickness t of Gd at the sidewalls and therefore the DC of the analyzer grating. The thickness t is calculated by

$$t = h \cdot tan\, \alpha\,. \tag{5.1}$$

The spacing d which determines the DC of the grating is given by

$$d = p_2 - s - t \,=\, p_2 - s - (h \cdot tan\, \alpha) \tag{5.2}$$

where p_2 is the period of the Si grating and s is the width of the Si bars. s is determined from a top view of a SEM image of the etched Si grating (Fig. 5.14 b). Finally the DC of the analyzer grating is given by

$$DC = \frac{d}{p_2} = \frac{p_2 - s - t}{p_2} = \frac{p_2 - s - (h \cdot tan\, \alpha)}{p_2}\,. \tag{5.3}$$

For a Si grating with the period p_2, the bar width s and the given apex angle α, the only parameter which can influence the DC is the evaporated Gd height h as shown in Eqn. 5.3.

The evaporation process was performed using a Balzers BAE 250 thermal evaporator. The process was realized in a closed chamber which was pumped down to a

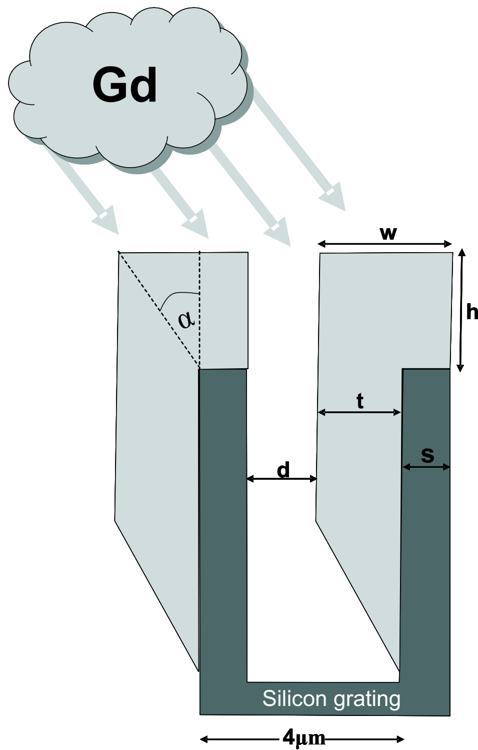

Figure 5.12: *Schematical picture of the inclined evaporation of Gd on the side walls of the Si bars.*

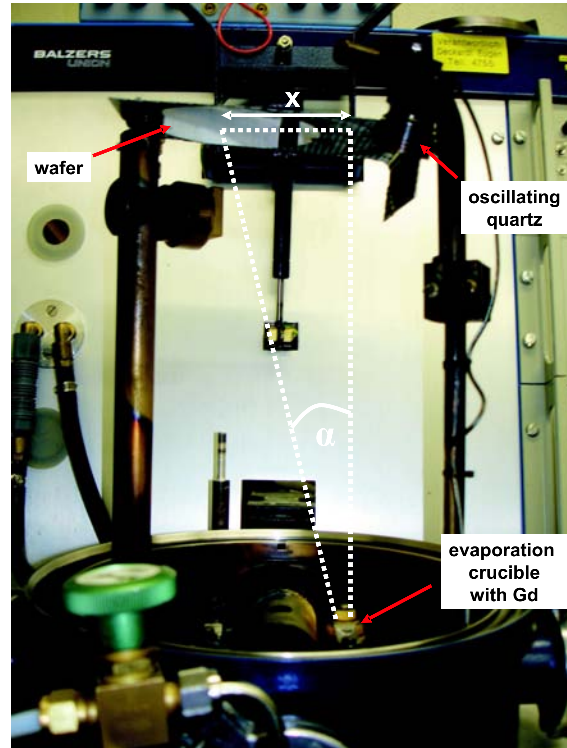

Figure 5.13: *Realization of the inclined evaporation at the evaporation machine.*

pressure of about 10^{-6} mbar. The evaporation rate of Gd measured *in-situ* with the balance quartz was set to 1 nm/sec. Several test runs showed that the evaporated Gd thickness indicated with the balance quartz differ form the effective Gd thickness measured with a SEM inspection. In average the deviation of the evaporated Gd thickness indicated by the oscillating quartz is in the range of 30-40% more than measured by a SEM inspection. Therefore it is not easy to evaporate the exact Gd height h to achieve a DC of 0.5 for a given bar width s. The compromise was made to evaporate a little bit more Gd and therefore get a better absorption but a DC less the 0.5[1].

The resulting analyzer grating is shown in Fig. 5.14. Image (a) shows the processed wafer. The colored square is the grating. Above the grating the two test structures are visible. The test structures below the grating are cleaved away. They serve for the cross section SEM image. Image (b) shows a top view SEM image of the etched Si grating. The bar width is s =1.21 μm. Image (c) shows a cross section SEM image of one of the test structures after the evaporating process. The "towers" on the Si bars and the additional Gd on the side walls are clearly visible. Image (d) shows the measured cross section SEM image. From the given bar width s and the evaporated

[1] The influence of the DC of the analyzer grating is the influence on the data analysis after a phase stepping scan. Since the extracting of the Fourier components is nevertheless possible the restriction on the DC is not so strong. However best performance is achieved for a DC of 0.5.

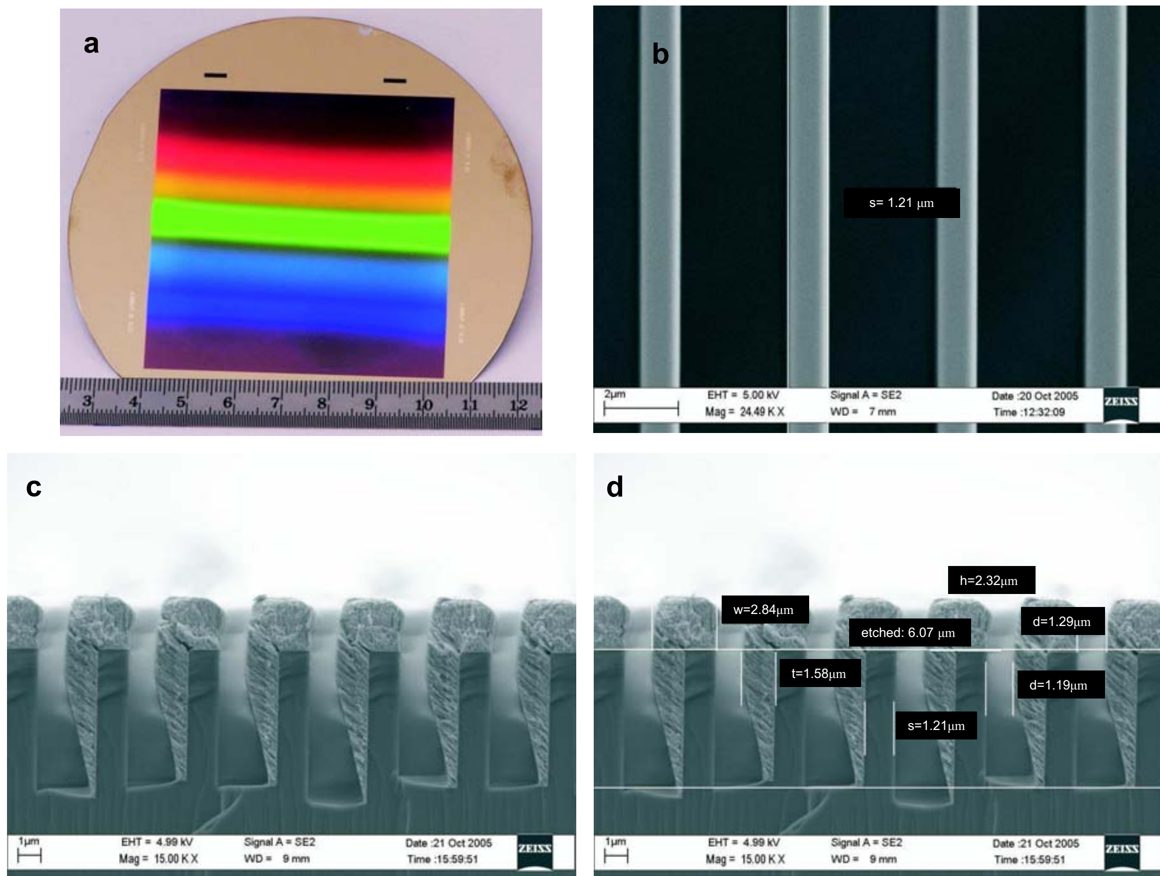

Figure 5.14: *(a) Image of the processed wafer. The colored square is the grating. (b) SEM top view image on the etched Si grating. The gray lines are the bars of the grating. (c) SEM cross section image with the evaporated Gd on the top of the bars and on the side walls. (d) Measured parameters of the evaporating process.*

Gd thickness h =2.32 μm, the measured values for t, d, w are determined. These are shown together with the calculated values in Tab. 5.1.

We found that, the smaller the bar width s is, the larger the height h can be for the same DC. Therefore the size of the "towers" $(w \cdot h)$ on the Si bars depends on the width s. For smaller bar width, the Gd on the sidewalls with the width t, which contributes as addition to the absorption height, could then be larger.

The analyzer grating can be well fabricated by side wall evaporating of Gd. Due to the uncertainty in the thickness measurement of evaporated Gd with the balance quartz, it is hard to get exact height required for a DC of 0.5. The question arises why one did not fabricate a Si grating with smaller s. It was not possible due to the fact that the possibility to fabricate the analyzer grating by the side wall evaporation technique was discoverd too late. Therefore the time was too short to design and order a new photo mask to fabricate a Si grating with small s in time with the scheduled beam time.

	nominal (calculated)	actual (measured)
t $[\mu m]$	1.43	1.58
d $[\mu m]$	1.37	1.29
w $[\mu m]$	2.74	2.84
DC	0.31	0.3

Table 5.1: *Comparison between the nominal (calculated) and the actual (measured) parameters for Si bar width s =1.21 μm and evaporated Gd thickness h =2.32 μm.*

Chapter 6

Experimental setup and results

In this chapter the realization of the experimental setup at the ICON beam line and the obtained results are shown. Section 6.1 describes the installation of the interferometer components at the beam line. The first challenge of the installation of the setup was the implementation of the source grating. It is important to mount the source grating as close as possible to the beam exit port, to still be able to perform the phase stepping with it, to change its period and to be able to change the DC of the source grating. How all this is mechanically realized is shown and explained in 6.1.1 . The second challenge for the setup was how to bring the remaining components ,i.e. the phase grating, the analyzer grating the object and the detector as close as possible together due to the demanded small distances between them. This is done by including all these components together in a interferometer box as shown in 6.1.2 . The testing of the performance of the three gratings and the obtained results are described in 6.2 .

6.1 Experimental setup at the ICON beam line

The experiment was performed at the ICON beam line at the spallation neutron source SINQ at the Paul Scherrer Institut. The neutron flux density at the beam line is $5.8 \times 10^6\ cm^{-2} \cdot s^{-1}$ with an aperture of 2 cm (used during the experiment) [ICON]. In Fig. 6.1 the installed components of the setup at the beam line are shown. Inset (a) in Fig. 6.1 shows the source grating mount[1]. It is installed as close as possible to the beam exit port. The red plate in inset (a) is the neutron fast shutter. The mount of the source grating and its functions are explained in more detail in subsection 6.1.1. Inset (b) in Fig. 6.1 shows the velocity selector installed at the beam line. The exit window of the velocity selector has a size of 4 cm × 4 cm. Inset (c) in Fig. 6.1 shows the interferometer box. It is installed at the first experimental place of the beam line. The interferometer box includes the remaining components like the phase grating, the analyzer grating, the object and the CCD camera. The assembling of these components is in detail described in subsection 6.1.2.

[1] The source grating mount consists of two source grating wafers. When we speak in the following context from the source grating then we mean the combination of these to wafers as the source grating.

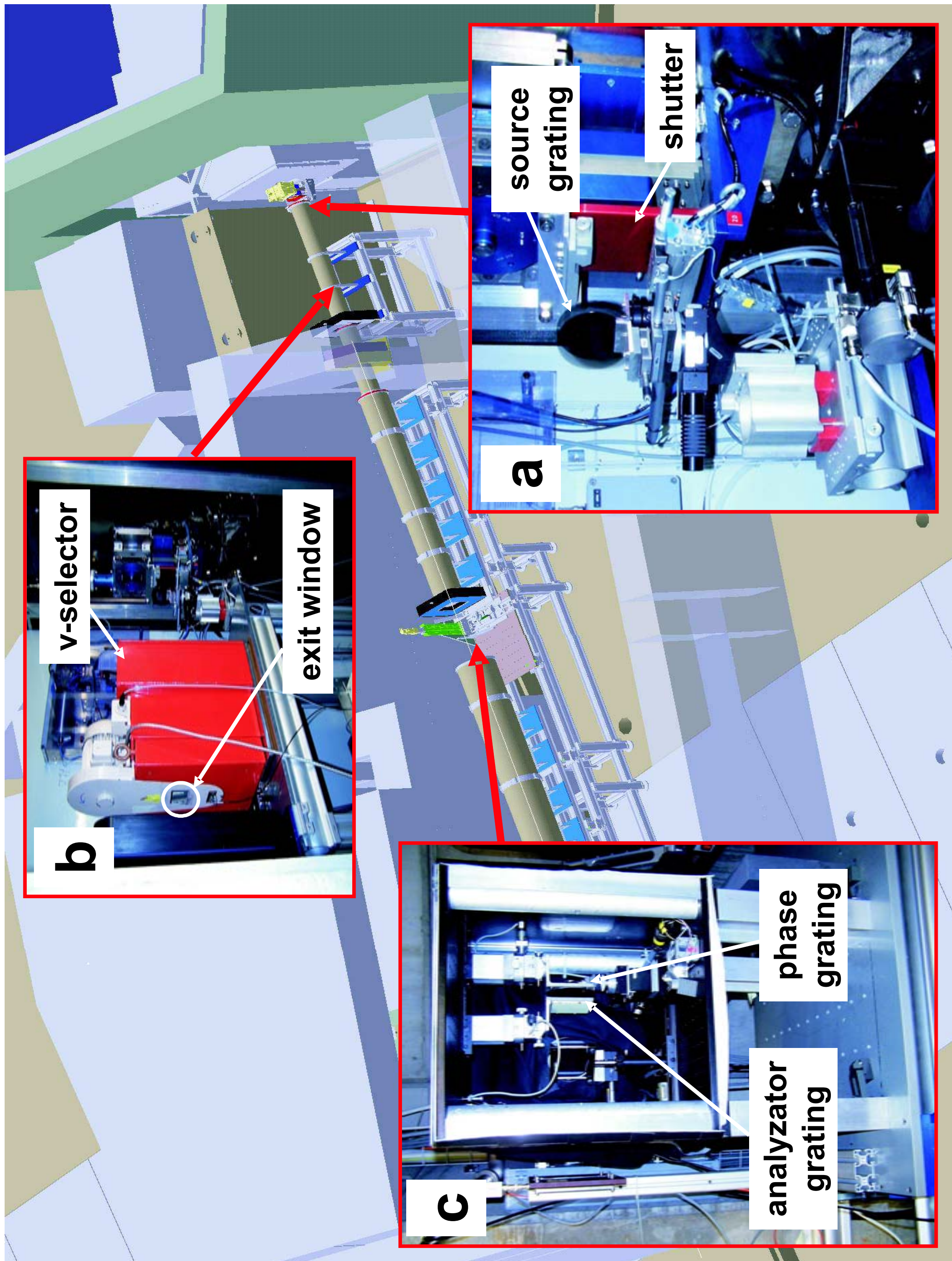

Figure 6.1: *Setup of the interferometer components at the ICON beam line. (a) Installation of the source grating mount close to the beam exit port. (b) Installation of the velocity selector. (c) Installation of the interferometer box at the first experimental place. The draft of the beam line is the 3D version of Fig. 4.1 which was used to calculate the setup parameters [ICON].*

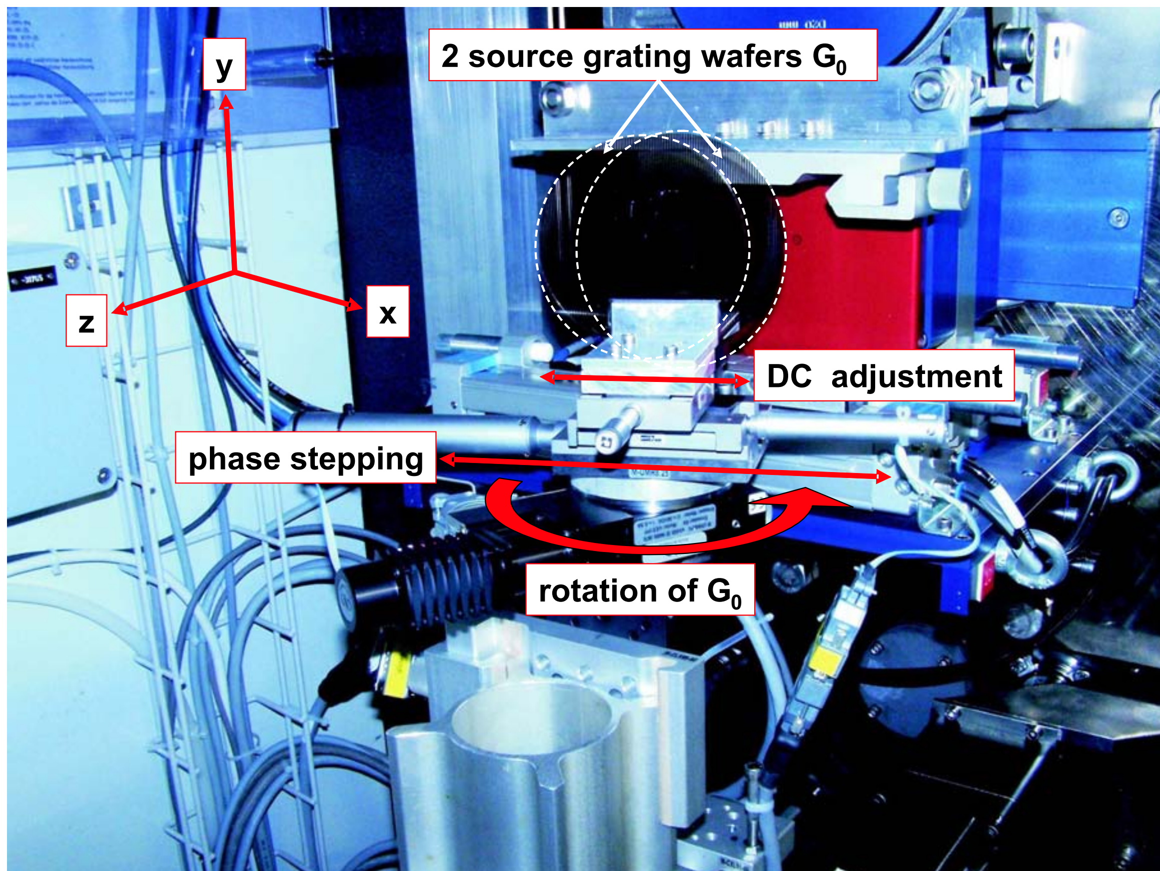

Figure 6.2: *Source grating mount consisting of two source grating wafers. With two motorized linear stages one can adjust the DC of the source grating and perform the phase-stepping. With the motorized rotation of the source grating mount the period can be adjusted.*

6.1.1 Source grating mount

A picture of the source grating mount is shown in Fig. 6.2. The two wafers are both glued with the back side of the wafer on an aluminum bracket. The grating lines of both wafers are oriented parallel to the y-axis. The rear bracket with the glued grating on is mounted on a prism stage[1], better seen on inset (a) of Fig. 6.1. The front bracket is mounted on a linear translation stage. With the movement of this stage (in the direction along the surface normal of the wafer) and the 3D adjustment possibility of the prism stage both wafers are brought into plan parallel contact to each other. After the plane parallel adjustment of the gratings, one of the tilt axis of the prism stage serves to adjust the grating lines of both gratings parallel with respect to each other without Moiré fringes[2]. Due to the transparency of both quartz wafers and the relatively large period this adjustment can be done manually by eye. One of the wafers

[1]3D adjustment with two tilting axes and one rotation axis.

[2] A Moiré pattern or fringe is an interference effect created for example when two grids are overlaid at an angle. The comparatively fine structure of the gratings seem to have regular thicker lines superimposed.

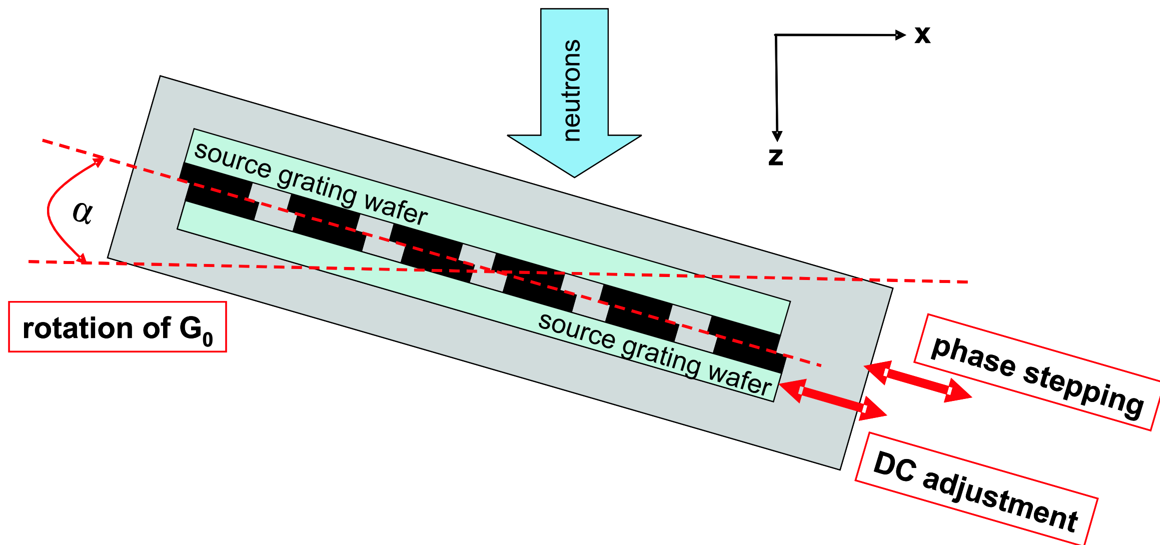

Figure 6.3: *Draft of the top view of the source grating mount. Adjustment of the DC with the moveable source grating wafers. The other source grating wafer is fixed. The phase-stepping is performed with a linear stage on which both wafers are mounted. The adjustment of the period of G_0 can be done by rotating the whole source grating mount by an angle α.*

is mounted on a motorized linear stage along the x-axis (perpendicular to the grating lines and to the surface normal). This movement serves to adjust the DC of the source grating as indicated in Fig. 6.3. By setting the DC and therefore the spacing s of the slits, one can influence the transverse coherence of each individual grating slit (section 3.4). Both wafers are mounted together on a second motorized linear translation stage. With this is the stage the phase-stepping as explained in section 3.3 is performed. The linear stage for the phase-stepping is finally mounted on a rotary stage as indicated in Fig. 6.3. This rotation around the y-axis is also motorized. With the rotation of the whole source grating mount around the y-axis one can adjust the period of the source grating within a few percent. This gives some freedom for the adjustment of the period to the setup as described in subsection 3.2.1. As described in section 5.1.2 the period of the fabricated source grating is 1120 μm. The calculated optimum period (section 4.1) is 1076 μm. This period can be achieved by rotating the source grating mount by an angle of 16° to the optical axis as shown in Fig. 6.3. For an angle of 16° and a DC of 0.4 the maximum spacing of the transmitting slits is s=430 μm. With this spacing enough transverse coherence is ensured as demanded in section 3.4.

6.1.2 Interferometer box

The interferometer box and the components inside are shown in Fig. 6.4. The box was build from two bread boards. One serves as a base plate and the other as cover plate. The components are mounted on optical rails mounted on the bread boards. Fig. 6.4 (a) shows a side view into the box (neutrons coming from the right side). It shows the object, which is mounted on a goniometer. The goniometer itself is mounted on a height

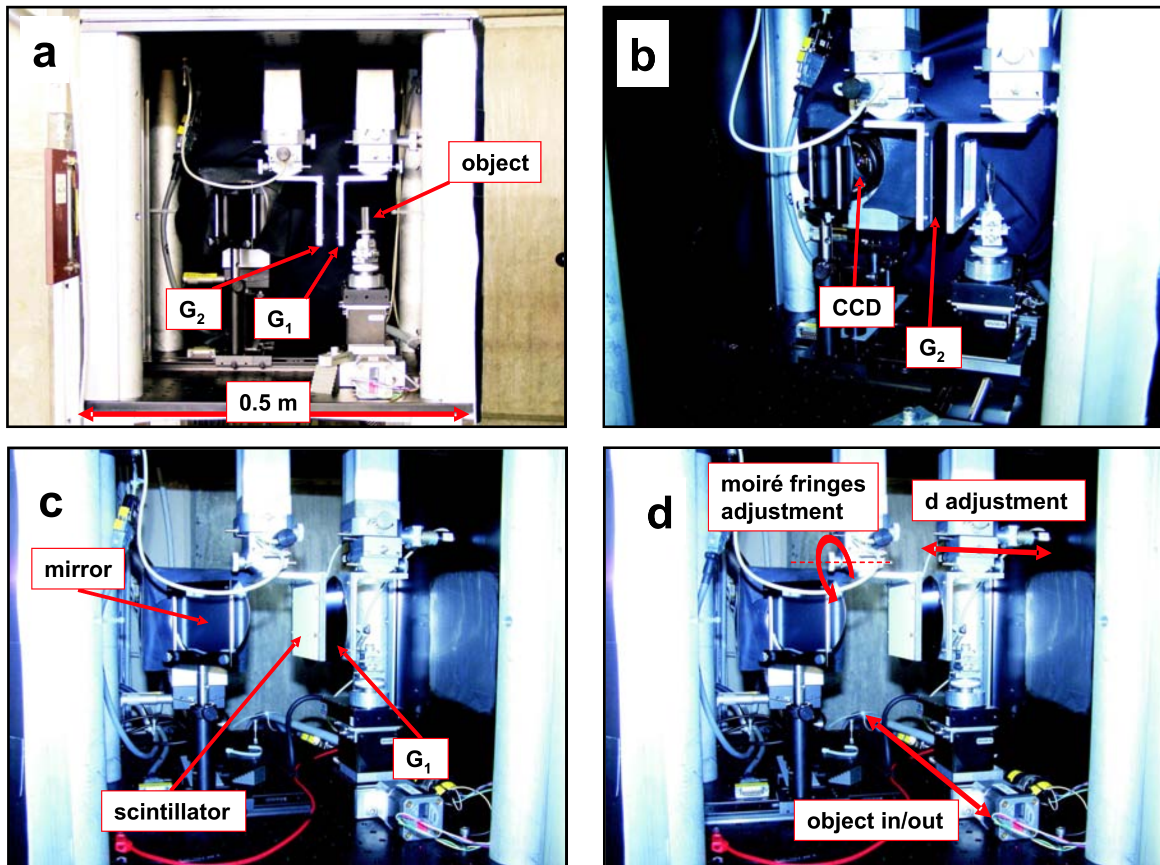

Figure 6.4: *Pictures of the interior of the interferometer box. (a) View on the object and the two brackets on which G_1 and G_2 are mounted. The edge length of the box is 0.5 m. (b) View on mounted G_2 and objective of the CCD camera. (c) View on mounted G_1 and the scintillator screen mounted on the backside of the same bracket where G_2 is mounted. View on the installed mirror. (d) Motorized adjustments of the Talbot distance d and the Moiré fringes. Motorized translation stage for the in/out positioning of the object.*

adjustable block to adjust the object to the beam center. The block then is mounted on a motorized translation stage. With this stage the object can be driven to the in and out position related to the beam as shown in Fig. 6.4 (d). This is required to take the flat field image[1] for the data processing. The wafer with the phase grating (seen in Fig. 6.4 (c)) and the wafer with the analyzer grating (seen in Fig. 6.4 (b)) are mounted on brackets. The brackets have cutouts with the same size as the gratings. The wafers are mounted such that the lines are vertical just like the grating lines of the source grating. The brackets themselves are mounted on goniometers. Both wafers are aligned parallel[2] to each other with the goniometers. The motorized adjustment for the Talbot distance along the beam can be done at the goniometer on which the phase grating

[1]Image without the object in the beam.

[2] The adjustment for each grating was done with a laser. The reflected zeroth diffraction order from the grating was adjusted to the beam center.

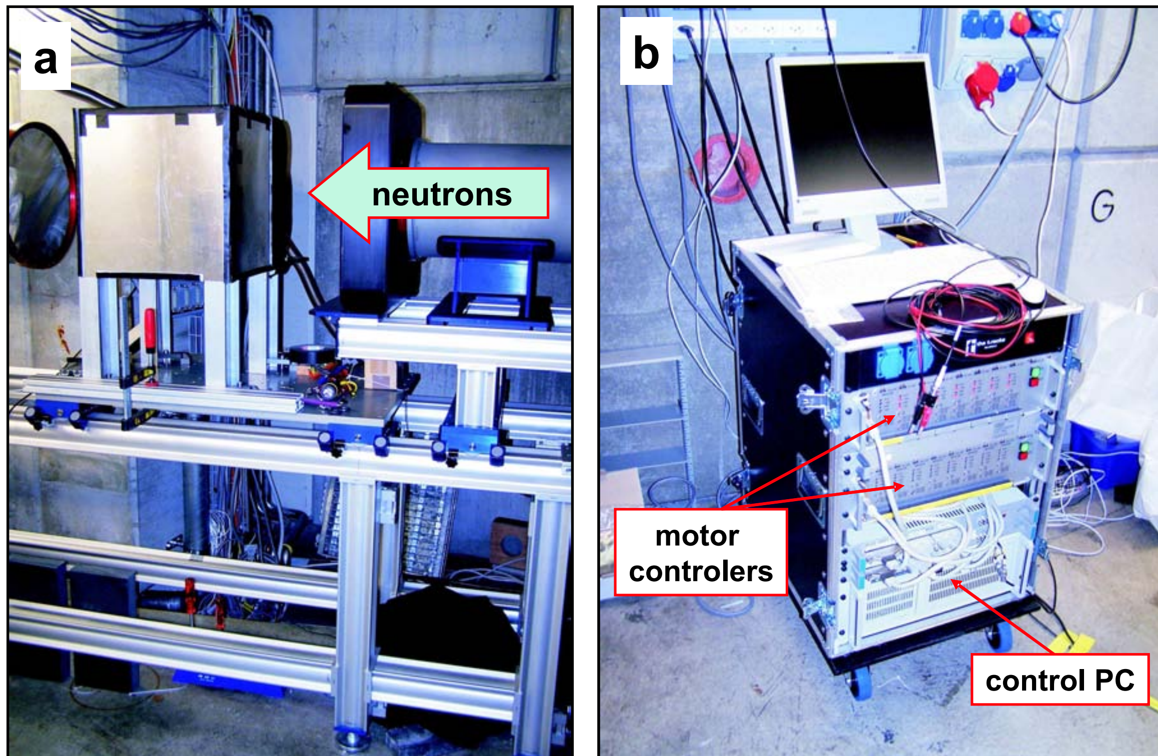

Figure 6.5: *(a) Interferometer box with the aluminum plate shielding to shield the inside from light. The box is mounted on four H-profiles which serves to adjust the box at the beam height. (b) Mobile rack which includes the control PC and the motor controllers. The rack is placed inside the hutch during the experiment .*

is mounted (see Fig. 6.4 (d)). The other goniometer on which the analyzer grating is mounted the motorized Moiré fringe adjustment between G_1 and G_2 around the beam axis can be done. Due to the fact, that it is not possible to directly detect neutron images with the CCD camera, one has to convert the neutrons into visible light. This is done with a scintillator screen[1]. The scintillator screen is directly mounted behind the analyzer grating on the rear side of the bracket as shown in Fig. 6.4 (c). The created visible light is deflected via a mirror (Fig. 6.4 (c)) towards the CCD camera[2] shown in Fig. 6.4 (b). The four end walls of the box were covered with 2 mm thin aluminum plates which shields the interior of the interferometer box of light from outside as shown in Fig. 6.5 (a). The shielding of the front side where the neutrons travel through did not attenuate the beam, due to the fact that the a_l - length for aluminum is 31.1 cm. In addition the inside of the aluminum plates were lacquered in black to avoid reflection of light created from the scintillator screen only. At the entrance window of the aluminum plate where the neutrons pass through the lacquer was removed to avoid the scattering of the neutrons. All the motorized stages and goniometers of the setup are connected to the motor controllers. These controllers are integrated into a mobile rack (Fig. 6.5 (b)). The controllers are linked to a PC via interfaces. The CCD

[1]This is a 300 μm thick ^{6}Li/ZnS converter with a fluorescence screen.
[2]Only the objective of the camera is seen. The camera itself is shielded with lead from γ-rays.

camera is also directly connected to the PC in the rack. The stepper motors were driven by in-house developed motor drivers (SLS 2003L SMD) and directly controlled by the well established software Spec (http://www.certif.com). The CCD camera was integrated in this stable and at the same time flexible software as well. Procedures like the phase stepping scans were automated by self written Spec macros. The rack is placed during the experiment inside the hutch of the beam line. During the experiment the connection to this PC was made by a direct network connection from another PC which was located outside the hutch. To ensure a stable operation, both PCs were running the Linux operating system.

6.2 Experimental results

The first step is to verify if our calculations for the grating parameters and the setup parameters calculated in chapter 4 were correct. This means that we should be able to observe Moiré fringes. The result is given in 6.2.1 where fringe visibility is measured and then optimized. Measurements on metal rods having the same dimensions and composition as the ones shown in the simulation in Fig. 3.8 are shown in 6.2.2.

6.2.1 Optimization of the visibility

The interferometric visibility or "fringe visibility" quantifies the contrast of an interference pattern. In our case we define the visibility as: $((I_{max} - I_{dark}) - (I_{min} - I_{dark}))/(I_{max} - I_{dark})$. I_{dark} is the measured dark field and corresponds to the offset of the ADC (analogue-digital converter) of the CCD camera. Therefore the visibility is normalized to unity, and is given in percent of the maxima amplitude oscillation. An determination example of the visibility of an interference pattern is shown in Fig. 6.6. For our purpose the visibility is sufficient as long as the contrast variation is large enough to provide an intensity oscillation after a phase stepping scan. An improvement of the visibility increases the quality of the phase images in term of noise reduction.

First we are checking the visibility for the setup parameters we calculated in chapter 4. Single images are taken with the CCD camera. The images were recorded using a 300 μm thick scintillator with a demagnifying optical lens system and a cooled CCD camera. The effective spatial resolution of 250 μm was mainly determined by the intrinsic unsharpness of the scintillator. The exposure time for a single image was 10 seconds. The size of the recorded images is 60mm $\times$ 60mm[1].

[1] The recorded field of view with the CCD camera is smaller than the grating size (64mm$\times$ 64mm) due to the demagnifying optic (done with a photo objective) to the CCD camera which has a 1 inch $\times$1 inch chip.

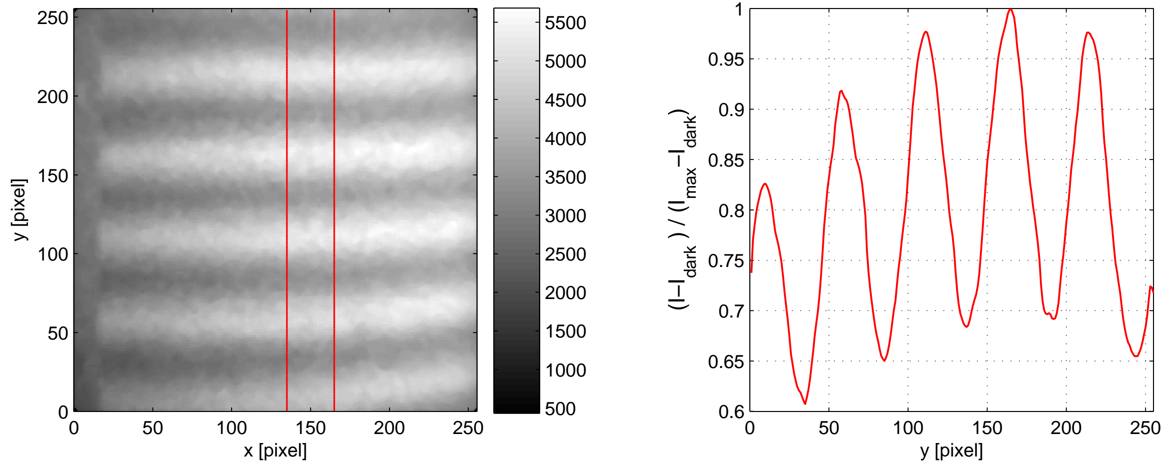

Figure 6.6: *Image recorded with the CCD camera (left). Due to the misalignment of the grating lines of G_1 and G_2 Moiré fringes are apparent. They serve to analyze the fringe visibility shown on the section plot on the right side. Here the visibility is 31%.*

If a single image is taken and the grating lines of the phase grating and the analyzer grating are not aligned parallel to each other, one will observe Moiré fringes[1] as shown in Fig. 6.6 on the left side. This misalignment and the resulting Moiré fringes can be used to check the performance of the setup and the gratings by analyzing the visibility. Taking a section profile (averaging over a band around a pixel value for x with a certain width) along the y pixel axis, gives the fringe visibility as shown in Fig. 6.6 on the right side.

The next step was to verify if the calculated parameters are the optimal ones. This was done changing parameters like the inter-grating distance d, the period of the source grating p_0 and the width s of the source grating. For the first check of the visibility we start with the calculated parameters of the setup: $l = 5.23$ m, $p_0 = 1076$ μ ($\alpha = 16°$), $s = 108$ μm, $d = 19.4$ mm. The visibility for these parameters is determined to 14%. Now we check if we are able to optimize the visibility by changing one parameter after the other and therefore find an optimum for the visibility [2].

1) Optimization of the visibility by changing the inter-grating distance d:
To find out the best visibility we first change the distance along the beam axis around the calculated value. The other parameters stay fixed. A plot of the obtained visibility against the distance is shown in Fig. 6.7. The best visibility is 31 % obtained at $d = 20.7$ mm. Already for $d = 18.7$ μm and $d = 24.2$ μm the visibility is zero. Therefore we set the inter-grating distance from now on to $d = 20.7$ mm.

2) Optimization of the visibility by changing the period p_0:

[1] The periodicity of the Moiré fringes is by a factor of $1/\sin\theta$ larger as the interference fringes behind G_1. θ is the rotation angle between the grating lines of G_1 and G_2 around the beam axis.

[2] Changing one parameter after the other is a simplification for the optimization of the visibility. One has to take into account that the parameters are not independent from each other. Therefore if one is changing one parameter normally the other parameters have to be readjusted.

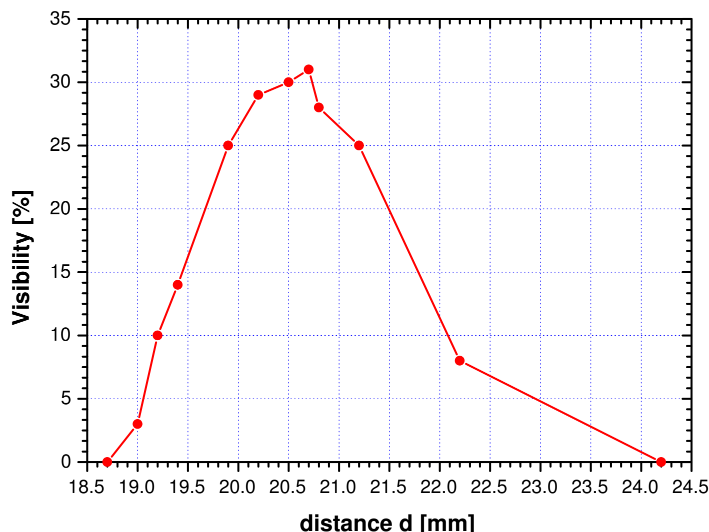

Figure 6.7: *Optimization of the visibility by changing the inter-grating distance d. The maximum of the visibility is 31% at d=20.7 mm.*

The next step is the checking of the visibility as a function of p_0. Therefore the visibility is analyzed for different rotating angles α of the source grating. The result is shown in Fig. 6.8. The best visibility of 33 % is obtained for $\alpha = 19°$ which corresponds to a period of $p_0 = 1058$ μm. Therefore we set the period of p_0 to $p_0 = 1058$ μm.

3) Optimization of the visibility by changing the slit width s respectively the DC of G_0:
Now we measure the visibility as a function of the slit width s of a single line source of the source grating. The changing of s is equivalent to changing the DC of the source grating. Therefore the DC adjustment is stepped over one period of p_0. At the beginning both gratings are placed in such a way that $s = 0$. For changing s we are measuring on the one hand the visibility and on the other hand the the flux of neutrons. The counting rate (flux) is measured in form of counts registered[1] with the CCD camera. Both curves are plotted together in Fig. 6.9. From the plot one sees that for $s = 0$ the counting rate is zero. That means that the transmission through the absorbing lines of G_0 is zero. The counting rate reaches a maximum for the DC adjustment of 0.5 mm. This is the point where the grating lines of the two source gratings are congruent and the DC has its maximum of 0.4. This corresponds to a slit width of $s = 423$ μm . Further stepping decrease the counting rate due to the fact that the slit with goes again to zero. The visibility has a constant value in the region of $0.2 \leq s \leq 0.9$. The smaller s the higher the transverse coherence length. This should result in an improvement of the visibility for smaller s. From the results of this measurement we set s =423 μm where the flux has its maximum and the visibility is 32 %.

[1] The dark field counts are already subtracted.

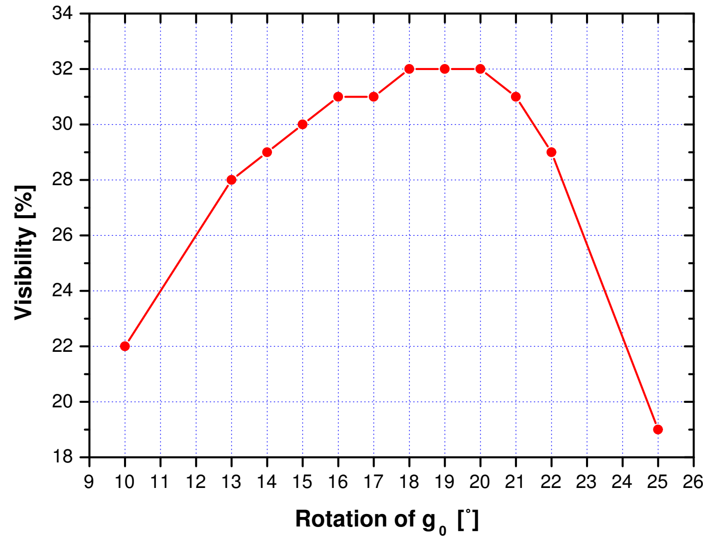

Figure 6.8: *Optimization of the visibility by changing the period of the source grating realized by rotating the source grating mount. The maximum of the visibility is 33 % at* $\alpha = 19°$ *which corresponds to* $p_0 = 1054\mu m$.

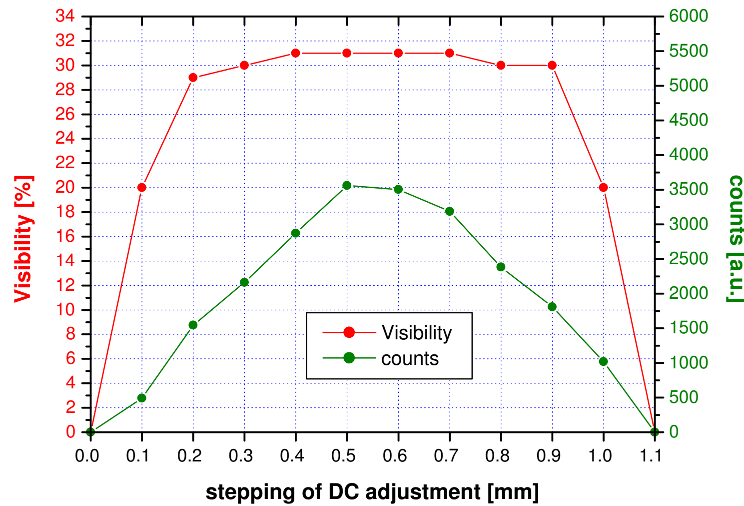

Figure 6.9: *Optimization of the visibility by changing the slit width s respectively the DC of the source grating. In addition the neutron flux is measured in form of counts registered with the CCD. For DC adjustment of 0.5 mm (s= 423 µm) the flux has its maximum but the visibility has a small decrease due to the fact that the changing of s also chances the transverse coherence length.*

Optimized parameters for the best visibility and maximum flux are:

$$\begin{aligned} d &= 20.7\ mm \\ p_0 &= 1058\ \mu m\ \ (\alpha = 19^\circ) \\ s &= 423\ \mu m\ \ (\text{DC adjustment } 0.5\ mm,\ \text{DC} = 0.4)\,. \end{aligned}$$

The achieved value of 32 % for the visibility is sufficient to perform phase stepping scans with objects to obtain phase images. The visibility could not be furthermore enhanced, since the wavelength distribution around the design wavelength was the limiting factor. The impact of the wavelength distribution is that it smears out the interference pattern in the first Talbot plane and therefore decreases the visibility.

For the measurement with an object the phase grating and the analyzer grating are adjusted in the way that the grating lines are parallel and therefore no Moiré fringes are apparent.

6.2.2 Phase contrast radiography images

The objects used for the experiment were the same as used for the simulation. These were four metal (Ti, Pb, Mg, Mo) rods with a quadratic profile. The edge length of the rods is 5 mm. The rods were fixed on a thin plate which was mounted on the holder of the goniometer. Fig. 6.10 shows the results of the neutron images. To obtain these three pictures the phase stepping approach was used as explained in section 3.3. Ten images were taken per oscillation period in the phase stepping scan. The exposure time for a single raw image was 10 seconds. Fig. 6.10 (a) shows the processed transmission image. Due to the different attenuation coefficients of the materials differences in the transmitted intensity are observed. Fig. 6.10 (d) shows a section profile through the corresponding image data. Furthermore, it is not easy to distinguish materials with roughly same attenuation coefficients like Pb and Mg in the transmission image. Fig. 6.10 (b) shows the processed phase gradient image. Since the vector component of the phase gradient in the direction perpendicular to the grating lines is constant, but off opposite signs for both sides of the rods, they appear dark and bright. Due to the fact that Ti has a negative coherent scattering length the refractive index is greater the unity. Therefore both sides of the Ti rod have opposite colors than the other rods. Fig. 6.10 (e) shows a section profile through the corresponding image data. The exact values from the simulation for $d\Phi/dx$ are: $\pm$ 51 (Ti), $\mp$ 81 (Pb), $\mp$ 116 (Mo) and $\mp$ 61 (Mg) [π/mm]. In the case of Ti and Pb, this agrees well with our measurements. The slightly smaller measured values for Mo and Mg could be caused by the presence of impurities in the metal objects, decreasing the effective scattering length density. Particularly, for weakly absorbing materials like Pb and Mg the integrated phase shift signal (Figs. 6.10 (c),(f)) yield a higher contrast in the image. It is interesting to note that Ti has a negative coherent scattering length and consequently a positive phase shift. Therefore the Ti rod appears dark instead of bright as the other rods in the object phase shift image in Fig. 6.10 c. The exact values from the simulation results for the

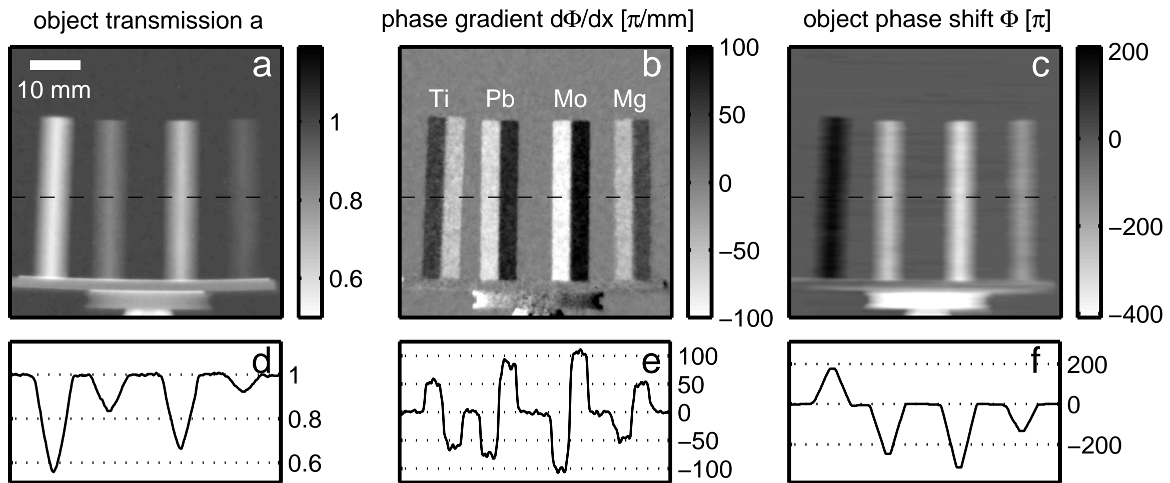

Figure 6.10: *Linear contour plots and section profiles of processed data for a test object comprising a Titanium (Ti), Lead (Pb), Molybdenum (Mo), and Magnesium (Mg) metal rod with a quadratic profile. (a) Conventional neutron transmission image. (b) Differential phase contrast image $d\Phi/dx$. (c) Integrated phase shift $\Phi(x, y)$ retrieved from $d\Phi/dx$ by integration. The images are represented on a linear grey scale. (d,e,f) Section profiles through the corresponding image data [Pfe2006b].*

maximum object phase shifts ϕ are: 180 (Ti), -286 (Pb), -400 (Mo) and -213 (Mg) [π]. These results demonstrate clearly that the grating interferometer based quantitative phase contrast imaging is feasible with neutrons. Particularly the high efficiency (short exposure times) of the DPC technique present a major step forward in neutron phase radiography.

Chapter 7

Conclusion and Outlook

We showed that our grating based neutron interferometer can yield both quantitative differential phase contrast (DPC) images and phase shift images of objects. These images are simultaneously obtained and complementary to the conventional attenuation image. This technique requires little spatial and temporal coherence, thus the method is significantly more efficient than existing techniques. An exposure time of 12 h for a single phase image measured at an equivalent neutron source (National Institute of Standards) is reported in [McM2003]. We conclude that our method, which requires typically 10 images of 10 sec exposure time for a single image, yields a decrease in exposure times by more than a factor of hundred.

The results show also that the requirements on the three gratings can be realized with the developed fabrication processes, especially the fabrication of the source and the phase grating. The result of the fabrication process of the analyzer grating was sufficient for the experiment but still can be improved. The experimental results are in good agreement with the performed simulations.

Due to the fact that all the results were obtained during the first and the only beam time, there are some improvements to be done concerning the setup. As well there are unanswered questions to clarify, i.e., why the visibility is so low, what are the influences of this and why the visibility has its maxima for a DC of 0.4 of the source grating. Another aim for the future is to verify the measured visibility with simulations which include the influence of the neutron spectrum, the shape of the absorbing lines of the analyzer grating and as well the rest transmission of this grating.

For the future, the efficiency of our method opens up a way to perform computed phase tomography with neutrons in a reasonable time. Furthermore our technique is sensitive to image other quantum-mechanical phase shifts. For instance the magnetically induced phase shift inside domains can be imaged. It is also feasible to image the dynamically induced phase shifts, like the Fizeau effect. Since the fabrication process was developed to produce the gratings with optical photo lithography, there is no obstacle to upscale the size of the gratings to state-of-art wafer size with a diameter of 300 mm.

Appendix A

Run sheets for $\mathbf{G}_0$, $\mathbf{G}_1$, $\mathbf{G}_2$

The run sheets for the source grating G_0, the phase grating G_1 and the analyzer grating G_2 are given in Fig. A.1, Fig. A.2 and Fig. A.3, respectively. Every fabrication step is listed successively in the run sheets of the gratings. The programs used at the machines as well as the settings of the machines are given. The values in the run sheet correspond to machines at the clean room facility of the LMN at PSI. However, the adjustable parameters on the different processes are listed, so that the gratings can also be fabricated on similar machines.

1.	cleaning the Quartz substrate (Boron free) with isopropanol
2.	***<u>Sputtering:</u>*** **(Cr/Gd /Cr multilayer)** von Ardenne plant p_{Ar} = 0.2 mbar P = 70 W U = 500 V vacuum pump: 711 Hz (~ 10^{-6} mbar) 25 nm Cr (rate: 75 nm/min) 10 µm Gd (rate: 150 nm/min) 1 µm Cr (rate: 750nm/min)
3.	***<u>Photolithography:</u>*** cleaning of the waver with acetone and isopropanol <u>Spin coating</u> S1813, 4000 rpm, 1000 acc, 30 sec Softbake, 90° C, 90 sec, on hot plate <u>Exposure</u> photo mask: grid foil with 1120 µm period glued on mask blank hard contact, exp.time = 12 sec, gap = 40 µm , Cl 2 = 20 mW/cm^2 <u>Development</u> MF84MX, 25-30 sec
4.	***<u>Plasma etching of Cr masking layer:</u>*** BMP machine (vertical mask etcher) program MASK 100 sccm Cl_2 + 100 sccm CO_2 p = 200 mTorr P = max. power 1600 sec (rate: 1 nm/sec)
5.	hard bake of photoresist on hot plate, 135° C, 3 min
6.	***<u>Wet chemical etching of Gd layer:</u>*** H_2SO_4 : H_2O 1 : 100 in Teflon container 5 min rinse with water and dry with N_2
7.	Inspection: light microscope, α-step height measurement

Figure A.1: *Run sheet for the fabrication of the source grating.*

1.	oxidation of a [110] oriented Si wafer for a of 110 nm oxide layer
2.	***Photolithography:*** cleaning of the waver with acetone and isopropanol Spin coating S1805, 4000 rpm, 1000 acc, 30 sec softbake, 90° C, 90 sec, on hot plate Exposure mask: ICON_g1_64_64_7.94_0.38 alignment: Flat parallel to grating lines (done with marks on the photo mask) vacuum contact, exp.time = 4 sec, gap = 40 µm , Cl 2 = 20 mW/cm^2 Development MF84MX, 25-30 sec
3.	***Plasma etching of SiO_2 (RIE) :*** Oxford Plasma Lab 100 program GC62SIO2 10 sccm CHF_3 + 10 sccm O_2 T = 300 K, p = 100mTorr, P = 100 W t = 5 min
4.	***Plasma etching of photo resist:*** Tepla 300 plasma processor program 01 550 sccm O_2 P = 700 W t = 5 min
	Wet chemical etching of Si (KOH): BOE dip with the wafer for 5 sec KOH bath 76° C, 20 % in H_2O 24.6 min @ 1,5 µm/min etching rate flush with water (4 times) rinse with Isopropanol and dry with N_2
6.	***Wet chemical etching (BOE) :*** BOE in Teflon container 3 min flush with water (4 times) rinse with isopropanol and dry with N_2
7.	Inspection: Light microscope, SEM (topview, crossection)

Figure A.2: *Run sheet for the fabrication of the phase grating.*

1.	oxidation of a [110] oriented Si wafer for a of 60 nm oxide layer
2.	***Photolithography:*** cleaning of the waver with acetone and isopropanol Spin coating S1805, 4000 rpm, 1000 acc, 30 sec softbake, 90° C, 90 sec, on hot plate Exposure photo mask: Talbot_64_64_4,00_55 alignment: flat parallel to grating lines (done with marks on the photo mask) vacuum contact, exp.time = 7 sec, gap = 40 µm , Cl 2 = 20 mW/cm^2 Development MF84MX, 25-30 sec
3.	***Plasma etching of SiO_2 (RIE) :*** Oxford Plasma Lab 100 program GC62SIO2 10 sccm CHF_3 + 10 sccm O_2 T = 300 K, p = 100mTorr, P = 100 W t = 3 min
4.	***Plasma etching of photo resist:*** Tepla 300 plasma processor Program 01 550 sccm O_2 P = 700 W t = 5 min
	Wet chemical etching of Si (KOH): BOE dip with the wafer for 5 sec KOH bath 76° C, 20 % in H_2O 4 min @ 1,5 µm/min etching rate flush with water (4 times) rinse with Isopropanol and dry with N_2
6.	***Wet chemical etching of SiO_2 (BOE) :*** BOE in Teflon container 3 min flash with water (4 times) rinse with Isopropanol and dry with N_2
7.	Inspection: light microscope, SEM topview for Si bar width *s*
8.	***Evaporation of Gd :*** Balzer BAE 250 thermal evaporator mounting of the grating with an angle α = 16° and lines parallel to the evaporation boat l = 30 cm => x = 8.6 cm vacuum: ~10^{-6} mbar power control: 6 evaporation rate indicated with balance quartz: ~1 nm/sec evaporation height *h*: h = (s-p_2(1-DC)) / tan α deviation of balance quartz - SEM: 30-40% more on balance quartz
9.	Inspection: SEM (topview, cross section)

Figure A.3: *Run sheet for the fabrication of the analyzer grating.*

Bibliography

[All2000] B.E. Allman, P.J. McMahon, K.A. Nugent, D. Paganin, D.L. Jacobson, and S.A. Werner, Nature **408**, 158 (2000).

[Arr2000] V. Arizon, G. Rojo-Velaquez and J.G. Ibarra, *Fractional Talbot Effect: Compact Description*, Optical Review Vol. 7, No.2 129-131 (2000).

[Bla1952] J.M Blatt, V.F. Weisskopf, *Theoretical nuclear physics* (John Wiley, New York, 1952).

[Bor1980] M. Born and E. Wolf, *Principles of Optics* (Pergamon Press, Oxford, 1980).

[Cha1980] B. Chapman, *Glow discharge processes* (John Wiley & Sons, Inc., 1980).

[Dav2002] C. David, B. Nöhammer, E. Ziegler and H. H. Solak, *Differential X-ray ray phase contrast imaging using a shearing interferometer*, Appl. Phys. Lett.**81**, 3287-3289 (2002).

[Ehr2002] W. Ehrfeld, *Handbuch Mikrotechnik* (Carl Hanser Verlag München Wien, 2002).

[Fer1936] E. Fermi, *Sul moto dei neutroni lenti*, Ric. Scientifica **1**,13 (1936).

[Fey1948] R.P. Feynmann, *Space-time approach to non-relativistic quantum mechanics*, Rev. Mod. Phys. **20**, 367-387 (1948).

[Goo2004] J.W. Goodman, *Introduction to Fourier Optics* (Roberts & Company Publishers, 2005).

[Gol1974] M.L Goldberger, F. Seitz (1947), *Theory of the refraction and the diffraction of neutrons by crystals*, Rev. Mod. Phys. **71**, 294-310 (1947).

[Hyp2005] Hyper Physics 2005, Gerorgia State University, http://hyperphysics.phy-astr.gsu.edu/hbase/nuclear/shell.html.

[ICON] Imaging with Cold Neutrons beam line at the Paul Scherrer Institut , http://neutra.web.psi.ch/facility/icon_index.html.

[Kra1988] K.S. Krane, *Introductory Nuclear Physics* (John Wiley & Sons, Inc, 1988).

[Lip1995] G. Lipson, *Optical Physics, 3^{rd}Edition* (Cambridge University Press, 1995).

[LMN] Laboratory for Micro- and Nanotechnology at the Paul Scherrer Institut, http://lmn.web.psi.ch.

[McM2003] P.J. McMahon, B.E. Allman, M. Arif, S.A. Werner, and K.A. Nugent, *Quantitative Phase Radiography with Polychromatic Neutrons*, Phys. Rev. Lett. **91**, 145502 (2003).

[NCNR92] National Institute of Standards and Technolog, Neutron scattering length and cross sections, http://www.ncnr.nist.gov/resources/n-lengths/list.html.

[NCNR2004] National Institute of Standards and Technolog, Neutron scattering length and cross sections, http://www.ncnr.nist.gov/resources/n-lengths/sldcalc.html.

[Neutra] Neutron Transmission Radiography beam line at at the Paul Scherrer Institut, http://neutra.web.psi.ch/What/physic.html.

[Pfe2006a] F.Pfeiffer, T. Weitkamp, O. Bunk and C. David, *Phase retrieval and differential phase-contrast imaging with low-brilliance X-ray sources*, Nature Physics **2**, 258-261 (2006).

[Pfe2006b] F. Pfeiffer, C. Grünzweig, O. Bunk, G. Frei, E. Lehmann and C. David, *Phase imaging and Tomography with massive particles*, submitted.

[Rau1974] H. Rauch, W. Treimer and U. Bonse, *Test of a single crystal neutron interferometer*, Phys. Lett. **A47**, 369 (1974).

[Rau2000] H. Rauch and S.A. Werner, *Neutron Interferometry* (Oxford University Press, Oxford, 2000).

[Ris1980] I. Heilmann and Jorgen Kjems, *Mechanical velocity selector, neutron flux and q-range for small angle neutron scattering facility at Risø*, Risø 1980.

[Sea1989] V.F. Sears, *Neutron optics* (Oxford University Press, Oxford, 1989).

[Shipley] http://www.eng.yale.edu/rslab/resources/S1800seriesDataSheet.pdf.

[SINQ] Swiss Spallation Neutron Source SINQ, http://asq.web.psi.ch/ASQ/facilities/SINQS.html.

[Tre2003] W. Treimer, M. Strobl, A. Hilger, C. Seifert, and U. Feye-Treimer, *Refraction as imaging signal for computerized (neutron) tomography*, Appl. Phys. Lett. **83**, 398 (2003).

[Wei2004] T. Weitkamp, A. Diaz, B. Nöhammer, F. Pfeiffer, T. Rohbeck, P. Cloetens, M. Stampanoni, and C. David *Hard x-ray phase imaging and tomography with a grating interferometer*, Proceedings of the SPIE - The International Society for Optical Engineering **5535** p. 137-142 (2004)

[Wei2005] T. Weitkamp, A. Diaz, F. Pfeiffer, M. Stampanoni, P. Cloetens, E. Ziegler and C. David , *X-ray phase imaging with a grating interferometer*, Opt. Express **13**, 6296-6304 (2005).

Danksagung

An dieser Stelle möchte ich all jenen, die zum Gelingen dieser Diplomarbeit und meinem Studium beigetragen haben, danken.

Herr Prof. Dr. Ihringer möchte ich für seine spontane Bereitschaft, diese Diplomarbeit extern zu betreuen, danken. Ohne dies wäre das Zustandekommen dieser Arbeit niemals möglich gewesen. Bei Herr Prof. Schreiber möchte ich mich bedanken, dass er sich als Zweitgutachter bereit erklärt hat.

Meinen beiden Betreuern am PSI, Dr. Christian David und Dr. Franz Pfeiffer, möchte ich hiermit ganz besonders danken. Ohne ihre Ideen und Hilfe hätte diese Arbeit in dem einen Jahr und in dem ausführlichen Rahmen nicht verwirklicht werden können.

Ein grosses Dankeschön gilt Dr. Oliver Bunk für sein immer offenes Ohr für alle möglichen Fragen und seine ausdauernde Hilfe beim Zusammenschreiben der Arbeit. Ohne ihn wäre ich sicherlich verzweifelt.

Bedanken möchte ich mich auch bei Dr. Ian Johnson (the boss) und Dr. Dillip Satapathy (the chief) für das Korrekturlesen der Diplomarbeit und die Englischkorrekturen.

Bei Gabriel Frei möchte ich mich bedanken für die Hilfe beim Aufbauen des Experimentes an der beam line.

Ein ganz grosser Dank gilt auch meinen ganzen Studienkollegen, die mich über die acht Semester lang begleitet haben. "Prof." Andreas Gumann danke ich für die wirklich tolle Zeit während den Praktikumsversuchen und der Hilfe bei sämtlichen Übungsblättern. Benjamin Sobotta, Michael Spannowsky, Achim Nonnenmacher, Michael Fromm, Matthias Hofmann und Karin Marianowski danke ich für tollen vier Jahre und die immer wieder lustigen Diskussionen beim Mittagessen. Bernhard Thomaszewski danke ich für die "Rettung" meines Studiums und das damit verbundene Bier auf dem Marktplatz.

Meinen WG-Kollegen aus Tübingen, Michael "Michel de Dicke" Becker, Domenik Schnurr, Karl Sippel, Dennis Lochmann und Matthias Gruenzweig von der Fässle-WG (www.faessle-wg.de) danke ich für die immer geile Zeit, die wir zusammen mit dem einen oder anderen Fässle hatten.
Ebenso danke ich meinen WG-Kollegen aus Riniken (The Riniken's) Onkel Murat Ay, Onkel Florian Piegsa und Onkel Daniel Dos Santos Covita für die tolle Zeit (es lebe der Papstbalkon!).

Meinem Schnuckelputz danke ich für das stundenlange Köpfchenkraulen während dem Lernen auf die Diplomprüfungen.

Mein letzter und zugleich grösster Dank gilt meinen Eltern und meinem Bruder für

Ihre unermüdliche Hilfe und Unterstützung während des Studiums und das Vertrauen in mich. Vor allem möchte ich mich bei meinen Eltern für die finanzielle Unterstützung während des Studiums bedanken. Ich hoffe, dass ich ihnen mit dieser Arbeit ein kleines Dankeschön zurückgeben kann. Danken möchte ich auch noch einmal meinem Papa und meinem Bruder für die vielen "Taxifahrten" nach Tübingen und in die Schweiz.

Erklärung

Die vorliegende Diplomarbeit habe ich unter Verwendung der angegeben Literatur selbständig verfasst. Es wurden dabei keine anderen als die angegebenen Quellen und Hilfsmittel verwendet.

Tübingen, den 28. April 2006

Ein kleiner Schritt für die Menschheit,
aber ein grosser Schritt für mich.

. . . to be continued . . .